

Magma Plumbing Systems:

Magee, Craig; Stevenson, Carl; Ebmeier, Susanna; Keir, Derek; Hammond, James; Gottsmann, Joachim; Whaler, Kathryn; Schofield, Nick; Jackson, Christopher; Petronis, Mike; O'Driscoll, Brian; Morgan, Joanna; Cruden, ALEXander; Vollgger, Stefan; Dering, Gregory; Micklethwaite, Steven; Jackson, Matthew

DOI:

[10.1093/petrology/egy064](https://doi.org/10.1093/petrology/egy064)

License:

None: All rights reserved

Document Version

Peer reviewed version

Citation for published version (Harvard):

Magee, C, Stevenson, C, Ebmeier, S, Keir, D, Hammond, J, Gottsmann, J, Whaler, K, Schofield, N, Jackson, C, Petronis, M, O'Driscoll, B, Morgan, J, Cruden, AL, Vollgger, S, Dering, G, Micklethwaite, S & Jackson, M 2018, 'Magma Plumbing Systems: A Geophysical Perspective', *Journal of Petrology*.
<https://doi.org/10.1093/petrology/egy064>

[Link to publication on Research at Birmingham portal](#)

Publisher Rights Statement:

This is a pre-copyedited, author-produced version of an article accepted for publication in *Journal of Petrology* following peer review. The version of record Carl Stevenson, Magma Plumbing Systems: A Geophysical Perspective, *Journal of Petrology*, 23/06/2018, egy064, is available online at: [10.1093/petrology/egy064](https://doi.org/10.1093/petrology/egy064)

Checked 22/06/2018.

General rights

Unless a licence is specified above, all rights (including copyright and moral rights) in this document are retained by the authors and/or the copyright holders. The express permission of the copyright holder must be obtained for any use of this material other than for purposes permitted by law.

- Users may freely distribute the URL that is used to identify this publication.
- Users may download and/or print one copy of the publication from the University of Birmingham research portal for the purpose of private study or non-commercial research.
- User may use extracts from the document in line with the concept of 'fair dealing' under the Copyright, Designs and Patents Act 1988 (?)
- Users may not further distribute the material nor use it for the purposes of commercial gain.

Where a licence is displayed above, please note the terms and conditions of the licence govern your use of this document.

When citing, please reference the published version.

Take down policy

While the University of Birmingham exercises care and attention in making items available there are rare occasions when an item has been uploaded in error or has been deemed to be commercially or otherwise sensitive.

If you believe that this is the case for this document, please contact UBIRA@lists.bham.ac.uk providing details and we will remove access to the work immediately and investigate.



Draft Manuscript for Review

Magma Plumbing Systems: A Geophysical Perspective

Journal:	<i>Journal of Petrology</i>
Manuscript ID	JPET-Jun-17-0068.R2
Manuscript Type:	Perspectives in Petrology
Date Submitted by the Author:	n/a
Complete List of Authors:	<p>Magee, Craig; The University of Birmingham, Earth Sciences Stevenson, Carl; University of Birmingham, School of Geography, Earth and Environmental Sciences Ebmeier, Susanna; Univeristy of Leeds Keir, Derek Hammond, James Gottsmann, Joachim; University of Bristol, School of Earth Sciences Whaler, Kathryn Schofield, Nick Jackson, Christopher Petronis, Mike O'Driscoll, Brian; University of Manchester, School of Earth, Atmospheric and Environmental Sciences Morgan, Joanna Cruden, Sandy; Monash University, School of Geosciences Vollgger, Stefan Dering, Gregory Micklethwaite, Steven Jackson, Matthew; Imperial College London, Earth Science and Engineernig</p>
Keyword:	geophysics, magma plumbing system, magma flow

SCHOLARONE™
Manuscripts

1
2
3
4
5
6 1 *Perspectives in Petrology*
7
8 2

9
10 3 **Magma Plumbing Systems: A Geophysical Perspective**
11
12 4

13
14 5 ¹Craig Magee, ²Carl T.E. Stevenson, ³Susanna K. Ebmeier, ^{4,5}Derek Keir, ⁶James O.S. Hammond,
15 6 ⁷Joachim H. Gottsmann, ⁸Kathryn A. Whaler, ⁹Nick Schofield, ¹Christopher A-L. Jackson,
16 7 ¹⁰Michael S. Petronis, ¹¹Brian O'Driscoll, ¹Joanna Morgan, ¹²Alexander Cruden, ¹²Stefan A.
17 8 Vollgger, ¹³Greg Dering, ¹²Steven Micklethwaite, ¹Matthew D. Jackson,
18
19 9

20
21 10 ¹Department of Earth Science and Engineering, Imperial College London, London, SW7 2BP, UK
22
23 11

24 12 ²School of Geography, Earth and Environmental Sciences, University of Birmingham, Birmingham, B15
25 13 2TT, UK
26 14

27 15 ³School of Earth Science and Environment, University of Leeds, Leeds, LS2 9JT, UK
28 16

29 17 ⁴Ocean and Earth Science, University of Southampton, Southampton, SO14 3ZH, UK
30 18

31 19 ⁵Dipartimento di Scienze della Terra, Università degli Studi di Firenze, Florence, 50121, Italy
32 20

33 21 ⁶Department of Earth and Planetary Sciences, Birkbeck, University of London, London, WC1E 7HX, UK
34 22

35 23 ⁷School of Earth Sciences, University of Bristol, Bristol, BS8 1RJ, UK
36 24

37 25 ⁸School of GeoSciences, University of Edinburgh, Grant Institute, Edinburgh, EH9 3FE, UK
38 26

39 27 ⁹Geology and Petroleum Geology, School of Geosciences, University of Aberdeen, Aberdeen, AB24 3UE,
40 28 UK
41 29

42 30 ¹⁰Environmental Geology, Natural Resource Management Department, New Mexico Highlands University,
43 31 PO Box 9000, Las Vegas, NM 87701, USA
44 32

45 33 ¹¹School of Earth and Environmental Sciences, University of Manchester, Manchester, M13 9PL, UK
46 34

47 35 ¹²School of Earth, Atmosphere and Environment, Monash University, Melbourne, Victoria, 3800, Australia
48 36

49 37 ¹³School of Earth Sciences, University of Western Australia, Perth, 6009, Australia
50 38

51
52 27 **Abstract**
53
54
55
56
57
58
59
60

1
2
3
4
5
6 28 Over the last few decades, significant advances in using geophysical techniques to image the
7
8 29 structure of magma plumbing systems have enabled the identification of zones of melt
9
10 30 accumulation, crystal mush development, and magma migration. Combining advanced geophysical
11
12 31 observations with petrological and geochemical data has arguably revolutionised our understanding
13
14 32 of and afforded exciting new insights into the development of entire magma plumbing systems.
15
16 33 However, divisions between the scales and physical settings over which these geophysical,
17
18 34 petrological, and geochemical methods are applied still remain. To characterise some of these
19
20 35 differences and promote the benefits of further integration between these methodologies, we
21
22 36 provide a review of geophysical techniques and discuss how they can be utilised to provide a
23
24 37 structural context for and place physical limits on the chemical evolution of magma plumbing
25
26 38 systems. For example, we examine how Interferometric Synthetic Aperture Radar (InSAR), coupled
27
28 39 with Global Positioning System (GPS) and Global Navigation Satellite System (GNSS) data, and
29
30 40 seismicity may be used to track magma migration in near real-time. We also discuss how seismic
31
32 41 imaging, gravimetry, and electromagnetic data can image contemporary melt zones, magma
33
34 42 reservoirs, and/or crystal mushes. These techniques complement seismic reflection data and rock
35
36 43 magnetic analyses that delimit the structure and emplacement of ancient magma plumbing systems.
37
38 44 For each ~~of these techniques, with the addition as well as the emerging use~~ of full-waveform
39
40 45 inversion (FWI), ~~the use of~~ and Unmanned Aerial Vehicles (UAVs), and the integration of
41
42 46 geophysics with numerical modelling, we discuss potential future directions ~~and opportunities~~. We
43
44 47 show that approaching problems concerning magma plumbing systems from an integrated
45
46 48 petrological, geochemical, and geophysical perspective will undoubtedly yield important scientific
47
48 49 advances, providing exciting future opportunities for the volcanological community.
49
50
51
52
53
54
55
56
57
58
59
60

51 **1. Introduction**

50 52 Igneous petrology and geochemistry are concerned with the chemical and physical mechanisms
51
52 53 governing melt genesis, mobilisation, and segregation, as well as the transport/ascent, storage,
53
54
55
56
57
58
59
60

1
2
3
4
5
6 54 evolution, and eruption of magma. The reasons for studying these fundamental processes include
7
8 55 understanding volcanic eruptions, modelling the mechanical development of magma conduits and
9
10 56 reservoirs, finding magma-related economic ore deposits, exploring for active geothermal energy
11
12 57 sources, and determining the impact of magmatism in different plate tectonic settings on the
13
14 58 evolution of the lithosphere and crustal growth ~~of the crust~~. However, whilst petrological and
15
16 59 geochemical studies over the last century have shaped our understanding of the physical and
17
18 60 chemical evolution of magma plumbing systems, assessing the distribution, movement, and
19
20 61 accumulation of magma in the Earth's crust from these data remains challenging. A key frontier in
21
22 62 igneous petrological and geochemical research thus involves deciphering how and where magma
23
24 63 forms, the routes it takes toward the Earth's surface, and where exactly it is stored.

24 64 This contribution will demonstrate how geophysical data can be used to determine the
25
26 65 architecture of magma plumbing systems, providing a structural framework for the interpretation of
27
28 66 petrological and geochemical data. To aid the alignment of petrological, geochemical, and
29
30 67 geophysical disciplines it is first important to delineate what we mean by 'magma'. We follow
31
32 68 Glazner *et al.*, (2016) and define magma as, "naturally occurring, fully or partially molten rock
33
34 69 material generated within a planetary body, consisting of melt with or without crystals and gas
35
36 70 bubbles and containing a high enough proportion of melt to be capable of intrusion and extrusion".
37
38 71 Importantly, this definition specifically considers that magma: (i) forms through the migration and
39
40 72 accumulation of partial melt that is initially distributed throughout pore spaces in a rock volume;
41
42 73 and (ii) is a suspension of particles (i.e. crystals, xenoliths, and/or bubbles) within melt (see
43
44 74 Cashman *et al.*, 2017). As magma starts to solidify, the proportion of suspended crystals and thus
45
46 75 the relative viscosity of the magma increases until a relatively immobile, continuous network of
47
48 76 crystals and interstitial melt develops; we term this a 'crystal mush' (e.g., Hildreth, 2004; Glazner *et*
49
50 77 *al.*, 2016; Cashman *et al.*, 2017). The rheological transition from a magma to a crystal mush is
51
52 78 partly dependent on its chemistry, but typically occurs abruptly when the particle volume increases
53
54 79 across the 50–65% range (Cashman *et al.*, 2017). Crystal mushes thus exist at or above the solidus
55
56
57
58
59
60

1
2
3
4
5
6 80 | and ~~largely-generally~~ cannot be erupted, although they may be partly entrained in eruptible magma
7
8 81 | as glomerocrysts, cumulate nodules, or restite (Cashman *et al.*, 2017). Migration of interstitial melt
9
10 82 | within a crystal mush can lead to its accumulation and, thus, formation of a magma. A magma
11 83 | plumbing system therefore consists of interconnected magma conduits and reservoirs, which store
12
13 84 | magma as it evolves into a crystal mush, ultimately fed from a zone of partial melting (e.g., Fig. 1).
14
15 85 | These definitions are supported by geophysical imaging and analyses of contemporary reservoirs,
16
17 86 | which show melt volumes in the mid- to upper crust are typically low (<10%) and likely exist
18
19 87 | within a crystal mush (e.g., Paulatto *et al.*, 2010; Koulakov *et al.*, 2013; Ward *et al.*, 2013;
20
21 88 | Hammond, 2014; Comeau *et al.*, 2015; Comeau *et al.*, 2016; Delph *et al.*, 2017). These definitions
22
23 89 | and geophysical data question the traditional view that magma resides in long-lived, liquid-rich, and
24
25 90 | volumetrically significant magma chambers. Following this, the emerging paradigm for igneous
26
27 91 | systems is thus that liquid-rich magma chambers are short-lived, transient phenomena with: (i) melt
28
29 92 | typically residing in mushes that develop through the incremental injection of small, distinct magma
30
31 93 | batches; and (ii) magma accumulating in thin lenses (e.g., Hildreth, 2004, Annen *et al.*, 2006;
32
33 94 | Annen, 2011; Miller *et al.*, 2011; Solano *et al.*, 2012; Cashman & Sparks, 2013; Annen *et al.*, 2015;
34
35 95 | Cashman *et al.*, 2017). We are now starting to view magmatic systems as a vertically extensive,
36
37 96 | transcrustal, interconnected networks of magma conduits and magma/mush reservoirs (Fig. 1) (e.g.,
38
39 97 | Cashman *et al.*, 2017).

39 98 | The current use of geophysical techniques within the igneous community can be separated
40
41 99 | into two distinct areas focused on either characterising active volcanic domains or investigating the
42
43 100 | structure and emplacement of ancient magma plumbing systems. For example, in areas of active
44
45 101 | volcanism, our understanding of magma plumbing system structure principally comes from the
46
47 102 | application of geophysical techniques that detect sites of magma movement or accumulation (e.g.,
48
49 103 | Sparks *et al.*, 2012; Cashman & Sparks, 2013). Such geophysical techniques include Interferometric
50
51 104 | Synthetic Aperture Radar (InSAR; e.g., Biggs *et al.*, 2014), seismicity (e.g., recording of
52
53 105 | earthquakes associated with magma movement; e.g., White & McCausland, 2016), various seismic
54
55
56
57
58
59
60

1
2
3
4
5
6 106 imaging methods (e.g., Paulatto *et al.*, 2010; Hammond, 2014), gravimetry (e.g., Battaglia *et al.*,
7
8 107 1999; Rymer *et al.*, 2005), and electromagnetic techniques (Desissa *et al.*, 2013; Comeau *et al.*,
9
10 108 2015). These techniques allow examination of: (i) the temporal development of magma plumbing
11
12 109 systems (e.g., Pritchard & Simons, 2004; Sigmundsson *et al.*, 2010); (ii) vertical and lateral
13
14 110 movements of magma (e.g., Keir *et al.*, 2009; Jay *et al.*, 2014); (iii) the relationship between
15
16 111 eruption dynamics, volcano deformation, and intrusion (e.g., Sigmundsson *et al.*, 2010;
17
18 112 Sigmundsson *et al.*, 2015); and (iv) estimates of melt sources and melt fractions (e.g., Desissa *et al.*,
19
20 113 2013; Johnson *et al.*, 2016). However, inversion of these geophysical data typically results in non-
21
22 114 unique, relatively low-resolution models of subsurface structures. Furthermore, some methods only
23
24 115 capture active processes, which may be short-lived or even instantaneous, potentially providing
25
26 116 information on only a small fraction of the magma plumbing system.

26
27 117 In contrast to the study of active volcanic domains, the analysis of ancient plumbing systems
28
29 118 through field observations, geophysical imaging techniques (e.g., reflection seismology, gravity,
30
31 119 and magnetic data), and/or rock magnetic experiments can provide critical insights into magma
32
33 120 emplacement, mush evolution, and allow the geometry of entire plumbing systems to be
34
35 121 reconstructed (e.g., Cartwright & Hansen, 2006; Stevenson *et al.*, 2007a; Petronis *et al.*, 2013;
36
37 122 Muirhead *et al.*, 2014; O'Driscoll *et al.*, 2015; Magee *et al.*, 2016). Whilst such studies of ancient
38
39 123 plumbing systems provide a framework for interpreting the structure of active intrusion networks,
40
41 124 capturing a snapshot of how magma moved and melt was distributed through the system at any one
42
43 125 time is difficult because magmatism has long since ceased.

44
45 126 All the techniques employed to define active and ancient plumbing systems, including
46
47 127 petrological and chemical analyses, provide information at different spatial and/or temporal
48
49 128 resolutions. Answering the major outstanding questions in studies of magma plumbing systems
50
51 129 therefore requires the integration of complementary petrological, geochemical, geophysical,
52
53 130 geochronological, and structural techniques. Here, we examine ~~how the distribution of melt,
54
55 131 magma, and mush can be determined in~~ active plumbing systems using InSAR, seismicity, seismic
56
57
58
59
60

1
2
3
4
5
6 132 imaging, gravimetry, and electromagnetic techniques. To provide a context for the interpretation of
7
8 133 data pertaining to the ~~modern distribution of melt, magma, and mush in~~ active systems, we also
9
10 134 discuss how seismic reflection data and rock magnetic techniques can be used to derive the
11
12 135 structure and evolution of ancient ~~plumbing systems~~ intrusion networks. The potential of emerging
13
14 136 techniques involving seismic full-waveform inversion (FWI) and unmanned aerial vehicles (UAVs)
15
16 137 are also considered, as is the role of numerical modelling in bringing together outputs from different
17
18 138 datasets. For each technique described, we briefly discuss the methodology and limitations and
19
20 139 provide a summary of the key findings and potential uses, with a focus on integration with
21
22 140 petrological and geochemical data. The aim of this review is to facilitate and promote integration
23
24 141 between petrologists, geochemists, geochronologists, structural geologists, and geophysicists
25
26 142 interested in addressing outstanding problems in studies of magma plumbing systems.

28 144 **2. Understanding magma plumbing system structure**

30
31 145 Here, we discuss a range of techniques that can be utilised to define different aspects of magma
32
33 146 plumbing system structure and evolution. In particular, we describe how InSAR, seismicity, seismic
34
35 147 imaging (e.g., seismic tomography), gravity, and electromagnetic data is used to determine melt
36
37 148 fractions and distribution, track movement of magma in near real-time, and/or locate sites and
38
39 149 examine the evolution of magma/mush storage. Overall, these geophysical techniques allow the
40
41 150 structure of active plumbing systems and their transient evolution to be assessed. We also discuss
42
43 151 how seismic reflection data can provide unprecedented images of ancient plumbing systems and
44
45 152 associated host rock deformation in three-dimensions at resolutions of 10's of metres. Finally, we
46
47 153 examine the application of rock magnetic techniques to assess magma flow and crystallisation
48
49 154 processes at a range of scales.

50
51 155 Although beyond the scope of this review, it is critical to highlight that interpreting the
52
53 156 geophysical response of a rock or magma relies on understanding its physical and chemical
54
55 157 properties (e.g., density, temperature, and melt fraction). Laboratory experiments testing how rock
56
57
58
59
60

1
2
3
4
5
6 158 or magma properties influence geophysically measured parameters (e.g., seismic velocities and
7
8 159 resistivity) thus provide context for interpreting magma plumbing system structure and evolution
9
10 160 from geophysical data (e.g., Gaillard, 2004; Pommier *et al.*, 2010; Pommier, 2014).

11 161 12 13 162 **2.1. Insights into magma plumbing systems from ground deformation data**

14 15 163 *Technique*

16
17 164 Changes in volume within ~~shallow level~~ magma plumbing systems can deform the host rock,
18
19 165 potentially resulting in displacement of ~~the~~ Earth's surface. Such displacements are a unique source
20
21 166 of information for volcanologists and can be modelled to estimate geodetic source depth and, to
22 167 varying extents, the source geometry and volume change (e.g., Segall, 2010). Measuring the
23
24 168 deformation of the Earth's surface can thus provide information about the characteristics and timing
25
26 169 of magma movement and accumulation, as well as variations in internal reservoir conditions.
27
28 170 Traditionally, deformation measurements are made using levelling, electronic distance meters,
29
30 171 tiltmeters, and Global Positioning System (GPS), ~~all of~~ which have proven to be reliable methods
31
32 172 and thus are widely used in volcano monitoring (e.g., Dzurisin, 2006). For example, GPS
33 173 measurements retrieve the relative positions of receivers on Earth's surface from dual frequency
34
35 174 carrier phase signals transmitted from GPS or Global Navigation Satellite System (GNSS) satellites
36
37 175 with precisely known orbits. Distances between satellites and receivers are assessed from the travel-
38
39 176 time, i.e. the measured difference between the transmitted and received times of a unique ranging
40
41 177 code, allowing movement of the Earth's surface over time to be monitored (see review by Dixon,
42
43 178 1991). Permanently installed receivers record position data continuously, but receivers can also be
44 179 deployed for a limited time during GPS campaigns to provide additional measurements, normally
45
46 180 made relative to a standard benchmark location (e.g., Dvorak & Dzurisin, 1997). Whilst tiltmeters
47
48 181 and GPS can provide continuous measurements, their spatial resolution is limited by logistical
49
50 182 constraints such as cost and accessibility, which may be restricted at active volcanoes.

1
2
3
4
5
6 183 The geographic reach of volcano geodesy has been greatly expanded over the past two
7
8 184 decades by the application of Interferometric Synthetic Aperture Radar (InSAR), an active remote
9
10 185 sensing technique that uses microwave electromagnetic radiation to image the Earth's surface (e.g.,
11 186 Simons & Rosen, 2007; Pinel *et al.*, 2014). Surface displacements can be measured by constructing
12
13 187 interferograms, where the difference in phase between radar echoes from ~~time-time~~-separated
14
15 188 images appear as 'fringes' of variation in the line of sight distance to the satellite (Fig. 2). The
16
17 189 patterns of fringes in individual interferograms are distinctive for different deformation source
18
19 190 geometries, such as for horizontal (sill-like) or vertical (dyke-like) opening of intrusions, or the
20
21 191 pressurisation of a spheroidal reservoir (i.e. a Mogi source) (e.g., Fig. ~~2B2b~~). However, magma
22 192 intrusion processes can rarely be uniquely identified from geodetic source geometry alone, and
23
24 193 distinguishing between magmatic, hydrothermal, structural (e.g., faulting and compaction), and
25
26 194 combinations of elastic and inelastic sources is particularly challenging (e.g., Galland, 2012;
27
28 195 Holohan *et al.*, 2017).

29
30 196 Whilst a single interferogram only provides displacements in satellite line-of-sight, a
31
32 197 pseudo-3D displacement field can be estimated by combining ~~data-multiple images~~ from polar
33
34 198 orbits that are ascending (i.e. satellite moves roughly northward, looking east) and descending (i.e.
35 199 satellite moves roughly southward, looking west) (Fig. 2A2a), especially where GNSS
36
37 200 measurements can also be incorporated. The lateral spatial resolution of most InSAR data is on the
38
39 201 order of metres to tens of metres, whilst vertical movements can be resolved on the order of
40
41 202 centimetres and sometimes millimetres. Temporal resolution depends on the satellite revisit time
42
43 203 and ranges between days to months depending upon the sensor type and satellite orbit. This means
44 204 that InSAR can be used to regularly assess ground deformation at virtually any volcano worldwide
45
46 205 situated above sea level, with a higher spatial density of measurements than ~~has been achievable~~
47
48 206 achieved using from ground-based instrumentation.

49
50 207 Magmatic processes are only observable by InSAR when either magma movement or
51
52 208 internal reservoir processes (e.g., cooling and contraction, phase changes) cause changes in pressure

1
2
3
4
5
6 209 and thereby instigate deformation of the host rock and free surface. The best-fit parameters of a
7
8 210 deformation source (e.g., an intruding magma body) are most often assessed by inverting measured
9
10 211 displacements using analytical elastic-half space models of simple source geometries, although
11
12 212 there are often trade-offs between parameters such as source depth and volume change (e.g.,
13
14 213 Pritchard & Simons, 2004). Complex and more realistic deformation source geometries may be
15
16 214 retrieved using finite element-based linear inversion of displacement fields (e.g., Ronchin *et al.*,
17
18 215 2017). A proportion of any pressure change may be accommodated by magma compressibility,
19
20 216 leading to underestimation of volume changes (e.g., Rivalta & Segall, 2008; McCormick-Kilbride *et*
21
22 217 *al.*, 2016). Assessing both volume changes and especially the total volume of a magma reservoir
23
24 218 from geodetic data therefore remains challenging. Furthermore, host rocks in areas of repeated
25
26 219 intrusion that have been heated above the brittle-ductile transition are better described by a
27
28 220 viscoelastic rheology (e.g., Newman *et al.*, 2006; Yamasaki *et al.*, 2018), while ductile
29
30 221 accommodation of volume changes may occur at greater depth. Where some constraints are
31
32 222 available for the structure and rheology of Earth's crust, finite or boundary element models may
33
34 223 achieve a more realistic model of the deformation source (e.g., Masterlark, 2007; Hickey *et al.*,
35
36 224 2017; Gottsmann *et al.*, 2017).

37 226 **Observations**

38
39 227 Measurements of volcano deformation preceding and/or accompanying eruption have provided
40
41 228 insights into the extent and structure of magma plumbing systems and, in some instances, the
42
43 229 dynamics of magma movement ~~through them~~. For example, ~~new~~ InSAR-based observations at
44
45 230 Eyjafjallajökull, Iceland have recognised the intrusion of multiple, distinct sills over a decade and
46
47 231 their subsequent extraction when tapped during an explosive eruption (e.g., Pedersen &
48
49 232 Sigmundsson, 2006; Sigmundsson *et al.*, 2010). ~~Over shorter timescales of days to months,~~
50
51 233 ~~deformation at Alu-Dalafilla, Ethiopia has demonstrated the temporal association between localised~~
52
53 234 ~~uplift and subsidence attributed to shallow sill intrusion and co-eruptive dyke opening (e.g., Figs 3A~~
54
55
56
57
58
59
60

1
2
3
4
5
6 235 ~~and B) (Pagli *et al.*, 2012)~~. Extensive lateral connections via dykes and sills between reservoirs
7
8 236 and/or volcanoes have been illuminated by eruptions or unrest accompanied by ground deformation
9
10 237 tens of kilometres away, and by the existence of multiple deformation sources (e.g., [Alu-Dalafilla](#)
11
12 238 [shown in Figures 3 and b. Pagli *et al.*, 2012](#); Korovin, Lu & Dzurisin, 2014; Cordon-Caulle, Jay *et*
13 239 *al.*, 2014; Kenyan volcanoes, Biggs *et al.*, 2014; global synthesis, Ebmeier *et al.*, 2018). Inter-
14
15 240 eruptive deformation at calderas is especially complex and seems to be particularly frequent and
16
17 241 high magnitude (e.g., Laguna del Maule; Fournier *et al.*, 2010; Singer *et al.*, 2014; Le Mével *et al.*,
18
19 242 2015), with the location of the deformation sources inferred to vary over time (e.g., Campi Flegrei,
20
21 243 Trasatti *et al.*, 2004; Yellowstone, Wicks *et al.*, 2006). ~~Overall, t~~The geometries of dykes and sills
22 244 inferred from InSAR data ~~reflect and~~ inform our understanding of changing subsurface stress fields
23
24 245 (e.g., Afar, Hamling *et al.*, 2010; Fernandina, Bagnardi *et al.*, 2013), as do measurements of
25
26 246 displacements caused by moderate earthquakes in close proximity to magma plumbing systems
27
28 247 (e.g., Kilauea, Wauthier *et al.*, 2013; Chiles-Cerro Negro, Ebmeier *et al.*, 2016).

Formatted: Font: Italic

29
30 248 At a transcrustal scale, deformation measurements have contributed to evidence for temporal
31
32 249 variations in magma supply rates (e.g., in Hawaii, Poland *et al.*, 2012). ~~and v~~Volume increases in
33 250 the mid- to lower-crust, notably in the Central Andes, have provided the first observations of deep
34
35 251 pluton growth (Pritchard & Simons, 2004). Furthermore, uplift during episodes of unrest that have
36
37 252 not (yet) resulted in eruption have been detected at a broad range of volcanoes (e.g., Westdahl,
38
39 253 Mount Peulik, Lu & Dzurisin, 2014; Alutu and Corbetti, Biggs *et al.*, 2011) and, in some cases,
40
41 254 have been interpreted as evidence for the ‘pulsed’ accumulation of potentially eruptible magma
42
43 255 (e.g., Santorini, Parks *et al.*, 2012). In addition to magma movement, volume changes associated
44 256 with internal reservoir processes can also cause deformation of the host rock and free surface. For
45
46 257 example, InSAR measurements have recorded subsidence linked to cooling and crystallisation of
47
48 258 sills (Medicine Lake, Parker, 2016; Taupo Volcanic Zone, Hamling *et al.*, 2015). Transient periods
49
50 259 of subsidence during inter-eruptive uplift have been attributed to phase transitions in response to the
51
52 260 addition of more juvenile magma (e.g., Okmok, Caricchi *et al.*, 2014).

Implications and integration

InSAR has increased the number of volcanoes where measurements of ground deformation have been made, from less than 50 in the late 1990s to over 200 ~~and counting~~ today (Biggs & Pritchard, 2017; Ebmeier *et al.*, 2018). This increase in coverage has been particularly influential in the developing world where monitoring infrastructure is typically poor (Ebmeier *et al.*, 2013; Chaussard *et al.*, 2013), with InSAR often providing the first evidence of magmatic activity at many volcanoes previously considered to be inactive (e.g., Pritchard & Simons, 2004; Biggs *et al.*, 2009; Biggs *et al.*, 2011; Lu & Dzurisin, 2014). A continued increase in the number and range of satellite- and large-scale UAV-based SAR instruments, as well as enhancements to their spatial and temporal resolution, ~~over the coming years~~ will allow the detection of a greater range of volcanic ground deformation (e.g., Salzer *et al.*, 2014; Schaefer *et al.*, 2015; Stephens *et al.*, 2017). Overall, improved InSAR coverage will also increase the number of volcanoes where deformation measurements have been made across multiple cycles of eruption and deformation, increasing its usefulness for both hazard assessment and for characterising the extent, geometry, and changes in magma plumbing systems.

~~Geodetic measurements provide information only about the parts of a plumbing system that are currently active, and do not necessarily reflect the full extent and character of the intrusion network (e.g., Sigmundsson, 2016). Several field, geophysical, and modelling-based studies highlight accommodation of magma can involve inelastic processes (e.g., compaction and faulting), which may: (i) mean uplift and/or subsidence does not wholly reflect the size of the underlying magma body (e.g., Morgan *et al.*, 2008; Galland, 2012; Magee *et al.*, 2013; Schofield *et al.*, 2014); or (ii) themselves contribute to the ground deformation signal, meaning the location of modelled geodetic sources may not be accurate (Holohan *et al.*, 2017). Despite these limitationHowever,~~ geodetic analyses of ground deformation provide critical insight into the spatial and temporal development of active plumbing systems. Comparing observations of ancient plumbing systems

(e.g., Magee *et al.*, 2013; Schofield *et al.*, 2014), integration of ground deformation measurements with petrological observations (e.g., Caricchi *et al.*, 2014; Jay *et al.*, 2014) or thermal models (Parker *et al.*, 2016), as well as tomographic geophysical imaging, will increase the sophistication of models of magmatic systems. Furthermore, integrating InSAR with gravity or electromagnetic measurements is particularly powerful, as it can allow discrimination between melt, volatiles, and hydrothermal fluids for which deformation signals are similar (see section 2.4) (e.g., Tizzani *et al.*, 2009).

2.2. Seismicity and magma plumbing systems

Technique

Seismicity (i.e. earthquakes) at volcanoes is primarily caused by the dynamic interaction of magma and hydrothermal fluids with the solid host rock (e.g., Chouet & Matoza, 2013), as well as by fracturing and fragmentation of silicic magma (e.g., Tuffen *et al.*, 2008). There are a number of primary physical mechanisms for causing volcano seismicity (e.g., faulting), each of which typically produces seismic signals of specific frequency content (Chouet & Matoza, 2013). Recording and isolating different volcano seismicity signals therefore allows a variety of plumbing system processes to be assessed. As such, the majority of volcano monitoring agencies have now deployed or aim to use a network of distributed seismic sensors, including broadband seismometers, to monitor volcano activity (Neuberg *et al.*, 1998; Sparks *et al.*, 2012). Furthermore, an increase in computing power and reduction in cost of seismic sensors means that researchers are now developing fast, fully automated detection and real-time location techniques that are fast and can locate seismicity to sub-decimetre precision (e.g., Drew *et al.*, 2013; Sigmundsson *et al.*, 2015).

Observations

Volcano-tectonic (VT) seismicity generally produces relatively high frequency (1–20 Hz), short period signals, involving clear primary (P), secondary (S), and surface waves, which are caused by

Formatted: Font: Italic

Formatted: Font: Italic

1
2
3
4
5
6
7
8
9
10
11
12
13
14
15
16
17
18
19
20
21
22
23
24
25
26
27
28
29
30
31
32
33
34
35
36
37
38
39
40
41
42
43
44
45
46
47
48
49
50
51
52
53
54
55
56
57
58
59
60

displacement on new or existing faults in the host rock in response to fluid-induced stress changes (e.g., Rubín & Gillard, 1998; Roman & Cashman, 2006; Tolstoy *et al.*, 2008). These earthquakes commonly occur near the propagating edge of intrusions, meaning the space-time evolution of VT earthquake locations can be used to track the horizontal and vertical growth of sills and dykes (e.g., Keir *et al.*, 2009; Sigmundsson *et al.*, 2010; Sigmundsson *et al.*, 2015). Inflation of a magma or mush body can also induce VT seismicity on any preferentially oriented faults surrounding the intrusion, thereby recording the delivery time and locus of new magma injected into a reservoir (e.g., Roman & Cashman, 2006; Vargas-Bracamontes & Neuberg, 2012).

Earthquakes with longer period seismic signals and low-frequencies (0.5–2 Hz) are thought to be generated near the interface between magma and solid rock (Chouet & Matoza, 2013). The earthquake source proximity to the magma causes the seismic signal to resonate in parts of the plumbing system (e.g., conduits, dykes, and cracks), leading to a reduction in its frequency content (Chouet & Matoza, 2013). These earthquakes can potentially be caused by stick-slip motion between the magma and wall-rock or fracturing of cooling magma near the conduit wall highest (Neuberg *et al.*, 2006; Tuffen *et al.*, 2008). Such earthquakes typically occur at restricted portions of conduits where the magma flow and shear strain rate are highest (Neuberg *et al.*, 2006; Tuffen *et al.*, 2008).

Very long period seismicity (VLP) of 10s of seconds to several minutes period are typically attributed to inertial forces associated with perturbations in the flow of magma and gases through conduits (Chouet & Matoza, 2013). These signals can record the response of the host rock to reservoir inflation and deflation and may be used to model conduit shape and size (Chouet *et al.*, 2008). To do this requires a better understanding of the links between flow processes and resultant pressure/momentum changes using laboratory experiments and numerical models that include the elastic response to magma flow across multiple signal frequency bands (e.g., Thomas & Neuberg, 2012).

6 339 ***Implications and integration***

7
8 340 Studies of evolving reservoirs now aim to link episodes of seismicity related to new magma
9
10 341 injection to petrological evidence for timing of reservoir recharge events, thereby providing
11 342 independent constraints on day to year-long time-scales of magma residence and input prior to
12
13 343 eruptions. For example, Fe-Mg diffusion chronometry modelling of orthopyroxene crystals from the
14
15 344 1980–1986 eruption of Mount St. Helens, ~~which display concentric zoning with either Fe-rich or~~
16
17 345 ~~Mg-rich rims~~, indicates that compositionally distinct rims grew at the same time and generally
18
19 346 within 12 months prior to eruption (Fig. 4) (Saunders *et al.*, 2012). Peaks in crystal growth
20
21 347 correlated extremely well with increased seismicity and SO₂ flux (Fig. 4), confirming the
22 348 relationship between seismicity and magma movement, as well as demonstrating how a
23
24 349 combination of seismicity and petrological information can be used to detect-record-new magma
25
26 350 injections (Saunders *et al.*, 2012).

27
28 351 Petrology and seismicity can also be integrated with other methods, such as GPS and
29
30 352 InSAR. Field *et al.*, (2012) analysed volatiles in melt inclusions trapped in phenocrysts within
31
32 353 peralkaline lavas from historic eruptions at the Dabbahu Volcano in Afar, Ethiopia. Volatile
33 354 saturation pressures at typical magmatic temperatures were constrained to be in the range 43–207
34
35 355 MPa, consistent with the phenocryst assemblage being stable at 100–150 MPa. The interpreted
36
37 356 magma/mush storage depths for these historic eruptions are ~1–5 km, consistent with the depths of
38
39 357 earthquakes associated with reservoir inflation following dyke intrusion in 2005–2006 (Fig. 5)
40
41 358 (Ebinger *et al.*, 2008; Field *et al.*, 2012). Additionally, the best-fit result for modelling of uplift
42
43 359 patterns recorded by InSAR data, which were collected over the same time period as seismicity
44 360 measurement, suggests the magma/mush reservoir comprises a series of stacked sills over a ~1–5
45
46 361 km depth range (Fig. 5) (Ebinger *et al.*, 2008). The consistency of depth estimates based on
47
48 362 petrological study of ancient eruptions, along with the seismicity and inflation of the Dabbahu
49
50 363 Volcano following axial dyke intrusion in 2005–2006, implies a vertically extensive and potentially
51
52 364 long-lived magma/mush storage region. Such multidisciplinary studies demonstrate that joint

1
2
3
4
5
6 365 observations and modelling of seismic signals, petrological data, and other techniques (e.g.,
7
8 366 geodesy and gas emissions) significantly strengthen interpretation of the physical structure,
9
10 367 emplacement, and evolution of magma plumbing systems.

11 368 12 13 369 **2.3. Identifying melt in plumbing systems using seismic imaging**

14 15 370 *Techniques*

16
17 371 Both active and passive source seismological techniques, which utilise man-made seismic events
18
19 372 and natural earthquakes respectively, can be used to identify areas where the presence of partial
20
21 373 melt or magma causes a local reduction in seismic wavespeed, an increase in anisotropy, or an
22 374 increase in attenuation (e.g., Berryman, 1980; Hammond & Humphreys, 2000a, b). With the recent
23
24 375 availability of dense seismic networks, resolution of the crust and mantle seismic velocity structure
25
26 376 has improved to the degree that active source seismic experiments can: (i) use tomographic
27
28 377 techniques to image likely storage regions in the upper crust beneath ocean island volcanoes (e.g.,
29
30 378 Soufrière Hills Volcano, Montserrat; Fig. 6) (Paulatto *et al.*, 2010; Shalev *et al.*, 2010) and,
31
32 379 occasionally, onshore volcanoes (e.g., Mt Erebus, Antarctica, Zandomenighi *et al.*, 2013; Mt. St.
33 380 Helens, Kiser *et al.*, 2014); and (ii) utilise reflected data to image individual sills beneath mid-ocean
34
35 381 ridges (e.g., Kent *et al.*, 2000, Marjanovic *et al.*, 2014). A further example from Katla volcano
36
37 382 Iceland, demonstrates how active source seismic experiments can be used to identify S-wave
38
39 383 shadow zones (i.e. S-waves cannot travel through fluids) and delays in P-waves, which may be used
40
41 384 to infer the location and geometry of shallow-level magma reservoirs (Gudmundsson *et al.*, 1994).

42
43 385 However, recent modelling approaches suggest that the upper crust likely represents only a small
44 386 portion of magma plumbing systems and long-term storage is dominated by mushy zones that
45
46 387 partial melt distributed throughout the lower crust, perhaps in mushes, dominates long-term storage
47
48 388 (e.g., Annen *et al.*, 2006). Active source seismic experiments, particularly on land where the crust is
49
50 389 thick and coverage less uniform, cannot penetrate to these depths efficiently. Furthermore, whilst
51
52 390 seismic tomographic methods using local earthquakes offer 3D images of crustal velocity beneath

1
2
3
4
5
6 391 many volcanoes (e.g., Mt. St. Helens, Waite & Moran, 2009; Askja, Iceland, Mitchell *et al.*, 2013),
7
8 392 they can only resolve areas directly above the deepest earthquakes. Non-uniform coverage thus
9
10 393 makes interpreting tomographic images difficult as resolution varies across the model (see review
11 394 by Lees, 2007).
12

13 395 To illuminate lower crustal regions, seismologists rely on passive seismology. Extending
14
15 396 seismic tomographic images of magma plumbing systems to lower crustal depths requires the use
16
17 397 of teleseismic body-wave and surface wave data, which emanate far (>1000 km) from the
18
19 398 measurement site. However, these data are dominated by longer period signals, meaning their
20
21 399 resolution is relatively low. For example, the Fresnel zone (i.e. the region within $\frac{1}{4}$ seismic
22 400 wavelength and an estimate of the minimum resolvable structure) for active source data at 10 Hz is
23
24 401 on the order of 3 km in the upper crust compared to 10–15 km for 1 Hz teleseismic data used in
25
26 402 receiver function or tomography studies.
27

28 403 29 30 404 **Observations**

31
32 405 Active and passive seismological techniques provide crucial insight into transcrustal melt and
33 406 magma distribution. For example, P-wave seismic travel-time tomography across Monserrat and the
34
35 407 Soufrière Hills Volcano images a series of relatively fast seismic velocity zones, which are
36
37 408 interpreted as solidified andesitic intrusions, surrounded by regions of slow seismic velocities likely
38
39 409 related to either areas of hydrothermal alteration or buried volcanoclastic deposits (Fig. 6) (Paulatto
40
41 410 *et al.*, 2010; Shalev *et al.*, 2010). Within the lower crust, inversions using surface wave data
42
43 411 generated by ambient seismic noise and receiver function data, which isolates P-wave to S-wave
44 412 conversions at major discontinuities in the earth, have identified low shear-wave velocities probably
45
46 413 related to melt presence beneath several volcanic settings (e.g., New Zealand, Bannister *et al.*, 2007;
47
48 414 Toba, Sumatra, Stankiewicz *et al.*, 2010; Ethiopia, Hammond *et al.*, 2011; Jaxybulatov *et al.*, 2014;
49
50 415 Costa Rica, Harmon & Rychert, 2015).
51
52
53
54
55
56
57
58
59
60

1
2
3
4
5
6 416 | When trying to determine how much melt or magma is present, ~~however,~~ numerous studies
7
8 417 | have shown that seismic velocities are ~~much~~ more sensitive to the shapes ~~of that~~ melt/magma-filled
9
10 418 | spaces on a range of scales ~~occupy in the crust (or mantle)~~ compared to the melt fraction (e.g.,
11
12 419 | Hammond & Humphreys, 2000a, b; Miller & Savage, 2001; Johnson & Poland, 2013; Hammond &
13 420 | Kendall, 2016). On the grain-scale, melt commonly wets grain boundaries, forming planar pockets
14
15 421 | In particular, melt distributed on the grain scale and on a macroscopic scale typically retain
16
17 422 | characteristic shapes within the crust, such as melt-wetting grain boundaries (e.g., Takei, 2002;
18
19 423 | Garapic *et al.*, 2013; Miller *et al.*, 2014), whereas on the larger scale magma may form planar
20
21 424 | intrusions the periodic layering of mush in intrusions of either mush (e.g., Annen *et al.*, 2006), or
22 425 | liquid-rich or magma intruding through a dykes or sills. If these melt-distribution features are
23
24 426 | preferentially aligned, they will appear as a distributed region of melt to seismic waves and the
25
26 427 | analyses described will not be able to discriminate between a melt-poor region dominated by
27
28 428 | aligned melt-pockets on grain boundaries and an elongate melt-rich body such as an
29
30 429 | intrusion whether the melt is restricted to grain boundaries or accumulated in intrusions (e.g.,
31
32 430 | Hammond & Kendall, 2016). A further problem is that ~~As the seismic response is more sensitive to~~
33 431 | the geometry of melt distribution, the evolution and movement from small melt fraction blebs or
34
35 432 | tubes to higher melt fraction magma intrusions will cause the relationship between melt fraction and
36
37 433 | seismic velocity to behave non-linearly (Hammond & Humphreys, 2000a, b). Finally, seismic
38
39 434 | velocities are affected by variations in temperature (Jackson *et al.*, 2002), composition (Karato &
40
41 435 | Jung, 1998), and attenuation (Goes *et al.*, 2012), ~~parameters that are all expected to be anomalous in~~
42
43 436 | the presence of partial melt. Relating seismic velocity anomalies to melt fraction is therefore
44
45 437 | difficult without some prior knowledge of melt distribution (Hammond & Kendall, 2016).

46 438 | One possible approach to investigate melt distributions further is through measuring seismic
47
48 439 | anisotropy. If melt has some preferential distribution on a length-length-scale smaller than the
49
50 440 | seismic wavelength, such as a stacked network of sills or an anisotropic permeability on the grain
51
52 441 | scale, then the seismic wavespeed will vary with direction of propagation, i.e. be anisotropic. As a
53
54
55
56
57
58
59
60

1
2
3
4
5
6 442 result, measuring the effects of seismic anisotropy allows inferences ~~on~~about sub-seismic
7
8 443 wavelength structures. ~~leading and understanding the anisotropic characteristics can lead to~~
9
10 444 estimates of the preferential orientation of melt distribution. It is common to observe strong
11
12 445 anisotropy beneath volcanoes and this has been used to place constraints on melt distribution. For
13
14 446 example, high degrees of shear-wave splitting from volcanic earthquakes can either directly map
15
16 447 out regions of significant ~~quantities of melt aligned in pockets~~aligned melt (Keir *et al.*, 2011), or
17
18 448 map out stress changes related to over-pressure from injections of magma into the upper crust (Gerst
19
20 449 & Savage, 2004; Roman *et al.*, 2011). To image the deeper crustal magmatic system, azimuthal
21
22 450 variations in the ratio of P-wave to S-wave speeds (i.e. V_p/V_s) from receiver functions led to the
23
24 451 interpretation that a stacked network of sills is present in the lower crust beneath the Afar
25
26 452 Depression, Ethiopia (Hammond, 2014). Differences in the velocity of Rayleigh Waves and Love
27
28 453 Waves, which are vertically polarised shear-waves and horizontally polarised shear waves
29
30 454 respectively, suggest a similar anisotropic melt distribution is present beneath the Toba Caldera,
31
32 455 Sumatra (Jaxybulatov *et al.*, 2014) and Costa Rica (Harmon & Rychert, 2015).

33 457 ***Implications and integration***

34
35 458 Due to the interference of signals denoting the geometry of melt-filled pockets and the volumetric
36
37 459 proportion of that melt~~Due to the large trade-offs between melt shapes and amounts~~, estimating
38
39 460 melt fraction remains difficult using seismology alone. Some attempt has been made to directly
40
41 461 infer magma/mush reservoir properties from seismic velocities. For example, Paulatto *et al.*, (2012)
42
43 462 used thermal modelling to test ~~what the~~ range of melt fractions that could ~~explain account for~~ the
44
45 463 low velocity zones imaged in the upper crust beneath Soufrière Hills Volcano (Fig. 6), Montserrat
46
47 464 and concluded the melt fraction is between 3 and 10%. However, accounting for resolution of the
48
49 465 tomography, together with uncertainties in the distribution and geometry of melt, means >30% melt
50
51 466 may be present more locally in the low velocity zones defined beneath Soufrière Hills Volcano
52
53 467 (Paulatto *et al.*, 2012). ~~Uncertainties in the distribution and geometry of the melt means this number~~

1
2
3
4
5
6 468 ~~could arguably be considered an upper bound.~~ Possible ways forward involve integrating
7
8 469 seismological data with: (i) petrological data that can place limits on likely melt fractions and/or
9
10 470 emplacement depths (e.g., McKenzie & O’Nions, 1991; Comeau *et al.*, 2016); (ii) geochemical
11 471 techniques that can help determine timescales of melt and magma evolution (e.g., Hawkesworth *et*
12
13 472 *al.*, 2000); and (iii) geodetic or other monitoring data, which helps determine magma movement
14
15 473 (Sturkell *et al.*, 2006). Recent efforts applying industry software, such as full waveform inversions
16
17 474 (FWI; Warner *et al.*, 2013), which is discussed in section 3.1, are also pushing the potential
18
19 475 application of seismological data further and mean that it may be possible to resolve features to sub-
20
21 476 kilometre levels, particularly in the upper crust. Together, these techniques may allow us to directly
22 477 relate seismic velocity anomalies to melt fractions and distributions in the whole crust.
23
24 478

26 479 **2.4. Studying magma plumbing systems using gravimetry**

28 480 ***Techniques***

29
30 481 Gravimetry measures the gravitational field and its changes over space and time, which can be
31
32 482 related to variations in the subsurface distribution and redistribution of mass (e.g., magma). A
33 483 variety of gravimeter instruments (e.g., free-fall, superconducting, and spring-based) and techniques
34
35 484 (e.g., ground-based, sea-floor, ship-borne, and air-borne instrumentations) are available. Spring
36
37 485 gravimeters, where a test mass is suspended on a spring, are mostly used to study magmatic and
38
39 486 volcanic processes in ground-based surveys (e.g., Carbone *et al.*, 2017; Van Camp *et al.*, 2017).
40
41 487 Changes in the gravitational acceleration across a survey area shorten or lengthen the spring, which
42
43 488 is recorded electronically and converted to gravity units. These changes are evaluated across a
44 489 survey network in relation to a reference and are hence termed ‘relative measurements’. Absolute
45
46 490 gravimetry can also be measured, i.e. the value of gravitational acceleration, and serves primarily to
47
48 491 create a reference frame into which other geodetic methods (e.g., InSAR, GNSS, levelling, relative
49
50 492 gravimetry) can be integrated for joint data evaluation. Recent reviews by Carbone *et al.*, (2017)

1
2
3
4
5
6 493 and Van Camp *et al.*, (2017) provide a broad account of gravimetric instruments, measurement
7
8 494 protocols, and data processing relevant for the study of magmatic systems.

9
10 495 Static gravimetric techniques obtain a single snap-shot of the subsurface mass distribution.
11 496 For example, Bouguer anomaly maps are perhaps the best-known products of static gravity surveys
12
13 497 and capture spatial variations in gravity over an area of interest, providing insight into anomalous
14
15 498 mass distribution in the subsurface. Within magmatic studies, computational modelling and
16
17 499 inversion of Bouguer anomaly data allows identification of shallow intrusions (e.g., dykes and sills;
18
19 500 Rocchi *et al.*, 2007), magma-related ore bodies (Hammer, 1945; Bersi *et al.*, 2016), and plutons
20
21 501 (e.g., Figs 7A-7a and Bb) (e.g., Vigneresse, 1995; Vigneresse *et al.*, 1999; Petford *et al.*, 2000)
22 502 exhibiting a density contrast with their host rocks.
23

24 503 In contrast to static surveys, dynamic gravimetric observations allow spatio-temporal mass
25
26 504 changes to be tracked. Dynamic gravimetric studies investigate how the subsurface architecture
27
28 505 changes over time and, ~~thus,~~ is usually performed by measuring variations in gravity across a
29
30 506 network of survey points (e.g., Fig. 7C7c) or, in a few exceptional cases, by installing a network of
31
32 507 continuously operating gravimeters. Dynamic observations demand one-to-two orders of magnitude
33
34 508 higher data precision (i.e. to a few μGal where $1 \mu\text{Gal} = 10^{-8} \text{ m/s}^2$) compared to static surveys,
35 509 making them an elaborate and time-consuming exercise. However, dynamic gravity data yields
36
37 510 important insights into the source processes behind non-tectonic volcano and crustal deformation,
38
39 511 particularly if combined with surface deformation data (e.g., InSAR and GNSS) as subsurface mass
40
41 512 and volume changes can be employed to characterise the density of the material behind the stress
42
43 513 changes (Figs 7C7c-Ff and 8) (e.g., Battaglia & Segall, 2004; Jachens & Roberts, 1985; Poland &
44 514 Carbone, 2016). There are also cases where volcano unrest, due either to magma intrusion into a
45
46 515 ductile host rock or to volatile migration at shallow depths, does not result in resolvable surface
47
48 516 deformation; in these scenarios, gravity data have provided vital clues about subsurface processes
49
50 517 otherwise hidden from conventional monitoring techniques ~~There are also cases where volcano~~
51
52 518 ~~unrest is not characterised by resolvable surface deformation, be it due to magma intrusion into a~~

1
2
3
4
5
6 519 ~~ductile host rock or the porous flow of fluids at shallow depths, but gravity data have provided vital~~
7
8 520 ~~clues about subsurface processes otherwise hidden from conventional monitoring techniques~~ (e.g.,
9
10 521 Gottsmann *et al.*, 2006; Gottsmann *et al.*, 2007; Miller *et al.*, 2017).

11 522 Whilst static and dynamic gravimetric observations offer considerable insight into the
12
13 523 structure and dynamics of magma plumbing systems, care must be exercised when collecting and
14
15 524 interpreting gravity data from active magmatic areas where seasonal variations in hydrothermal
16
17 525 systems, aquifers, or the vadose zone can influence subsurface mass distribution (e.g., Hemmings *et*
18
19 526 *al.*, 2016). These seasonal changes can, in some cases, result in data aliasing artefacts and inhibit
20
21 527 the quantification of ~~deeper-deeper~~-seated magmatic processes (e.g., Gottsmann *et al.*, 2005;
22 528 Gottsmann *et al.*, 2007).

26 530 **Observations**

27
28 531 Gravimetric investigations have been at the heart of studies into the subsurface structure of active
29
30 532 and ancient magma plumbing systems for more than 80 years (e.g., Carbone *et al.*, 2017; Van Camp
31
32 533 *et al.*, 2017). Using techniques initially designed for imaging salt domes, silicic plutons were the
33
34 534 first components of magma plumbing systems to be examined using gravimetry because their low
35 535 density relative to surrounding rocks produces clear, negative gravity anomalies of ~10 to ~40 mGal
36
37 536 amplitude (e.g., Reich, 1932; Bucher, 1944; Bott, 1953). Gravity data have been instrumental in the
38
39 537 investigation of upper-crustal, silicic magma plumbing systems, helping to reveal: (i) the 3D
40
41 538 geometry of plutons by allowing floor morphologies (e.g., flat-floored or wedge-shaped) to be
42
43 539 determined (e.g., Vigneresse *et al.*, 1999; Petford *et al.*, 2000); and (ii) how plutons are constructed,
44 540 for example, by the amalgamation of multiple intrusions fed from depth by dykes (e.g., Vigneresse,
45
46 541 1995). Furthermore, recent high-precision static surveys over active silicic volcanoes have enabled
47
48 542 detailed modelling of the sub-volcanic magma plumbing system, commonly demonstrating the
49
50 543 occurrence of vertically extensive, transcrustal magma bodies (Figs [7A-7a](#) and [Bb](#)) (e.g., Gottsmann
51
52 544 *et al.*, 2008; del Potro *et al.*, 2013; Saxby *et al.*, 2016; Miller *et al.*, 2017). In addition to examining

1
2
3
4
5
6 545 silicic magma plumbing systems, negative gravity anomalies with typical amplitudes of up to 60
7
8 546 mGal and up to 100 km wavelength can be associated with, and provide insight into, the geometry
9
10 547 and size of silicic ash-flow calderas (e.g., Eaton *et al.*, 1975; Masturyono *et al.*, 2001). Positive
11 548 gravity anomalies with amplitudes of up to 30 mGal and wavelengths of up to 20 km are
12
13 549 commonly identified at mafic volcanoes and likely result from dense intrusive complexes (e.g.,
14
15 550 Rymer & Brown, 1986).

16
17 551 Dynamic gravity observations have provided unprecedented insight into the evolution of
18
19 552 magma plumbing systems over timescales of seconds to decades, including: (i) the characterisation
20
21 553 of multi-year lava lake dynamics (e.g., Poland & Carbone, 2016); (ii) mass budgets of magma
22 554 intrusions (e.g., Fig. 8) (e.g., Battaglia *et al.*, 1999; Jousset *et al.*, 2000; Rymer *et al.*, 2005;
23
24 555 Bonforte *et al.*, 2007; Tizzani *et al.*, 2009); (iii) shallow hydrothermal fluid flow processes induced
25
26 556 by deeper magmatic unrest (e.g., Battaglia *et al.*, 2006; Gottsmann *et al.*, 2007; Miller *et al.*, 2017);
27
28 557 and (iv) parameters of magmatic geothermal reservoirs (e.g., Hunt & Bowyer, 2007; Sofyan *et al.*,
29
30 558 2011). For example, using data from a network of continuously recording gravimeters, Carbone *et*
31
32 559 *al.*, (2013) calculated the density of the Kilauea lava lake as $950 \pm 300 \text{ kg m}^{-3}$, i.e. similar to and
33 560 potentially less than that of water, suggesting that the magma column within the upper portions of
34
35 561 the volcanic edifice is gas-rich. Because density and volatile content are critical controls on magma
36
37 562 rheology, identification of a gas-rich magma column and lava lake at Kilauea is crucial to modelling
38
39 563 and understanding convection and eruption dynamics (Carbone *et al.*, 2013).

40 41 564 42 43 565 **Implications and integration**

44 566 The advent of data-rich geodetic observations from satellite-remote sensing (e.g., InSAR), in
45
46 567 conjunction with spatio-temporal gravity studies, provides unprecedented opportunities to
47
48 568 characterise magma plumbing system dynamics and the driving mechanisms behind volcano
49
50 569 deformation. At Long Valley caldera, for example, a residual gravity increase of more than $60 \mu\text{Gal}$
51
52 570 between 1982 and 1999 indicates a mass addition at depth (Battaglia *et al.*, 1999). Joint inversion of
53
54
55
56
57
58
59
60

1
2
3
4
5
6 571 InSAR and gravity data from Long Valley derives a best fit-source density of 2509 kg m³ and is
7
8 572 indicative of a magmatic intrusion (Fig. 8) (Tizzani *et al.*, 2009). At the deforming Laguna del
9
10 573 Maule volcanic centre, Chile, multi-year InSAR and dynamic gravity records demonstrate **that**
11 574 uplift and extension above an inflating sill-like reservoir at ~5 km depth promoted migration of
12
13 575 hydrothermal fluids along a fault to shallow (1–2 km) depths (Miller *et al.*, 2017). Alternatively,
14
15 576 although no ground deformation is observed at Tenerife, Spain, deconvolution of dynamic gravity
16
17 577 into a shallow and deep gravity field provides **e**vidence of unrest (Prutkin *et al.*, 2014). The gravity
18
19 578 data suggest hybrid processes have generated the unrest, whereby fluids were released and migrated
20
21 579 upward along deep-rooted faults from an intrusion at ~9 km beneath the summit of Teide Volcano
22 580 (Prutkin *et al.*, 2014). Overall, combining ground deformation and gravimetric observations has
23
24 581 highlighted complex processes both within magma reservoirs (e.g., mass addition by magma input,
25
26 582 density decrease by volatile exsolution, or density increase by crystallisation; Figs **7C7c-Ff**) and **in**
27
28 583 the surrounding host rock (e.g., migration of magmatic fluids, phase changes in hydrothermal
29
30 584 systems). Key to a better understanding of the processes governing these magma plumbing system
31
32 585 and volcano deformation dynamics is the integration of gravimetric and geodetic data with other
33
34 586 geophysical data (e.g., seismicity or magnetotellurics) and petrological **and geochemical** data.
35 587 Coupled with advanced numerical modelling, such multi-parameter studies promise exciting new
36
37 588 insights into the inner workings of sub-volcanic magma plumbing systems (e.g., Currenti *et al.*,
38
39 589 2007; Hickey *et al.*, 2016; Currenti *et al.*, 2017; Gottsmann *et al.*, 2017; Miller *et al.*, 2017).
40
41 590

42 591 **2.5. Resolving magma plumbing system structure with electromagnetic methods**

44 592 ***Techniques***

46 593 Electromagnetic (EM) methods probe subsurface electrical resistivity or its inverse, i.e. electrical
47
48 594 conductivity. Spatial variations in resistivity control the position, strength, and geometry of local
49
50 595 electrical eddy currents and the magnetic fields they produce. These electrical eddy currents are
51
52 596 induced by time-varying, naturally occurring magnetic fields external to Earth, which forms the
53
54
55
56
57
58
59
60

1
2
3
4
5
6 597 basis of the magnetotelluric (MT) technique, or by controlled sources. Monitoring these decaying
7
8 598 electrical and magnetic fields with passive MT techniques therefore allows the subsurface resistivity
9
10 599 distribution to be inferred. Controlled source methods generally probe only the shallow subsurface,
11
12 600 but MT has a greater depth range as its uses ~~longer-longer~~-period signals to penetrate deeper. The
13
14 601 signals propagate diffusively, which means EM methods typically have a lower resolution than
15
16 602 seismic techniques. -However, melt, magma, and magmatic hydrothermal fluids are generally
17
18 603 considerably less resistive (~~i.e. they are more conductive~~) than solid rock and can thus easily be
19
20 604 detected by EM methods, which are sensitive to conductive materials (e.g., Whaler & Hautot, 2006;
21
22 605 Wannamaker *et al.*, 2008; Desissa *et al.*, 2013; Comeau *et al.*, 2015). EM methods, particularly MT,
23
24 606 have therefore been used extensively to study magmatic systems in various tectonic settings.

25
26 607 MT equipment, data acquisition, and processing is described by Simpson & Bahr (2005) and
27
28 608 Ferguson (2012). Measured field variations have very low amplitudes, meaning equipment needs to
29
30 609 be positioned and installed carefully ~~to, avoiding steep topography, to~~ reduce vibrational (e.g., from
31
32 610 wind, vegetation, or vehicles) and electrical (e.g., from power lines) noise. If data are recorded
33
34 611 synchronously at a second, less noisy site, remote reference methods can be used to improve the
35
36 612 data quality (e.g., Gamble *et al.*, 1979). ~~An additional control on quality is that seawater is a good
37
38 613 electrical conductor and can strongly influence the data, although the availability of higher quality
39
40 614 bathymetry models (and the computational power to use them) does allow corrections to be made.~~

41
42 615 One further problem is that small-scale resistivity anomalies in the shallow subsurface generate
43
44 616 galvanic (non-inductive) effects that distort MT data. The distortion is identified and corrected for,
45
46 617 which may involve using controlled source transient electromagnetic data to ensure complete
47
48 618 removal (e.g. Sternberg *et al.*, 1988), at the same time as assessing whether the data can be
49
50 619 modelled with a one-, two- or three-dimensional resistivity structure (e.g. Jones, 2012). Failure to
51
52 620 remove galvanic distortion can result in models having resistivity features at the wrong depth. For
53
54 621 example, there has been controversy as to whether a conductor beneath Vesuvius Volcano, Italy is
55
56 622 caused by a deep (~8–10 km depth) magma reservoir (Di Maio *et al.*, 1998) or a shallow brine layer
57
58
59
60

1
2
3
4
5
6 623 (Manzella *et al.*, 2004). All of these factors can be a significant problem when using MT to study
7
8 624 magmatic systems, especially on volcanic islands.

9
10 625 The relationship between MT data and subsurface resistivity is strongly non-linear meaning
11 626 that inversion is fundamentally non-unique and computationally expensive (e.g., Bailey, 1970;
12
13 627 Parker, 1980; Weaver, 1994). Most practical algorithms for inverting MT data obtain a unique
14
15 628 result by minimising a combination of misfit to the data and a measure of model roughness (e.g.,
16
17 629 Constable *et al.*, 1987). This approach poorly delimits how magma is distributed in the subsurface,
18
19 630 whether it is in sills, dykes, or larger reservoirs (Johnson *et al.*, 2016). Whilst MT data are sensitive
20
21 631 to the top surface of a conductor, its base may not be detected becauseas conductive material
22 632 reduces the penetration depth of the signal. Sensitivity analysis is used to ascertain the model
23
24 633 features required to fit the MT data, which allows a conductor to be confined to a certain depth
25
26 634 range and thereby constrains its base (e.g., Desissa *et al.*, 2013). Furthermore, if the resistivity of a
27
28 635 conductor can be inferred, its conductance (i.e. a product of thickness and conductivity) can be used
29
30 636 to determine its thickness (e.g., Comeau *et al.*, 2016).

31 32 637 33 638 **Observations**

34
35 639 EM induction surveys have been conducted on most major sub-aerial volcanoes and magmatic
36
37 640 systems; only a few will be mentioned here to illustrate the type information on magma plumbing
38
39 641 systems that has been obtained. MT data have been used to image several low resistivity features in
40
41 642 the central Andes, particularly beneath the uplifting (10–15 mm/yr) Volcán Uturuncu, Bolivia (Fig.
42
43 643 9A9a) (Comeau *et al.*, 2015; Comeau *et al.*, 2016). The deepest of these bodies has resistivities of
44 644 $<3 \Omega \text{ m}$, has a top contact at ~15–20 km depth (i.e. it is shallowest beneath Uturuncu), likely has a
45
46 645 thickness of $>6 \text{ km}$, and extends E-W for ~170 km (Fig. 9) (Comeau *et al.*, 2015; Comeau *et al.*,
47
48 646 2016). This large-scale structure is interpreted to be the Altiplano-Puna magma body (APMB),
49
50 647 which has been identified in other geophysical datasets (e.g., Fig. 7A7a) (e.g., gravimetry, del Potro
51
52 648 *et al.*, 2013), with its low resistivity attributed to the presence of at least 20% andesitic melt and/or

1
2
3
4
5
6 649 magma. Extending from the top of the APMB towards the surface are several vertical, narrow (<10
7
8 650 km wide), low resistivity (<10 Ω m) zones that coincide with areas of seismicity and negative
9
10 651 gravity anomalies (Fig. 9). These zones likely reflect a network of dykes and upper crustal magma
11
12 652 reservoirs (Jay *et al.*, 2012; del Potro *et al.*, 2013; Comeau *et al.*, 2015; Comeau *et al.*, 2016).

13 653 Monitoring of magmatic systems can also be undertaken by both time-lapse and continuous
14
15 654 EM measurement. For example, MT data collected immediately after the 1977–1978 eruption at
16
17 655 Usu volcano, Japan revealed a conductive zone (<100 Ω m) beneath the summit that probably
18
19 656 corresponded to intruded magma. By 2000, MT data revealed that this conductive body had become
20
21 657 resistive (500–1000 Ω m) as the intrusion cooled, from 800°C to 50°C, and crystallised
22
23 658 (Matsushima *et al.*, 2001). Continuous MT monitoring of Sakurajima volcano, Japan between May
24
25 659 2008 and July 2009 revealed temporal changes in resistivity of $\pm 20\%$, some of which correlated to
26
27 660 periods of surface deformation and were inferred to reflect mixing between groundwater and
28
29 661 volatiles exsolved from an underlying magma body (Aizawa *et al.*, 2011). Continuous MT
30
31 662 monitoring at La Fournaise, Réunion Island recorded apparent resistivity decreases associated with
32
33 663 the large 1998 eruption, which were attributed to the injection of a N-S striking dyke (Wawrzyniak
34
35 664 *et al.*, 2017).

36
37 665 Several EM studies have focussed on magma plumbing systems at divergent margins,
38
39 666 including mid-ocean ridges and continental rifts. For example, at the fast-spreading East Pacific
40
41 667 Rise ~~mid-ocean ridge~~, a ~ 10 km wide, sub-vertical conductor, slightly displaced from the ridge axis
42
43 668 and connected to a deep, broad conductive zone was interpreted as a channel efficiently transporting
44
45 669 melt to the base of the crust (Baba *et al.*, 2006; Key *et al.*, 2013). Imaging of a crustal conductor for
46
47 670 the first time beneath a slow-spreading ridge, i.e. the Reykjanes ridge in the Atlantic Ocean,
48
49 671 suggests that magma injection into crustal reservoirs is intermittent but rapid (MacGregor *et al.*,
50
51 672 1998; Heinson *et al.*, 2000). Conversely, slow-spreading continental rifting in the Dabbahu magma
52
53 673 segment, Afar, Ethiopia appears to be underlain by a large conductor, either at the top of the mantle
54
55 674 or straddling the Moho, containing more melt (>300 km³) than is intruded into the magma plumbing
56
57
58
59
60

1
2
3
4
5
6 675 system during a typical rifting episode (Desissa *et al.*, 2013). The volume of this large conductor
7
8 676 implies it is a long-lived feature that could source magmatic activity for tens of thousands of years
9
10 677 (Desissa *et al.*, 2013).

11 678 12 13 679 ***Implications and integration*** 14

15 680 It is clear from MT studies of the APMB that other geophysical techniques aid and/or corroborate
16
17 681 data interpretation (Fig. 9) (e.g., Comeau *et al.*, 2015; Comeau *et al.*, 2016). Over the last two
18
19 682 decades, numerous geophysical studies have been applied to examine magma and melt distribution
20
21 683 beneath various portions of the East African Rift, providing an excellent opportunity to test how
22 684 different techniques and data can be integrated. For example, extensive zones of melt beneath the
23
24 685 Afar region in Ethiopia inferred from MT data by Desissa *et al.*, (2013) is supported by: (i) the
25
26 686 occurrence of coincident, low P-wave velocity (down to 7.2 km s^{-1}) zones identified using from
27
28 687 analysis of seismic Pn waves that propagate along the Moho (Stork *et al.*, 2013); (ii) surface wave
29
30 688 studies that reveal lower crustal areas in magmatic domains with low S-wave velocities ($\sim 3.2 \text{ km s}^{-1}$) (Guidarelli *et al.*, 2011); and (iii) high anisotropic V_p/V_s ratios and low amplitude receiver
31
32 689 functions, which are indicative of the presence of melt ~~presence~~ (Hammond *et al.*, 2011; Hammond,
33 690 | 2014). Similarly, crustal conductors along the northern flanks of the Main Ethiopian Rift,
34
35 691 interpreted to represent melt/magma (Whaler & Hautot, 2006; Samrock *et al.*, 2015; Hübner *et al.*,
36
37 692 2018), coincide with locations where receiver functions either have amplitudes too low to interpret
38
39 693 or indicate high V_p/V_s values (Dugda *et al.*, 2005; Stuart *et al.*, 2006). Electrical anisotropy can be
40
41 694 inferred directly from MT data consistent with a two-dimensional subsurface resistivity distribution
42
43 695 (Padilha *et al.*, 2006; Hamilton *et al.*, 2006). Large amounts of electrical anisotropy were found ~~at~~
44 696 | periods sampling in the lower crust beneath Quaternary magmatic segments in Afar, Ethiopia, where
45
46 697 there is also significant crustal seismic anisotropy (see Fig. 11 of Ebinger *et al.*, 2017); oriented
47
48 698 melt-filled pockets are the probable cause of both.
49
50 699
51
52
53
54
55
56
57
58
59
60

1
2
3
4
5
6 700 Although EM methods can image subsurface conductors that are interpreted to represent
7
8 701 magma bodies or zones of partial melt (i.e. crystal mushes), additional information is required to
9
10 702 determine their composition, volume, and/or melt fraction. However, there are several challenges in
11 703 inverting measured bulk resistivities to recover this information. Two-phase mixing laws predict
12
13 704 bulk resistivity is primarily a function of melt resistivity and geometry in the rock matrix when the
14
15 705 fluid phase ~~has~~ low resistivity, as in the case of partial melt. Well-connected melt gives a lower
16
17 706 bulk resistivity than isolated melt pockets, for the same melt fraction and resistivity (e.g. Hashin &
18
19 707 Shtrikman, 1963; Roberts & Tyburczy, 1999; Schmeling, 1986). Whilst resistivities of basaltic and
20
21 708 rhyolitic melts have been measured in laboratory experiments (e.g., Laumonier *et al.*, 2015; Guo *et*
22 709 *al.*, 2016), they are strongly dependent on temperature, pressure, silica, sodium and water content,
23
24 710 making extrapolation uncertain, ~~although~~ The web-based SIGMELTS tool can, however, be used
25
26 711 to (Pommier & Le Trong, 2011), predicts melt and bulk resistivities for a wide range of
27
28 712 compositions and conditions (Pommier & Le Trong, 2011). Importantly, petrological and
29
30 713 geochemical characterisation of eruptive products can help inform interpretations of associated,
31
32 714 subsurface conductors but it is difficult to ascertain either whether if their composition reflects the
33
34 715 current magma/melt present in the plumbing system or whether melt pockets are interconnected.
35 716 These large uncertainties in melt resistivity and the requirement to make assumptions ~~of~~ about its
36
37 717 geometry make direct inference of melt fraction difficult. Nonetheless, information from laboratory
38
39 718 studies, petrology, and geochemistry aids interpreting resistivity anomalies in magmatic regions
40
41 719 (see review by Pommier, 2014).

44 721 **2.6. Imaging ancient magma plumbing systems in seismic reflection data**

46 722 ***Techniques***

48 723 Over the last two decades, major advances have been made in imaging deep crustal melt beneath
49
50 724 active volcanic terrains using P- and S-wave tomographic data (e.g., Yellowstone, Husen *et al.*,
51
52 725 2004; Mt. St. Helens, Lees, 2007; Hawaii, Okubo *et al.*, 1997). These data image deep (>7 km),
53
54
55
56
57
58
59
60

1
2
3
4
5
6
7
8
9
10
11
12
13
14
15
16
17
18
19
20
21
22
23
24
25
26
27
28
29
30
31
32
33
34
35
36
37
38
39
40
41
42
43
44
45
46
47
48
49
50
51
52
53
54
55
56
57
58
59
60

often laterally extensive (up to 20 km), sill-like magma reservoirs (e.g., Paulatto *et al.*, 2012). However, like many geophysical and geodetic techniques applied to study active magma plumbing systems, these data typically lack the spatial resolution to resolve the detailed geometry of pathways transporting magma to the Earth's surface. Active source seismic reflection data, which have a spatial resolution of metres-to-decametres down to depths of ~5 km, can provide unprecedented images of and insights into the geometry and dynamics of shallow-level, crystallised, magma plumbing systems (e.g., Fig. 10) (e.g., Planke *et al.*, 2000; Smallwood & Maresh, 2002; Thomson & Hutton, 2004; Cartwright & Hansen, 2006; Jackson *et al.*, 2013; Magee *et al.*, 2016; Schofield *et al.*, 2017). Whilst seismic reflection data are traditionally used to find and assist in the production of hydrocarbons in sedimentary basins (Cartwright & Huuse, 2005), we here discuss and support its application to volcanological problems.

Acquiring active source seismic reflection data involves firing acoustic energy (i.e. seismic waves) into the subsurface and measuring the surface arrival times (i.e. the travel-time) of reflected energy. Processing of these arrival time data allows reconstruction of the location and geometry of the geological interfaces from which acoustic energy was reflected. Mafic intrusive igneous rocks are generally well-imaged in seismic reflection data because they typically have greater densities (>2.5 g/cm³) and acoustic velocities (i.e. >4000 m s⁻¹) than encasing sedimentary strata; these differences result in a high acoustic impedance contrast, causing more seismic energy to be reflected back to the surface compared to low acoustic impedance boundaries (Smallwood & Maresh, 2002; Brown, 2004). In contrast, ~~evolved~~ silicic igneous rocks have similar acoustic properties to encasing sedimentary strata, meaning that felsic intrusions are rarely imaged in seismic reflection data (Mark *et al.*, 2017; Rabbel *et al.*, 2018). Furthermore, because reflection seismology relies on the return of acoustic energy to the surface, seismic reflection data favourably image mafic, sub-horizontal-to-moderately inclined intrusions (e.g., sills, inclined sheets, and laccoliths; Smallwood & Maresh, 2002; Jackson *et al.*, 2013; Magee *et al.*, 2016). Sub-vertical dykes reflect only a limited amount of acoustic energy back to the surface and are thus typically poorly imaged in

1
2
3
4
5
6 752 seismic reflection data (e.g., Smallwood & Maresh, 2002; Planke *et al.*, 2005; Thomson, 2007; Wall
7
8 753 *et al.*, 2010; Eide *et al.*, 2017a; Phillips *et al.*, 2017).

9
10 754
11 755 **Observations**
12

13 756 Sills and inclined sheets are commonly observed in seismic reflection data as laterally
14
15 757 discontinuous, high-amplitude reflections, which may cross-cut the host rock strata (Fig. 10) (e.g.,
16
17 758 Symonds *et al.*, 1998, Smallwood & Maresh, 2002; Planke *et al.*, 2005, Magee *et al.*, 2015). Many
18
19 759 of the sills and inclined sheets imaged in seismic reflection data are, however, expressed as tuned
20
21 760 reflection packages, whereby discrete reflections from the top and base contacts interfere on their
22 761 | return to the surface and cannot be distinguished (e.g., Figs 10 and ~~10A-11a~~) (e.g., Smallwood &
23
24 762 Maresh, 2002; Peron-Pinvidic *et al.*, 2010; Magee *et al.*, 2015; Eide *et al.*, 2017a; Rabbel *et al.*,
25
26 763 | 2018). It is therefore difficult to assess either intrusion thicknesses, or to detect whether if imaged
27
28 764 sills are composite bodies made of numerous, stacked, thin sheets. Either way, subtle vertical offsets
29
30 765 and corresponding amplitude variations of sill reflections can often be mapped, defining linear
31
32 766 structures that radiate out from either the central, deepest portions of sills or areas where underlying
33 767 intrusions intersect the sill (e.g., Schofield *et al.*, 2012a; Magee *et al.*, 2014; Magee *et al.*, 2016).
34
35 768 These structures are interpreted to relate to magma flow indicators such as intrusive steps, broken
36
37 769 bridges, and magma fingers (e.g., Schofield *et al.*, 2010; Schofield *et al.*, 2012b; Magee *et al.*,
38
39 770 2018).

40
41 771 A recurring observation from seismic reflection-based studies of extinct and buried intrusive
42
43 772 systems is that complexes of interconnected sills and inclined sheets, which may cover $>3 \times 10^6$
44 773 | km², can dominate magma plumbing systems (e.g., Fig. ~~10A-10b~~) (e.g., Svensen *et al.*, 2012, Magee
45
46 774 *et al.*, 2016). Importantly, where buried volcanic edifices are imaged in seismic reflection data, they
47
48 775 rarely appear to be underlain by ‘magma chambers’ (i.e. a spheroidal or ellipsoidal body of now-
49
50 776 crystallised magma). Instead, these imaged volcanoes commonly appear laterally offset from
51
52 777 genetically related sills and/or laccoliths that are inferred to represent their feeder reservoirs (e.g.,
53
54
55
56
57
58
59
60

1
2
3
4
5
6 778 | Fig. ~~H10b~~10b) (Magee *et al.*, 2013a; McLean *et al.*, 2017). The geometry, location, and connectivity
7
8 779 | of these intrusions, which can represent magma storage sites and conduits to the surface, are often
9
10 780 | heavily influenced by both the host rock structure and lithology (see review by Magee *et al.*, 2016).
11
12 781 | For example, magma may flow along pronounced discontinuities (e.g., bedding) or within specific
13
14 782 | stratigraphic units (e.g., coal) for considerable distances, occasionally ~~abruptly~~ climbing to higher
15
16 783 | stratigraphic levels by instigating deformation of the host rock or by exploiting pre-existing faults
17
18 784 | (e.g., Jackson *et al.*, 2013; Magee *et al.*, 2016; Schofield *et al.*, 2017; Eide *et al.*, 2017b). It is clear
19
20 785 | from seismic reflection data that shallow-level tabular intrusions are commonly accommodated by
21
22 786 | roof uplift to form a flat-topped or dome-shaped forced fold (e.g., Figs ~~H11a~~11a and ~~Bb~~Bb) (e.g.,
23
24 787 | Trude *et al.*, 2003; Hansen & Cartwright, 2006; Jackson *et al.*, 2013; Magee *et al.*, 2013b).
25
26 788 | Moreover, if the age of reflections onlapping onto these intrusion-induced forced folds can be
27
28 789 | ascertained, the timing and to some extent the duration of magmatic activity can be determined
29
30 790 | (e.g., Trude *et al.*, 2003; Hansen & Cartwright, 2006; Magee *et al.*, 2014; Reeves *et al.*, 2018).
31
32 791 | Although most seismic-based studies examine intrusions within sedimentary basins, saucer-shaped
33
34 792 | sills and laterally extensive sill-complexes emplaced into crystalline basement rock are also imaged
35
36 793 | (e.g., Ivanic *et al.*, 2013; McBride *et al.*, 2018). Lastly, seismic reflection data can also be used to
37
38 794 | image the internal structure of layered ultramafic-mafic intrusions (e.g., the Bushveld Layered
39
40 795 | Intrusion, Malehmir *et al.*, 2012) and, in some instances, identify dykes (e.g., Fig. ~~H11c~~11c) (e.g.,
41
42 796 | Wall *et al.*, 2010; Abdelmalak *et al.*, 2015; Bosworth *et al.*, 2015; Phillips *et al.*, 2017).
43
44 797

43 798 | **Implications and integration**

44 799 | Despite being limited in terms of their spatial resolution (typically a few tens of metres) and ability
45
46 800 | to image steeply dipping features (i.e. dykes), they provide unprecedented snapshots into the final
47
48 801 | 3D structure of magma plumbing systems. Beyond quantifying the structure and connectivity of
49
50 802 | magma plumbing systems, seismic-based studies have shown that: (i) magma flow patterns mapped
51
52 803 | across entire sill-complexes indicate they can transport melt from source to surface over great
53
54
55
56
57
58
59
60

1
2
3
4
5
6 804 lateral (>100's km) and vertical distances (10's km), potentially without significant input from
7
8 805 dykes (Fig. [10A-10a](#)) (e.g., Thomson & Hutton, 2004; Cartwright & Hansen, 2006; Magee *et al.*,
9
10 806 2014; Magee *et al.*, 2016; Schofield *et al.*, 2017); and (ii) a variety of elastic and inelastic
11 807 mechanisms can accommodate host rock deformation during magma emplacement, meaning that
12
13 808 the location and size of ground deformation does not necessarily equal that of the forcing intrusion
14
15 809 (e.g., Jackson *et al.*, 2013, Magee *et al.*, 2013b). Importantly, observations from seismic reflection
16
17 810 data highlight that the lateral dimension should be considered when modelling the transit of magma
18
19 811 in the crust, posing problems for the widely held and simple assumption that magma simply travels
20
21 812 vertically from melt source to eruption site.

22 813 Seismic-based studies have also shown that direct comparison to active deformation
23
24 814 structures can be informative. For example, through comparing mapped lava flows and structures
25
26 815 associated with the Alu dome to similar features observed in seismic reflection data (see section
27
28 816 2.6), Magee *et al.*, (2017) concluded that the shallow-level sill likely has a saucer-shaped, as
29
30 817 opposed to the sill-like tabular morphology inferred from an episode of deformation measured using
31
32 818 InSAR (Figs [3C-3c](#) and [Dd](#)). Despite its benefits, it is important to remember that seismic reflection
33
34 819 data typically reveal only the final geometry of the magma plumbing system. There thus remains a
35 820 challenge in using these data to understand areas where deformation captures potentially transient,
36
37 821 active processes, rather than structures resulting from (multiple) periods of intrusion and cooling
38
39 822 (Reeves *et al.*, 2018). One potential and exciting way forward [here](#) is the development of Virtual
40
41 823 Reflection Seismic Profiling, [where-by-which](#) microseismicity at active volcanoes may [potentially](#)
42
43 824 be used to image magma reservoirs and subsurface structure in 4D (Kim *et al.*, 2017). Although
44
45 825 challenges exist in dataset integration, the imaging power afforded by modern seismic reflection
46 826 data thus presents a unique opportunity to further unite field-, petrological-, geochemical-, and other
47
48 827 geophysical-based analyses within more realistic structural frameworks (e.g., Figs 3, [11A-11a](#) and
49
50 828 [Bb](#)). In our view, however, seismic reflection data are under-utilized in igneous research, remaining
51
52 829 an unfamiliar technique to many Earth Scientists in the volcanic and magmatic community.

1
2
3
4
5
6 830
7
8 831 **2.7. Rock magnetism**

9
10 832 ***Technique***

11 833 Whilst seismic reflection data provide unique 3D images of ancient magma plumbing systems,
12
13 834 which can be used to infer magma flow patterns across entire intrusion networks, we commonly
14
15 835 lack sufficient data (e.g., boreholes) to test seismic-based hypotheses. It is therefore critical to
16
17 836 compare seismic interpretations to field analogues where magma flow patterns, emplacement
18
19 837 mechanics, and intrusion evolution can be investigated via other techniques. In this section, we
20
21 838 examine how rock magnetic analyses can be used to systematically study magnetic mineralogy and
22 839 petrofabrics, thereby illuminating the structure and history of igneous intrusions.
23

24 840 There are two principal types of rock magnetic study; magnetic remanence and magnetic
25
26 841 susceptibility, where the total magnetisation (M) of a rock is the sum of the magnetic remanence
27
28 842 (M_{rem}) and the induced magnetisation (M_{ind}), which is a product of the susceptibility (K) and
29
30 843 applied field strength (H) (Dunlop & Özdemir, 2001). Remanence carries a geological record of the
31
32 844 various magnetisations acquired over time and is central to palaeomagnetic studies. However, we
33 845 focus on magnetic fabric analysis, which relies on measurements of the anisotropy of magnetic
34
35 846 susceptibility (AMS). The AMS signal of a rock carries information from all constituent grains.
36
37 847 Although mineral phases that have a paramagnetic behaviour (i.e. they are weakly attracted to
38
39 848 externally applied magnetic fields) volumetrically dominate most igneous rocks (e.g., olivine,
40
41 849 clinopyroxene, ~~feldspars~~, biotite), ferromagnetic mineral phases (e.g., titanomagnetite) are highly
42
43 850 susceptible to magnetization and therefore tend to dominate K (e.g., Dunlop & Özdemir, 2001;
44
45 851 Biedermann *et al.*, 2014). Magnetic fabrics therefore typically reflect the preferential orientation of
46 852 crystallographic axes (i.e. crystalline anisotropy), the shape-preferred orientation of individual
47
48 853 crystals (i.e. shape anisotropy), and/or the alignment of closely spaced crystals (i.e. distribution
49
50 854 anisotropy) belonging to Fe-bearing silicate and oxide phases (e.g., Voight & Kinoshita, 1907;
51
52 855 Graham, 1954; Hrouda, 1982; Tarling & Hrouda, 1993; Dunlop & Özdemir, 2001). The principal
53
54
55
56
57
58
59
60

1
2
3
4
5
6 856 axes of the magnetic fabrics measured by AMS can thus be related to the orientation, shape, and
7
8 857 distribution of individual grains (i.e. the petrofabric) (e.g., Fig. [12A.12a](#)).

9
10 858 Regardless of whether mineral phases crystallise early or late, whereby their orientation and
11 859 distribution typically mimics the earlier silicate framework, it is expected that the initial petrofabric
12
13 860 developed in intrusive rocks will likely be sensitive to alignment of crystals during primary magma
14
15 861 flow. However, it is also critical to recognise that later magmatic processes (e.g., convection and
16
17 862 melt extraction) and syn- or post-emplacement tectonic deformation can modify or overprint
18
19 863 primary magma flow fabrics during intrusion, solidification (i.e. mush development), or sub-solidus
20
21 864 conditions (e.g., Borradaile & Henry, 1997; Bouchez, 1997; O'Driscoll *et al.*, 2015; Kavanagh *et*
22 865 *al.*, 2018). Whilst anisotropy of magnetic susceptibility (AMS) can thus rapidly and accurately
23
24 866 detect weak or subtle mineral alignments within igneous intrusions, which may be attributable to
25
26 867 magmatic and/or tectonic processes, evaluating the origin and evolution of petrofabric development
27
28 868 requires additional information (e.g., Borradaile & Henry, 1997; Bouchez, 1997). For example,
29
30 869 shape-preferred orientation analyses and comparison to visible flow indicators (e.g., intrusive steps
31
32 870 and bridge structures) allow magma flow axes and directions that have been inferred from magnetic
33
34 871 fabrics to be verified (e.g., Launeau & Cruden, 1998; Callot *et al.*, 2001; Magee *et al.*, 2012a). For a
35 872 useful précis of AMS-related magnetic theory in igneous rocks, the reader is referred to early works
36
37 873 by Balsey & Buddington (1960) and Khan (1962), and more recent summaries provided by Martín-
38
39 874 Hernández *et al.*, (2004), O'Driscoll *et al.*, (2008), and O'Driscoll *et al.*, (2015).

40
41 875 The principle behind AMS relies on the measurement of the bulk susceptibility (K_m) of a
42
43 876 single sample in different orientations to determine the susceptibility anisotropy tensor, which
44
45 877 relates the induced magnetisation (M_{ind}) to the applied field (H) in three dimensions (Tarling &
46 878 Hrouda, 1993). The orientation and magnitude of the eigenvectors and eigenvalues of this tensor
47
48 879 define an ellipsoid with three principal axes; the long axis of the ellipsoid, K_1 , defines the magnetic
49
50 880 lineation and the short axis, K_3 , defines the normal (i.e. the pole) to the magnetic foliation plane
51
52 881 (K_1 – K_2 ; Fig. [11A.12a](#)) (Stacy *et al.*, 1960; Khan, 1962; Tarling & Hrouda, 1993). In order to
53
54
55
56
57
58
59
60

1
2
3
4
5
6 882 interpret magnetic fabrics, it is important to determine the mineralogy of the phases carrying the
7
8 883 magnetic signal because the composition, grain size, and distribution of magnetically dominant
9
10 884 minerals (e.g., titanomagnetite) can control fabric orientation (e.g., Hargreaves *et al.*, 1991;
11 885 Stephenson, 1994; Dunlop & Özdemir, 2001). In addition to primary crystallographic and textural
12
13 886 controls on magnetic fabrics, subsequent oxidation of remaining melt and secondary hydrothermal
14
15 887 alteration can affect the magnetic mineralogy and, thereby, the AMS signal (e.g., Trindade *et al.*,
16
17 888 2001; Stevenson *et al.*, 2007a). A variety of rock magnetic experiments are thus required to
18
19 889 determine the magnetic mineralogy. The most widely used method involves measuring
20
21 890 susceptibility, and thereby behaviour of magnetic materials, at varying temperatures ranging from -
22 891 200°C to 700°C (i.e. thermomagnetic analysis *sensu* Orlický, 1990; Hrouda *et al.*, 1997). For
23
24 892 example, paramagnetic materials (e.g., biotite) follow the Curie-Weiss law, whereby their
25
26 893 susceptibility drops hyperbolically with increasing temperature. In contrast, the thermomagnetic
27
28 894 curve of ferromagnetic materials (e.g., titanomagnetite) displays little change in susceptibility with
29
30 895 temperature, apart from when characteristic crystallographic transitions occur (e.g., the Curie point
31
32 896 for pure magnetite at ~580°C, Petrovský & Kapička, 2006) temperature. To determine the grain size
33 897 of ferromagnetic fraction in the magnetic susceptibility signal, the hysteretic property of the
34
35 898 magnetisation is important (Dunlop, 2002). Other rock magnetic experiments (e.g., anisotropy of
36
37 899 anhysteretic remanent magnetism (AARM) can be conducted to further isolate the relative
38
39 900 importance of different paramagnetic and ferromagnetic phases (e.g., McCabe *et al.*, 1985; Richter
40
41 901 & van der Pluijm, 1994; Kelso *et al.*, 2002).

42 43 902 44 903 **Observations**

45
46 904 Having established the magnetic mineralogy, AMS fabrics can be interpreted. Even in weakly
47
48 905 anisotropic igneous rocks (i.e. visually isotropic), particularly sheet intrusions, it is now accepted
49
50 906 that the magnetic lineation and foliation can provide information on magma migration (e.g., flow
51
52 907 direction) or regional and local strain (e.g., Hrouda, 1982; Knight & Walker, 1988; Rochette *et al.*,

1
2
3
4
5
6 908 1992; Bouchez, 1997; Tauxe *et al.*, 1998; Callot *et al.*, 2001; Féménias *et al.*, 2004; Magee *et al.*,
7
8 909 2012a). For example, comparisons to other indicators of magma flow (e.g., intrusive steps and
9
10 910 visible mineral alignments) in sheet intrusions have shown that magnetic lineations commonly
11
12 911 parallel the magma flow (e.g., Knight & Walker, 1988; Cruden & Launeau, 1994; Callot *et al.*,
13
14 912 2001; Magee *et al.*, 2012a), whilst imbrication of elongate crystals induced by simple shear at
15
16 913 intrusion margins define the sense of magma flow (Fig. ~~12B~~12b) (e.g., Knight & Walker, 1988;
17
18 914 Hargraves *et al.*, 1991; Stephenson, 1994; Geoffroy *et al.*, 2002; Féménias *et al.*, 2004).
19
20 915 Alternatively, contact-parallel magnetic fabrics generated during the formation and inflation of
21
22 916 magma lobes can be used to determine flow and emplacement dynamics, even if other evidence for
23
24 917 the presence of magma lobes is lacking (e.g., Fig. ~~12C~~12c) (Cruden *et al.*, 1999; Stevenson *et al.*,
25
26 918 2007a; Magee *et al.*, 2012b). Identifying changes in fabric orientation within or between individual
27
28 919 sheet intrusions is also important because these variations suggest that deformation, imparted by
29
30 920 either the emplacement of adjacent magma bodies or tectonic processes, did not significantly
31
32 921 modify magma emplacement fabrics (e.g., Clemente *et al.*, 2007).

33
34 922 Post solidification textural modification and the possibility of overlap in tectonic and
35
36 923 magmatic strain fields during protracted emplacement is a particular complication when studying
37
38 924 granitoid and gabbroic plutons (e.g., Mamtani *et al.*, 2013; O'Driscoll *et al.*, 2015; Cheadle *et al.*,
39
40 925 2017). In fact, most early studies of granitoid emplacement using AMS, in conjunction with many
41
42 926 other structural analysis tools, concluded that tectonic strain was the main source of subtle fabrics
43
44 927 (e.g., Brun *et al.*, 1990; Bouchez, 1997; de Saint-Blanquat & Tikoff 1997; Neves *et al.*, 2003;
45
46 928 Mamtani *et al.*, 2005). Although primary magma flow fabrics in granitic and gabbroic plutons may
47
48 929 thus be overprinted, the magnetic fabrics characterised by AMS can still provide fundamental
49
50 930 insights into emplacement mechanics (e.g., Stevenson *et al.*, 2007a; Petronis *et al.*, 2012) and
51
52 931 magma/mush evolution (e.g., formation of layering; O'Driscoll *et al.*, 2015).

53 54 55 56 57 58 59 60 52933 ***Implications and integration***

1
2
3
4
5
6 934 Overall, AMS has provided vital magma flow and evolution information that has helped to
7
8 935 understand mafic and silicic magma plumbing systems (e.g., Knight & Walker, 1988; Ernst &
9
10 936 Baragar, 1992; Glen *et al.*, 1997; Aubourg *et al.*, 2008; Petronis *et al.*, 2013; Petronis *et al.*, 2015).
11 937 Critical insights emanating from these AMS studies have revealed that: (i) flow trajectories
12
13 938 predicted by classic emplacement models (e.g., for ring dykes and cone sheets) are not always
14
15 939 consistent with measured AMS fabrics and supporting data, which thereby call into question the
16
17 940 application of such models (e.g., Stevenson *et al.*, 2007b; Magee *et al.*, 2012a); (ii) lateral magma
18
19 941 flow is recorded in many shallow, planar intrusions associated with volcanic magma plumbing
20
21 942 systems (e.g., Ernst & Baragar, 1992; Cruden & Laneau, 1994; Cruden *et al.*, 1999; Herrero-
22 943 Bervera *et al.*, 2001; Magee *et al.*, 2012a; Petronis *et al.*, 2013; Petronis *et al.*, 2015); and (iii)
23
24 944 plutons, particularly those with a granitic composition, commonly consist of incrementally
25
26 945 emplaced magma pulses that often develop lobate geometries (e.g., Fig. 12C12c) (e.g., Stevenson *et*
27
28 946 *al.*, 2007a). Analysing AMS fabrics from layered mafic-ultramafic intrusions can also provide
29
30 947 evidence for magma reservoir processes, including crystal settling, or post-cumulus modification of
31
32 948 crystal mushes (O'Driscoll *et al.*, 2008; O'Driscoll *et al.*, 2015). Importantly, AMS and related
33
34 949 analyses provide robust, testable, and repeatable methods to constrain subtle shape and
35 950 crystallographic orientations of crystals in igneous rocks. Rock magnetic instrumentation
36
37 951 technology continues to advance with better automation of measurement protocols, sensitivity of
38
39 952 measurements, and a greater ability to unravel contributors to the AMS signal. The direction and
40
41 953 scope of these developments are improving the holistic integration of AMS with other structural,
42
43 954 microstructural, geophysical, petrological and geochemical techniques, promising to advance our
44
45 955 understanding of magmatism and crustal evolution.

46 956 47 48 957 **3. Future advances** 49

50 958 Our understanding of magma plumbing system structure and evolution has been significantly
51
52 959 enhanced by the geophysical techniques described above. We have demonstrated that there is scope
53
54
55
56
57
58
59
60

1
2
3
4
5
6 960 for advancement within individual methodologies and through the integration of different
7
8 961 techniques, particularly involving the synthesis of geophysical, petrological, and geochemical data.

9
10 962 In this section, we ~~look forward and briefly~~ discuss two new, ~~upcoming~~ techniques that will
11 963 potentially revolutionize our understanding of magma plumbing systems: ~~(i) full-waveform~~
12
13 964 ~~inversion (FWI); and (ii) the use of unmanned aerial vehicles (UAVs) in mapping exposed~~
14
15 965 ~~intrusions~~. We also briefly discuss how integration of geophysical data with numerical modelling
16
17 966 can enhance our knowledge of reservoir construction and evolution.

18 19 967 20 21 968 **3.1. Full-Waveform Inversion**

22 969 *Technique*

23
24 970 We have demonstrated that seismic reflection data can provide unique insight into the 3D structure
25
26 971 of magma plumbing systems (e.g., see review by Magee *et al.*, 2016). In addition to using seismic
27
28 972 reflection data to image the subsurface, we can also invert the measured travel-times of reflected
29
30 973 acoustic energy to model subsurface P-wave velocities. Full-waveform inversion (FWI) is a rapidly
31
32 974 developing technology using active source seismic data to generate models that reproduce both the
33 975 travel-times and full waveform of the arriving wavefield, thereby matching observed seismic data
34
35 976 (Tarantola, 1984). Because FWI considers the full wavefield, as opposed to conventional techniques
36
37 977 that only model travel-times, it is a technique capable of recovering high-resolution models of
38
39 978 subsurface P-wave velocities and other physical properties (Warner *et al.*, 2013; Routh *et al.*, 2017).
40
41 979 The FWI technique begins with a best-guess starting velocity model for the subsurface geology,
42
43 980 which is then iteratively updated using a local linearized inversion until the observed seismic data is
44 981 matched (Virieux & Operto, 2009). FWI is much more computationally expensive than travel-time
45
46 982 tomography, as a full-physics implementation of the wave equation is required to generate the
47
48 983 predicted seismic data at all energy source and receiver locations for each iteration (Routh *et al.*,
49
50 984 2017). FWI, however, has the advantage of being able to resolve much finer-scale structure than
51
52 985 conventional techniques.

Observations

To date, 3D FWI has principally been applied within the petroleum sector to obtain high-resolution velocity models that can be used to improve depth-migrated (i.e. travel-time is converted to depth in metres) reflection images of petroleum reservoirs and their overburden (Sirgue *et al.*, 2010; Vigh *et al.*, 2010; Warner *et al.*, 2013; Kapoor *et al.*, 2013; Routh *et al.*, 2017). FWI can also produce interpretable, quantitative models of physical properties of rocks in the subsurface that can be related directly to compaction, permeability, and overpressure as measured in subsurface boreholes (Lazaratos *et al.*, 2011; Mancini *et al.*, 2015). Of relevance here is that mafic intrusions, which appear as high-amplitude reflections in seismic reflection data (e.g., Figs 10 and 11a), are recovered as high-velocity features in FWI velocity models (e.g., Fig. 13) (Mancini *et al.*, 2015; Kalincheva *et al.*, 2017). For example, successful application of 3D FWI to a marine ocean bottom seismometer dataset acquired across the Endeavour segment of the Juan de Fuca Ridge led to generation of a velocity model that had a resolution up to four times greater than travel-time tomography (Morgan *et al.*, 2016). Within this new, high-resolution velocity model, several velocity anomalies were identified and interpreted to indicate localized magma recharge of the axial reservoir, induced seismogenic cracking, and increased permeability (Arnoux *et al.*, 2017).

Implications and integration

Active magma plumbing systems comprise a complex network of interconnected conduits and reservoirs with variable geometries and sizes, which likely contain magmatic vapour-rich, liquid-rich, and mush-zones (Christopher *et al.*, 2015). These intrusions will all be associated with reduced P-wave velocities, which could be resolved in high-resolution, 3D FWI datasets as supported by successes in the fine-scale imaging of: (i) low-velocity gas clouds (Warner *et al.*, 2013); (ii) axial reservoirs at an oceanic spreading centre (Arnoux *et al.*, 2017); (iii) relatively narrow, low-velocity fault zones within an antiform (Morgan *et al.*, 2013); and (iv) a subduction zone using 2D FWI

1
2
3
4
5
6 1012 (Kamei *et al.*, 2012). A suite of synthetic tests ~~have~~ been performed to investigate whether 3D FWI
7
8 1013 could be applied to better understand magma plumbing systems (Morgan *et al.*, 2013). These tests
9
10 1014 indicate that it is possible to recover high-resolution models of P-wave velocity beneath volcanoes,
11
12 1015 which can then be used to better determine where magma/mush is stored beneath the surface. In
13
14 1016 particular, these synthetic tests suggest that FWI could be used to: (i) distinguish between
15
16 1017 continuous zones of mush and individual magma reservoirs; (ii) image sills and conduits of magma
17
18 1018 and/or fluids that are a few 10s metres across (e.g., Fig. 13); and (iii) image the deeper (lower-
19
20 1019 crustal) part of the magma system. We therefore consider that 3D FWI affords an unprecedented
21
22 1020 opportunity to obtain high-resolution images of actual magma plumbing systems beneath active
23
24 1021 volcanoes. To this end, the ongoing PROTEUS (Plumbing Reservoirs Of The Earth Under
25
26 1022 Santorini) experiment was specifically designed to use 3D FWI to investigate the Santorini magma
27
28 1023 plumbing system (Hooft *et al.*, 2017).

3.2. Unmanned Aerial Vehicle photogrammetry

Technique

31
32 1026
33 1027 Despite major advances in satellite-based remote sensing systems and aeromagnetic surveys, very
34
35 1028 high-resolution (i.e., mm–cm scale ground sampling distance) imagery of dykes and other igneous
36
37 1029 intrusions has been limited to low altitude aerial photography. This in turn has created a critical
38
39 1030 scale gap in intrusion studies, which range from <1 mm at thin section scale to the metres to 100's
40
41 1031 of metres scale provided by outcrop analysis, conventional remote sensing, and geophysical data.
42
43 1032 Fortunately, the emerging capability of unmanned aerial vehicle (UAV) photogrammetry fills this
44
45 1033 gap (e.g., Eisenbeiss, 2009; Westoby *et al.*, 2012; Bemis *et al.*, 2015; Eide *et al.*, 2017b). It is also
46
47 1034 noteworthy that several studies have demonstrated that digital photogrammetry can deliver high
48
49 1035 quality datasets with accuracies similar to more established laser scanning techniques (e.g., Leberl
50
51 1036 *et al.*, 2010; Hodgetts, 2013; Thiele *et al.*, 2015).

1
2
3
4
5
6 1037 The basic setup required to carry out UAV (or drone) photogrammetry is commercially
7
8 1038 available and relatively inexpensive, comprising a fixed wing or rotary wing UAV, a digital camera,
9
10 1039 and access to a suitable digital photogrammetry software package (e.g., Agisoft Photoscan Pro,
11 1040 Pix4Dmapper Pro, VisualSFM). UAV photogrammetry combines a simple and cost-effective
12
13 1041 method to acquire geospatially referenced, overlapping digital aerial images, from which structure-
14
15 1042 from-motion algorithms can generate spatial 3D datasets (Bemis *et al.*, 2014; Vollgger & Cruden,
16
17 1043 2016). Such an approach can be used for high spatial resolution mapping of all types of well-
18
19 1044 exposed igneous intrusions. The resulting data greatly enhance the effectiveness of traditional field
20
21 1045 mapping, particularly the characterisation of contact relationships and internal and external structure
22
23 1046 (e.g., fractures, fabrics, and phase distributions) of intrusive rocks, complementing AMS and
24 1047 petrological analyses.
25

26 1048

27

28 1049 **Observations**

29
30 1050 ~~Here we describe~~A-a photogrammetric workflow was applied to examine a swarm of 5 cm to 1 m
31
32 1051 wide Palaeogene dolerite and dacite dykes exposed on coastal outcrops at Bingie Bingie Point, SE
33
34 1052 Australia (Fig. 14). The orthophotograph of the entire wave-cut platform shows the distribution of
35
36 1053 the Palaeogene dolerite and dacite dykes and their Devonian host rock lithologies, including a
37 1054 prominent moderately NE-dipping aplite dyke (Fig. [14A14a](#)). Linear ENE-WSW linear terrain
38
39 1055 features pick out the traces of dyke-parallel joints (Fig. [14A14a](#)). The Palaeogene dykes trend 063°
40
41 1056 parallel to a major set of joints in the country rock that likely formed contemporaneously with syn-
42
43 1057 dyking extension (Fig. [14B14b](#)). Subsidiary joint sets trend NNW-SSE, sub-perpendicular to the
44
45 1058 Palaeogene dykes, N-S and E-W (Fig. [14B14b](#)). The Palaeogene dykes display considerable
46
47 1059 structural complexity such as bridge structures, intrusive steps and apophyses (Fig. [14C14c](#)). Where
48
49 1060 present, the steps mostly occur where dykes cross country rock contacts (e.g., the aplite-tonalite
50 1061 contact in the NE; Fig. [14C14c](#)).
51
52 1062

Implications and integration

Data such as the orthophotograph collected at Bingie Bingie Point indicate that high-resolution structural and lithological mapping and measurement can be carried out much more rapidly than by traditional survey methods (e.g., plane table or grid mapping). However, the use of conventional RGB cameras restricts the resulting image data to reflected visible light. Future applications will include the deployment of multispectral and hyperspectral sensors (infrared to short wave infrared to thermal infrared) as well as potential field geophysical or geodetic instruments (e.g., Sparks, 2012). A further challenge for UAV applications in many countries concerns the regulatory framework around the use of drones for research. The global trend is moving to require non-recreational UAV operators to have remotely piloted aircraft licences and for the associated organisation to be certified for UAV operations. Innovations in sensor types and design, attachment of geophysical instruments, machine learning, and integration with complementary techniques such as AMS will open up new avenues for UAV applications in the study of magma plumbing systems.

3.4. Numerical modelling of magma reservoir processes constrained by geophysical data

Geophysical imaging of both active and ancient magma plumbing systems is delivering new insights into the 3D geometry of reservoirs, the timing and rates of melt and magma transport, the pathways followed by magmas as they ascend through the crust, and typical stored melt fractions in mushes. These data can be used to constrain and calibrate numerical models of reservoir processes. Numerical models are used ubiquitously to understand and predict the behaviour of other subsurface crustal reservoirs, such as hydrocarbon reservoirs, groundwater resources, and targets for geological CO₂ storage (e.g., Chen *et al.*, 2003; Class *et al.*, 2009; Dean & Chen, 2011). However, there has been relatively little focus to date on developing numerical models for magma/mush reservoirs. Yet such models can integrate across different data sources and types, provide quantitative estimates of rates, volumes and timescales, and provide a framework for data interpretation. For example, numerical modelling of heat transfer within the plumbing system at

1
2
3
4
5
6 1089 Okmok Volcano in Alaska, which was informed by analytical models of geodetic data and
7
8 1090 estimated magma compositions of erupted material, allowed estimation of the role magma injection,
9
10 1091 crystallisation, and degassing processes had on volume changes over time (Caricchi *et al.*, 2014).
11
12 1092 Numerical thermal modelling has also helped interpret seismic data from the Soufrière Hills
13
14 1093 Volcano, Montserrat, suggesting higher melt fraction in the underlying magma reservoir than was
15
16 1094 inferred from seismic data alone (Paulatto *et al.*, 2012). More recent numerical models focus on
17
18 1095 crystal mushes, evaluating melt transport and reaction at low melt fractions, and these show that
19
20 1096 temperature and melt fraction in mushes can be decoupled; i.e. maximum temperature occurs close
21
22 1097 to the centre of the reservoir but maximum melt fraction occurs close to the top (Solano *et al.*,
23
24 1098 2014). This decoupling impacts how seismic velocities and electrical conductivities will be
25
26 1099 modified within the mush (Solano *et al.*, 2014). Other numerical models show the important role
27
28 1100 played by exsolution, crystallisation, and the viscoelastic response of the crust in driving magma
29
30 1101 mobilisation in and eruption from shallow reservoirs (e.g., Degruyter & Huber, 2014; Parmigiani *et*
31
32 1102 *al.*, 2016), as well as providing insights into the mixing mechanisms of melt and crystals in mushes
33
34 1103 (Bergantz *et al.*, 2015). However, most models to date have a lower dimensionality (zero dimension
35
36 1104 box models, or one/two dimensions) and capture only a small subset of the key physical and
37
38 1105 chemical processes that are likely to occur in crustal magma reservoirs or crystal mushes.
39
40 1106 Moreover, few studies have integrated modelling with geophysical data (cf. Gutierrez *et al.*, 2013).
41
42 1107 This is in marked contrast to the 3D modelling routinely undertaken of other crustal reservoirs (e.g.,
43
44 1108 hydrocarbon reservoirs), which is commonly integrated with and delimited by geophysical data.
45
46 1109 There is thus significant scope for improved, and integrated, numerical modelling of crustal magma
47
48 1110 reservoirs.

48 1112 **4. Conclusions**

49
50 1113 Determining the structure of magma plumbing systems is critical to understanding where melt and
51
52 1114 magma is stored in the crust, which can influence the location of volcanic eruptions and economic

1
2
3
4
5
6
7
8
9
10
11
12
13
14
15
16
17
18
19
20
21
22
23
24
25
26
27
28
29
30
31
32
33
34
35
36
37
38
39
40
41
42
43
44
45
46
47
48
49
50
51
52
53
54
55
56
57
58
59
60

ore deposits, providing an important framework for interpreting the physical and chemical evolution of magma from petrological and geochemical datasets. Geophysical techniques have revealed unique insights into the architecture of active and ancient magma plumbing systems, which when integrated with traditional structural, petrological and geochemical results has yielded exciting advances in our understanding of magmatic processes. However, divisions between communities applying these methodologies still exist, contributing to diverging views on the nature of magma plumbing systems. To help promote collaboration, we [have reviewed](#) a range of geophysical techniques and [discussed](#) how they could be integrated with structural, petrological and geochemical datasets to answer outstanding questions in the volcanological community. In particular, we demonstrate how a range geophysical techniques can be applied to track melt migration in near real-time, map entire intrusion networks in 3D, examine magma emplacement mechanics, and understand the evolution of crystal mushes. For example, Interferometric Synthetic Aperture Radar (InSAR) allows measurement of the development of active magmatic systems by successive intrusion, the vertical and lateral movements of magma, and the relationship between magma plumbing system dynamics and eruption. Seismicity beneath volcanoes can, when the magma interacts dynamically with the host rock, illuminate in high-resolution the time and spatial scales of the motion of magma and hydrothermal fluids. Seismic imaging of magma plumbing systems allows the spatial distribution of melt and magma to be determined whilst the inclusion of anisotropy within seismic techniques even allows sub-seismic wavelength features to be identified. Gravimetry can characterise the distribution and redistribution of mass (e.g., magma) in the subsurface over high spatial and temporal resolutions, helping to reveal the structure and composition of magma plumbing systems and the source(s) of volcano deformation. Electromagnetic methods, particularly magnetotellurics, can identify fluids within magmatic systems (e.g., melt, magma, and hydrothermal fluids). Seismic reflection data provide unprecedented 3D images of ancient magma plumbing systems and has revealed that laterally extensive, interconnected networks of sills and inclined sheets can play a pivotal role in transporting

1
2
3
4
5
6 magma through the crust to eruption sites potentially located >100 km away from the melt source.
7
8 Rock magnetics can provide fabric data pertaining to magma flow, deformation or crystallisation.
9
10 All these methodologies discussed have provided unique insights into the structure of igneous
11 intrusions and, through integration with petrological and geochemical datasets, are beginning to
12
13 help unravel the entire evolution of magma plumbing systems. In addition to the ongoing
14
15 application and advancement of these geophysical techniques, emerging methodologies look set to
16
17 radically improve our understanding of magma plumbing systems. For example, full-waveform
18
19 inversion can image and characterise physical properties across plumbing systems at an
20
21 unprecedented resolution, whereas unmanned aerial vehicle photogrammetry provides a tool for
22
23 high spatial resolution of outcrop scale intrusions that bridges the scale gap between seismic
24
25 reflection data and traditional mapping of magma plumbing systems. The geophysical techniques
26
27 discussed also provide critical constraints on input parameters for numerical modelling. Overall, we
28
29 consider that the future of magma plumbing system studies will benefit greatly from the synthesis
30
31 of geophysics and more traditional petrological and geochemical approaches.

32 33 34 **5. Acknowledgements**

35
36 We would like to thank Marian Holness for inviting us to put together this review article and for
37
38 editorial handling. We are very grateful to Juliet Biggs, Martyn Unsworth, John Bartley, and
39
40 Magnús Gudmundsson for their extensive and constructive reviews. CM is funded by an Imperial
41
42 College Research Fellowship at Imperial College London. SKE is funded by an Early Career
43
44 Fellowship from the Leverhulme Trust. KAW is funded by grant NE/L013932/1.

45 46 47 **6. References**

48
49 Abdelmalak, M. M., Andersen, T. B., Planke, S., Faleide, J. I., Corfu, F., Tegner, C., Shephard, G.
50
51 E., Zastrozhnov, D., Myklebust, R. (2015). The ocean-continent transition in the mid-Norwegian

52
53
54
55
56
57
58
59
60

1
2
3
4
5
6
7
8
9
10
11
12
13
14
15
16
17
18
19
20
21
22
23
24
25
26
27
28
29
30
31
32
33
34
35
36
37
38
39
40
41
42
43
44
45
46
47
48
49
50
51
52
53
54
55
56
57
58
59
60

margin: Insight from seismic data and an onshore Caledonian field analogue. *Geology* **43**, 1011-1014.

Aizawa, K., Kandam, W., Ogawa, Y., Iguchi, M., Yokoo, A., Yakiwara, H., Sugano, T. (2011). Temporal changes in electrical resistivity at Sakurajima volcano from continuous magnetotelluric observations. *Journal of Volcanology and Geothermal Research* **199**, 165-175.

Annen, C. (2011). Implications of incremental emplacement of magma bodies for magma differentiation, thermal aureole dimensions and plutonism–volcanism relationships. *Tectonophysics* **500**, 3-10.

Annen, C., Blundy, J. D., Sparks, R. S. J. (2006). The genesis of intermediate and silicic magmas in deep crustal hot zones. *Journal of Petrology* **47**, 505-539.

Annen, C., Blundy, J. D., Leuthold, J., Sparks, R. S. J. (2015). Construction and evolution of igneous bodies: Towards an integrated perspective of crustal magmatism. *Lithos* **230**, 206-221.

Arnoux G. M., Toomey, D., Hooft, E., Wilcock, W., Morgan, J., Warner, M., VanderBeek, B. (2017). Seismic evidence that black smoker heat flux is rate-limited by crustal permeability. *Geophysical Research Letters* **44**, 1687-1695.

Aubourg, C., Tshoso, G., le Gall, B., Bertrand, H., Tiercelin, J. -J., Kampunzu, A. B., Dyment, J., Modisi, M. (2008). Magma flow revealed by magnetic fabric in the Okavango giant dyke swarm, Karoo igneous province, northern Botswana. *Journal of Volcanology and Geothermal Research* **170**, 247-261.

Baba, K., Chave, A. D., Evans, R. L., Hirth, G., Mackie, R. L. (2006). Mantle dynamics beneath the East Pacific Rise at 17°S: Insights from the Mantle Electromagnetic and Tomography (MELT) experiment. *Journal of Geophysical Research* **111**, B02101.

Bailey, R. C. (1970). Inversion of the geomagnetic induction problem. *Proceedings of the Royal Society* **315**, 185-194.

- 1
2
3
4
5
6 1190 Bagnardi, M., Amelung, F., Poland, M. P. (2013). A new model for the growth of basaltic shields
7
8 1191 based on deformation of Fernandina volcano, Galápagos Islands. *Earth and Planetary Science*
9
10 1192 *Letters* **377**, 358-366.
- 11 1193 Balsley, J. R., & Buddington, A. F. (1960). Magnetic susceptibility anisotropy and fabric of some
12
13 1194 Adirondack granites and orthogneisses. *American Journal of Science* **A258**, 6-20.
- 14
15 1195 Bannister, S., Reyners, M., Stuart, G. & Savage, M. (2007). Imaging the Hikurangi subduction
16
17 1196 zone, New Zealand, using teleseismic receiver functions: crustal fluids above the forearc mantle
18
19 1197 wedge. *Geophysical Journal International* **169**, 602-616.
- 20
21 1198 Battaglia, M., Roberts, C. & Segall, P. (1999). Magma intrusion beneath Long Valley caldera
22
23 1199 confirmed by temporal changes in gravity. *Science* **285**, 2119-2122.
- 24 1200 Battaglia, M. & Segall, P. (2004). The Interpretation of Gravity Changes and Crustal Deformation
25
26 1201 in Active Volcanic Areas. *Pure and Applied Geophysics* **161**, 1453-1467.
- 27
28 1202 Battaglia, M., Troise, C., Obrizzo, F., Pingue, F. & De Natale, G. (2006). Evidence for fluid
29
30 1203 migration as the source of deformation at Campi Flegrei caldera (Italy). *Geophysical Research*
31
32 1204 *Letters* **33**, L01307.
- 33
34 1205 Bemis, S. P., Micklethwaite, S., Turner, D., James, M. R., Akciz, S., Thiele, S., Bangash, H. A.
35
36 1206 (2014). Ground-based and UAV-Based photogrammetry: A multi-scale, high-resolution mapping
37
38 1207 tool for structural geology and paleoseismology. *Journal of Structural Geology* **69**, 163-178.
- 39 1208 Bergantz, G. W., Schleicher, J. M., Burgisser, A. (2015) Open-system dynamics and mixing in
40
41 1209 magma mushes. *Nature Geoscience* **8**, 793-796.
- 42
43 1210 Berryman, J. G. (1980). Long-wavelength propagation in composite elastic media II. Ellipsoidal
44
45 1211 inclusions. *The Journal of the Acoustical Society of America* **68**, 1820-1831.
- 46 1212 Bersi, M., Saibi, H. & Chabou, M. C. (2016). Aerogravity and remote sensing observations of an
47
48 1213 iron deposit in Gara Djebilet, southwestern Algeria. *Journal of African Earth Sciences* **116**, 134-
49
50 1214 150.

51
52
53
54
55
56
57
58
59
60

1
2
3
4
5
6
7
8
9
10
11
12
13
14
15
16
17
18
19
20
21
22
23
24
25
26
27
28
29
30
31
32
33
34
35
36
37
38
39
40
41
42
43
44
45
46
47
48
49
50
51
52
53
54
55
56
57
58
59
60

- Biedermann, A. R., Pettke, T., Reusser, E., Hirt, A. M. (2014). Anisotropy of magnetic susceptibility in natural olivine single crystals. *Geochemistry, Geophysics, Geosystems* **15**, 3051–3065.
- Biggs, J., Anthony, E. Y. & Ebinger, C. J. (2009). Multiple inflation and deflation events at Kenyan volcanoes, East African Rift. *Geology* **37**, 979-982.
- Biggs, J., Bastow, I. D., Keir, D. & Lewi, E. (2011). Pulses of deformation reveal frequently recurring shallow magmatic activity beneath the Main Ethiopian Rift. *Geochemistry, Geophysics, Geosystems* **12**, Q0AB10.
- Biggs, J., Ebmeier, S. K., Aspinall, W. P., Lu, Z., Pritchard, M. E., Sparks, R. S. J., Mather, T. A. (2014). Global link between deformation and volcanic eruption quantified by satellite imagery. *Nature Communications* **5**, 3471.
- Biggs, J. & Pritchard, M. E. (2017). Global volcano monitoring: what does it mean when volcanoes deform?. *Elements* **13**, 17-22.
- Bonforte, A., Carbone, D., Greco, F. & Palano, M. (2007). Intrusive mechanism of the 2002 NE-rift eruption at Mt Etna (Italy) modelled using GPS and gravity data. *Geophysical Journal International* **169**, 339-347.
- Borradaile, G. J. & Henry, B. (1997). Tectonic applications of the magnetic susceptibility and its anisotropy. *Earth Science Reviews* **42**, 49-93.
- Bosworth, W., Stockli, D. F. & Helgeson, D. E. (2015). Integrated outcrop, 3D seismic, and geochronologic interpretation of Red Sea dike-related deformation in the Western Desert, Egypt—The role of the 23Ma Cairo “mini-plume”. *Journal of African Earth Sciences* **109**, 107-119.
- Bott, M. H. P. (1953). Negative gravity anomalies over acid "intrusions" and their relation to the structure of the Earth's crust. *Geological Magazine* **90**, 257-267.
- Bouchez, J. L. (1997). Granite is never isotropic: An introduction to AMS studies of granitic rocks. In: Bouchez, J. L., Hutton, D. H. W., Stephens, W. E. (eds) *Granite: From Segregation of Melt to Emplacement Fabrics* 8: pp. 95-112. Dordrecht: Kluwer Academic.

- 1
2
3
4
5
6 1241 Brown, A. R. (2004). *Interpretation of three-dimensional seismic data*. Oklahoma, USA: AAPG
7
8 1242 and SEG.
- 9
10 1243 Brun, J. P., Gapais, D., Cogne, J. P., Ledru, P. & Vigneresse, J. L. (1990). The Flamanville granite
11 1244 (northwest France): an unequivocal example of a syntectonically expanding pluton. *Geological*
12
13 1245 *Journal* **25**, 271-286.
- 14
15 1246 Bucher, W. H. (1944). Discussion in Romberg, F., and Barnes, V. E. Correlation of gravity
16
17 1247 observations with the geology of the Smoothingiron granite mass, Llano County, Texas. *Geophysics*
18
19 1248 **9**, 79-93.
- 20
21 1249 Callot, J. -P., Geoffroy, L., Aubourg, C., Pozzi, J., Mege, D. (2001). Magma flow directions of
22
23 1250 shallow dykes from the East Greenland volcanic margin inferred from magnetic fabric studies.
24
25 1251 *Tectonophysics* **335**, 313-329.
- 26 1252 Carbone, D., Poland, M. P., Patrick, M. R. & Orr, T. R. (2013). Continuous gravity measurements
27
28 1253 reveal a low-density lava lake at Kīlauea Volcano, Hawai‘i. *Earth and Planetary Science Letters*
29
30 1254 **376**, 178-185.
- 31
32 1255 Carbone, D., Poland, M. P., Diament, M. & Greco, F. (2017). The added value of time-variable
33
34 1256 microgravimetry to the understanding of how volcanoes work. *Earth-Science Reviews* **169**, 146-
35
36 1257 179.
- 37 1258 Caricchi, L., Biggs, J., Annen, C., Ebmeier, S. (2014) The influence of cooling, crystallisation and
38
39 1259 re-melting on the interpretation of geodetic signals in volcanic systems. *Earth and Planetary*
40
41 1260 *Science Letters* **388**, 166-174.
- 42
43 1261 Cartwright, J. & Hansen, D. M. (2006). Magma transport through the crust via interconnected sill
44
45 1262 complexes. *Geology* **34**, 929-932.
- 46 1263 Cartwright, J. & Huuse, M. (2005). 3D seismic technology: the geological ‘Hubble’. *Basin*
47
48 1264 *Research* **17**, 1-20.
- 49
50 1265 Cashman, K. V. & Sparks, R. S. J. (2013). How volcanoes work: A 25 year perspective. *Geological*
51
52 1266 *Society of America Bulletin* **125**, 664-690.
- 53
54
55
56
57
58
59
60

1
2
3
4
5
6
7
8
9
10
11
12
13
14
15
16
17
18
19
20
21
22
23
24
25
26
27
28
29
30
31
32
33
34
35
36
37
38
39
40
41
42
43
44
45
46
47
48
49
50
51
52
53
54
55
56
57
58
59
60

Cashman, K. V., Sparks, R. S. J. & Blundy, J. D. (2017). Vertically extensive and unstable magmatic systems: a unified view of igneous processes. *Science* **355**, p.eaag3055.

Chaussard, E. & Amelung, F. (2013) Depth of magma storage in volcanic arcs: testing the influence of regional parameters using a global data compilation. In EGU General Assembly Conference Abstracts (Vol. 15).

Cheadle, M. J., & Gee, J. S. (2017). Quantitative textural insights into the formation of gabbro in mafic intrusions. *Elements* **13**, 409-414.

Chen, Y., Durlofsky, L. J., Gerritsen, M., Wen, X. H. (2003). A coupled local–global upscaling approach for simulating flow in highly heterogeneous formations. *Advances in Water Resources* **26**, 1041-1060.

Chmielowski, J., Zandt, G. & Haberland, C. (1999). The central Andean Altiplano-Puna magma body. *Geophysical Research Letters* **26**, 783-786.

Chouet, B., Dawson, P., Martini, M. (2008). Shallow-conduit dynamics at Stromboli Volcano, Italy, imaged from waveform inversions. In: Lane, S. J., Gilbert, J. S. (Eds.), *Fluid Motions in Volcanic Conduits: A Source of Seismic and Acoustic Signals. Geological Society of London Special Publication* **307**, 57-84.

Christopher, T. E., Blundy, J. D., Cashman, K., Cole, P., Edmonds, M., Smith, P. J., Sparks, R. S. J. & Stinton, A. (2015). Crustal-scale degassing due to magma system destabilization and magma-gas decoupling at Soufrière Hills Volcano, Montserrat. *Geochemistry Geophysics Geosystems* **16**, 2797-2811.

Chouet, B. & Matoza, R. S. (2013). A Multi-decadal view of seismic methods for detecting precursors of magma movement and eruption. *Journal of Volcanology and Geothermal Research* **252**, 108-175.

Class, H., Ebigbo, A., Helmig, R., Dahle, H. K., Nordbotten, J. M., Celia, M. A., Audigane, P., Darcis, M., Ennis-King, J., Fan, Y., Flemisch, B. (2009). A benchmark study on problems related to CO₂ storage in geologic formations. *Computational Geosciences* **13**, 409-434.

- 1
2
3
4
5
6 1293 Clemente, C. S., Amorós, E. B. & Crespo, M. G. (2007). Dike intrusion under shear stress: effects
7
8 1294 on magnetic and vesicle fabrics in dikes from rift zones of Tenerife (Canary Islands). *Journal of*
9
10 1295 *Structural Geology* **29**, 1931-1942.
- 11 1296 Comeau, M. J., Unsworth, M. J., Ticona, F., Sunagua, M. (2015). Magnetotelluric images of
12
13 1297 magma distribution beneath Volcán Uturuncu, Bolivia: Implications for magma dynamics. *Geology*
14
15 1298 **43**, 243-246.
- 16
17 1299 Comeau, M. J., Unsworth, M. J., Cordell, D. (2016). New constraints on the magma distribution
18
19 1300 and composition beneath Volcán Uturuncu and the southern Bolivian Altiplano from
20
21 1301 magnetotelluric data. *Geosphere* **12**, 1391-1421.
- 22 1302 Constable, S. C., Parker, R. L., Constable, C. G. (1987). Occam's inversion: A practical algorithm
23
24 1303 for generating smooth models from electromagnetic sounding data. *Geophysics* **52**, 289-300.
25
- 26 1304 Cruden, A. R. & Launeau, P. (1994). Structure, magnetic fabric and emplacement of the Archean
27
28 1305 Lebel Stock, SW Abitibi greenstone belt. *Journal of Structural Geology* **16**, 677-691.
- 29
30 1306 Cruden, A. R., Tobisch, O. T., Launeau, P. (1999). Magnetic fabric evidence for conduit fed
31
32 1307 emplacement of a tabular granite: Dinkey Creek Pluton, central Sierra Nevada Batholith, California.
33
34 1308 *Journal of Geophysical Research* **104**, 10,511-10,531.
- 35 1309 Cruden, A. R. & Weinberg, R. F. (2018). Mechanisms of magma transport and storage in the lower
36
37 1310 and middle crust – magma segregation, ascent and emplacement. In: Burkhardt, S. (Ed). *Volcanic*
38
39 1311 *and Igneous Plumbing Systems*, Elsevier, Amsterdam, In Press.
- 40
41 1312 Currenti, G., Del Negro, C. & Ganci, G. (2007). Modelling of ground deformation and gravity
42
43 1313 fields using finite element method: an application to Etna volcano. *Geophysical Journal*
44
45 1314 *International* **169**, 775-786.
- 46 1315 Currenti, G., Napoli, R., Coco, A. & Privitera, E. (2017). Effects of hydrothermal unrest on stress
47
48 1316 and deformation: insights from numerical modeling and application to Vulcano Island (Italy).
49
50 1317 *Bulletin of Volcanology* **79**, 28.

51
52
53
54
55
56
57
58
59
60

- 1
2
3
4
5
6 1318 de Saint Blanquat, M. & Tikoff, B. (1997). Development of magmatic to solid-state fabrics during
7
8 1319 syntectonic emplacement of the Mono Creek Granite, Sierra Nevada Batholith. In *Granite: from*
9
10 1320 *segregation of melt to emplacement fabrics*, Springer Netherlands, 231-252.
- 11 1321 Dean, O. S. & Chen, Y. (2011). Recent progress on reservoir history matching: a review.
12
13 1322 *Computational Geosciences* **15**, 152-221.
- 14
15 1323 DeGruyter, W. & Huber, C. (2014). A model for eruption frequency of upper crustal silicic magma
16
17 1324 chambers. *Earth and Planetary Science Letters* **403**, 117-130.
- 18
19 1325 del Potro, R., Diez, M., Blundy, J., Gottsmann, J. & Camacho, A. (2013). Diapiric ascent of silicic
20
21 1326 magma beneath the Bolivian Altiplano. *Geophysical Research Letters* **40**, 2044-2048.
- 22 1327 Delph, J. R., Ward, K. M., Zandt, G., Ducea, M. N., Beck, S. L. (2017). Imaging a magma
23
24 1328 plumbing system from MASH zone to magma reservoir. *Earth and Planetary Science Letters* **457**,
25
26 1329 313-324.
- 27
28 1330 Desissa, M., Johnson, N. E., Whaler, K. A., Hautot, S., Fisseha, S., Dawes, G. (2013). A mantle
29
30 1331 magma reservoir beneath an incipient mid-ocean ridge in Afar, Ethiopia. *Nature Geoscience* **6**, 861-
31
32 1332 865.
- 33 1333 Di Maio, R., Mauriello, P., Patella, D., Petrillo, Z., Piscitelli, S., Siniscalchi, A. (1998). Electric and
34
35 1334 electromagnetic outline of the Mount Somma–Vesuvius structural setting. *Journal of Volcanology*
36
37 1335 *and Geothermal Research* **82**, 219-238.
- 38
39 1336 Dixon, T. H. (1991). An introduction to the Global Positioning System and some geological
40
41 1337 applications. *Reviews of Geophysics* **29**, 249-276.
- 42
43 1338 Drew, J., White, R. S., Tilmann, F., Tarasewicz, J. (2013) Coalescence microseismic mapping.
44
45 1339 *Geophysical Journal International* **195**, 1773-1785.
- 46 1340 Dugda, M. T., Nyblade, A. A., Julia, J., Langston, C. A., Ammon, C. J., Simiyu, S. (2005). Crustal
47
48 1341 structure in Ethiopia and Kenya from receiver function analysis: Implications for rift development
49
50 1342 in eastern Africa. *Journal of Geophysical Research* **110**, B01303.

- 1
2
3
4
5
6 1343 Dunlop, D. J. (2002). Theory and application of the Day plot (Mrs/Ms versus Hcr/Hc) 1.
7
8 1344 Theoretical curves and tests using titanomagnetite data. *Journal of Geophysical Research: Solid*
9
10 1345 *Earth* **107**(B3).
- 11 1346 Dunlop, D. J. & Özdemir, Ö. (2001). Rock magnetism: fundamentals and frontiers (Vol. 3).
12
13 1347 Cambridge university press.
- 14
15 1348 Dvorak, J. J. & Dzurisin, D. (1997). Volcano geodesy: The search for magma reservoirs and the
16
17 1349 formation of eruptive vents. *Reviews of Geophysics* **35**, 343-384.
- 18
19 1350 Dzurisin, D. (2006). Volcano deformation: new geodetic monitoring techniques. Springer Science
20
21 1351 & Business Media.
- 22 1352 Eaton, G. P., Christiansen, R. L., Iyer, H. M., Pitt, A. D., Mabey, D. R., Blank, H. R., Zietz, I. &
23
24 1353 Gettings, M. E. (1975). Magma Beneath Yellowstone National park. *Science* **188**, 787.
25
- 26 1354 Ebinger, C., Keir, D., Ayele, A., Calais, E., Wright, T. J., Belachew, M., Hammond, J. O. S.,
27
28 1355 Campbell, E., Buck, W. R. (2008). Capturing magma intrusion and faulting processes during
29
30 1356 continental rupture: seismicity of the Dabbahu (Afar) rift. *Geophysical Journal International* **174**,
31
32 1357 1138-1152.
- 33 1358 Ebinger, C. J., Keir, D., Bastow, I. D., Whaler, K., Hammond, J. O., Ayele, A., Miller, M. S.,
34
35 1359 Tiberi, C., Hautot, S. (2017). Crustal structure of active deformation zones in Africa: Implications
36
37 1360 for global crustal processes. *Tectonics*.
- 38
39 1361 Ebmeier, S. K., Elliott, J. R., Nocquet, J. M., Biggs, J., Mothes, P., Jarrín, P., Yépez, M., Aguaiza,
40
41 1362 S., Lundgren, P., Samsonov, S. V. (2016). Shallow earthquake inhibits unrest near Chiles–Cerro
42
43 1363 Negro volcanoes, Ecuador–Colombian border. *Earth and Planetary Science Letters* **450**, 283-291.
- 44 1364 Ebmeier, S. K., Andrews, B. J., Araya, M. C., Arnold, D. W. D., Biggs, J., Cooper, C. & 10 others.
45
46 1365 (2018). Synthesis of global satellite observations of magmatic and volcanic deformation:
47
48 1366 implications for volcano monitoring & the lateral extent of magmatic domains. *Journal of Applied*
49
50 1367 *Volcanology*, **7**, 2.

51
52
53
54
55
56
57
58
59
60

- 1
2
3
4
5
6 1368 Eide, C. H., Schofield, N., Lecomte, I., Buckley, S. J. and Howell, J. A. (2017a). Seismic
7
8 1369 interpretation of sill complexes in sedimentary basins: implications for the sub-sill imaging
9
10 1370 problem. *Journal of the Geological Society of London*, jgs2017-096.
- 11 1371 Eide, C. H., Schofield, N., Jerram, D. A., Howell, J. A. (2017b). Basin-scale architecture of deeply
12
13 1372 emplaced sill complexes: Jameson Land, East Greenland. *Journal of the Geological Society of*
14
15 1373 *London* **174**, 23-40.
- 16
17 1374 Eisenbeiss, H. (2009). UAV Photogrammetry. PhD thesis. ETH Zurich.
- 18
19 1375 Ernst, R. E. & Baragar, W. R. A. (1992). Evidence from magnetic fabric for the flow pattern of
20
21 1376 magma in the Mackenzie giant radiating dyke swarm. *Nature* **356**, 511.
- 22 1377 Féménias, O., Diot, H., Berza, T., Gauffriau, A., Demaiffe, D. (2004). Asymmetrical to symmetrical
23
24 1378 magnetic fabric of dikes: Paleo-flow orientations and Paleo-stresses recorded on feeder-bodies from
25
26 1379 the Motru Dike Swarm (Romania). *Journal of Structural Geology* **26**, 1401-1418.
- 27
28 1380 Ferguson, I. J. (2012). Instrumentation and field procedures, in *The Magnetotelluric Method:*
29
30 1381 *Theory and Practice*, ed. Chave, A. D. & Jones, A. G., Cambridge University Press.
- 31
32 1382 Field, L., Blundy, J. D., Brooker, R. A., Wright, T., Yirgu, G. (2012) Magma storage conditions
33
34 1383 beneath Dabbahu volcano (Ethiopia) constrained by petrology, seismicity and satellite geodesy.
35
36 1384 *Bulletin of Volcanology* **74**, 981-1004.
- 37 1385 Fournier, T. J., Pritchard, M. E., Riddick, S. N. (2010). Duration, magnitude, and frequency of
38
39 1386 subaerial volcano deformation events: New results from Latin America using InSAR and a global
40
41 1387 synthesis. *Geochemistry, Geophysics, Geosystems* **11**, Q01003.
- 42
43 1388 Gaillard, F. (2004). Laboratory measurements of electrical conductivity of hydrous and dry silicic
44
45 1389 melts under pressure. *Earth and Planetary Science Letters* **218**, 215-228.
- 46 1390 Galland, O. (2012). Experimental modelling of ground deformation associated with shallow magma
47
48 1391 intrusions. *Earth and Planetary Science Letters* **317**, 145-156.
- 49
50 1392 Gamble, T. D., Goubau, W. M., Clarke, J. (1979). Magnetotellurics with a remote magnetic
51
52 1393 reference. *Geophysics* **44**, 53-68.
- 53
54
55
56
57
58
59
60

- 1
2
3
4
5
6 1394 Garapic, G., Faul, U. H., Brisson, E. (2013). High-resolution imaging of the melt distribution in
7
8 1395 partially molten upper mantle rocks: evidence for wetted two-grain boundaries. *Geochemistry*
9
10 1396 *Geophysics Geosystems* **14**, 556-566.
- 11 1397 Geoffroy, L., Callot, J. P., Aubourg, C. & Moreira, M. (2002). Magnetic and plagioclase linear fabric
12
13 1398 discrepancy in dykes: a new way to define the flow vector using magnetic foliation. *Terra Nova* **14**,
14
15 1399 183-190.
- 16
17 1400 Gerst, A. & Savage, M. K. (2004). Seismic anisotropy beneath Ruapehu volcano: a possible eruption
18
19 1401 forecasting tool. *Science* **306**, 1543-1547.
- 20
21 1402 Glazner, A. F., Bartley, J. M. & Coleman, D. S. (2016). We need a new definition for "magma". *Eos*
22
23 1403 **97**.
- 24 1404 Glen, J. M., Renne, P. R., Milner, S. C., Coe, R. S. (1997). Magma flow inferred from anisotropy of
25
26 1405 magnetic susceptibility in the coastal Parana-Etendeka igneous province: Evidence for rifting before
27
28 1406 flood volcanism. *Geology* **25**, 1131-1134.
- 29
30 1407 Goes, S., Armitage, J., Harmon, N., Smith, H., Huisman, R. (2012). Low seismic velocities below
31
32 1408 mid-ocean ridges: Attenuation versus melt retention. *Journal of Geophysical Research* **117**, B12403.
- 33
34 1409 Gottsmann, J., Rymer, H. & Wooller, L. K. (2005). On the interpretation of gravity variations in the
35
36 1410 presence of active hydrothermal systems: Insights from the Nisyros Caldera, Greece. *Geophysical*
37
38 1411 *Research Letters* **32**, L23310.
- 39 1412 Gottsmann, J., Camacho, A. G., Tiampo, K. F. & Fernández, J. (2006). Spatiotemporal variations in
40
41 1413 vertical gravity gradients at the Campi Flegrei caldera (Italy): a case for source multiplicity during
42
43 1414 unrest?. *Geophysical Journal International* **167**, 1089-1096.
- 44 1415 Gottsmann, J., Carniel, R., Coppo, N., Wooller, L., Hautmann, S. & Rymer, H. (2007). Oscillations
45
46 1416 in hydrothermal systems as a source of periodic unrest at caldera volcanoes: Multiparameter insights
47
48 1417 from Nisyros, Greece. *Geophysical Research Letters* **34**, L07307.
- 49
50 1418 Gottsmann, J., Camacho, A. G., Marti, J., Wooller, L., Fernández, J., Garcia, A. & Rymer, H. (2008).
51
52 1419 Shallow structure beneath the Central Volcanic Complex of Tenerife from new gravity data:
53
54
55
56
57
58
59
60

- 1
2
3
4
5
6 1420 Implications for its evolution and recent reactivation. *Physics of the Earth and Planetary Interior* **68**
7
8 1421 212-230.
- 9
10 1422 Gottsmann, J., Blundy, J. D., Henderson, S., Pritchard, M. E. & Sparks, R. S. J. (2017).
11 1423 Thermomechanical Modeling of the Altiplano-Puna Deformation Anomaly: Multiparameter Insights
12
13 1424 into Magma Mush Reorganization. *Geosphere* **13**, 1042-1065.
- 14
15 1425 Graham, J. W. (1954). Magnetic anisotropy, an unexploited petrofabric element. *Geological Society*
16
17 1426 *of America Bulletin* **65**, 1257-1258.
- 18
19 1427 Gudmundsson, O., Brandsdottir, B., Menke, W. & Sigvaldason, G. E. (1994). The crustal magma
20
21 1428 chamber of the Katla volcano in south Iceland revealed by 2-D seismic undershooting. *Geophysical*
22
23 1429 *Journal International* **119**, 277-296.
- 24 1430 Guidarelli, M., Stuart, G., Hammond, J. O., Kendall, J. M., Ayele, A., Belachew, M. (2011).
25
26 1431 Surface wave tomography across Afar, Ethiopia: Crustal structure at a rift triple-junction zone.
27
28 1432 *Geophysical Research Letters* **38**, L24313.
- 29
30 1433 Guo, X., Zhang, L., Behrens, H., Ni, H. (2016). Probing the status of felsic magma reservoirs:
31
32 1434 Constraints from the P - T - H_2O dependences of electrical conductivity of rhyolitic melt. *Earth and*
33
34 1435 *Planetary Science Letters* **433**, 54-62.
- 35 1436 Gutierrez, F., Payacan, I., Gelman, S. E., Bachmann, O., Parada, M. A. (2013) Late-stage magma
36
37 1437 flow in a shallow felsic reservoir: Merging the anisotropy of magnetic susceptibility record with
38
39 1438 numerical simulations in La Gloria Pluton, central Chile. *Journal of Geophysical Research-Solid*
40
41 1439 *Earth* **118**, 1984-1998.
- 42
43 1440 Hamilton, M. P., Jones, A. G., Evans, R. L., Evans, S., Fourie, C. J. S., Garcia, X., Mountford, A,
44
45 1441 Spratt, J. E., SAMTEX MT Team. (2006). Electrical anisotropy of South African lithosphere
46
47 1442 compared with seismic anisotropy from shear-wave splitting analyses. *Physics of the Earth and*
48
49 1443 *Planetary Interiors* **158**, 226-239.
- 50 1444 Hamling, I. J., Wright, T. J., Calais, E., Bennati, L., Lewi, E. (2010). Stress transfer between
51
52 1445 thirteen successive dyke intrusions in Ethiopia. *Nature Geoscience* **3**(10), 713-717.
- 53
54
55
56
57
58
59
60

- 1
2
3
4
5
6 1446 Hamling, I. J., Hreinsdottir, S. & Fournier, N. (2015). The ups and downs of the TVZ: Geodetic
7
8 1447 observations of deformation around the Taupo Volcanic Zone, New Zealand. *Journal of*
9
10 1448 *Geophysical Research: Solid Earth* **120**, 4667-4679.
- 11 1449 Hammer, S. (1945). Estimating ore masses in gravity prospecting. *Geophysics* **10**, 50-62.
12
- 13 1450 Hammond, W. & Humphreys, E. (2000a). Upper mantle seismic wave velocity: Effects of realistic
14
15 1451 partial melt geometries. *Journal of Geophysical Research* **105**, 10975-10986.
16
- 17 1452 Hammond, W. & Humphreys, E. (2000b). Upper mantle seismic wave attenuation: Effects of
18
19 1453 realistic partial melt distribution, *Journal of Geophysical Research* **105**, 10987-10999.
20
- 21 1454 Hammond, J. O. S., Kendall, J., Stuart, G. W., Keir, D., Ebinger, C. J., Ayele, A., Belachew, M.
22
23 1455 (2011). The nature of the crust beneath the Afar triple junction: Evidence from receiver functions.
24
25 1456 *Geochemistry Geophysics Geosystems* **12**, Q12004.
- 26 1457 Hammond, J. O. S. (2014). Constraining melt storage geometries beneath the Afar Depression,
27
28 1458 Ethiopia from teleseismic receiver functions: The anisotropic H-κ stacking technique. *Geochemistry*
29
30 1459 *Geophysics Geosystems* **15**, 1316-1332.
- 31
32 1460 Hammond, J. O. S. & Kendall, J. (2016). Constraints on melt distribution from seismology: a case
33
34 1461 study in Ethiopia. In: Wright, T. J., Ayele, A., Ferguson, D. J., Kidane, T., Vye-Brown, C. (eds.)
35
36 1462 *Magmatic Rifting and Active Volcanism*. Geological Society, Special Publication, London **420**, 127-
37
38 1463 147.
- 39 1464 Hansen, D. M. & Cartwright, J. (2006). The three-dimensional geometry and growth of forced folds
40
41 1465 above saucer-shaped igneous sills. *Journal of Structural Geology* **28**, 1520-1535.
42
- 43 1466 Hargraves, R. B., Chan, C. Y., Johnson, D. (1991). Distribution anisotropy: the cause of AMS in
44
45 1467 igneous rocks? *Geophysical Research Letters* **18**, 2193-2196.
- 46 1468 Hargraves, R. B., Briden, J. C., Daniels, B. A. (1999). Palaeomagnetism and magnetic fabric in the
47
48 1469 Freetown Complex, Sierra Leone. *Geophysical Journal International* **136**, 705-713.
49
- 50 1470 Harmon, N., & Rychert, C. A. (2015). Seismic imaging of deep crustal melt sills beneath Costa Rica
51
52 1471 suggests a method for the formation of the Archean continental crust. *Earth and Planetary Science*
53
54
55
56
57
58
59
60

1
2
3
4
5
6
7
8
9
10
11
12
13
14
15
16
17
18
19
20
21
22
23
24
25
26
27
28
29
30
31
32
33
34
35
36
37
38
39
40
41
42
43
44
45
46
47
48
49
50
51
52
53
54
55
56
57
58
59
60

Letters **430**, 140-148.

Hashin, Z. & Shtrikman, S. (1962). A variational approach to the theory of the effective magnetic permeability of multiphase materials. *Journal of Applied Physics* **33**, 3125-3131.

Hawkesworth, C. J., Blake, S., Evans, P., Hughes, R., Macdonald, R., Thomas, L. E., Turner, S. P., Zellmer, G. (2000). Time scales of crystal fractionation in magma chambers—integrating physical, isotopic and geochemical perspectives. *Journal of Petrology* **41**, 991-1006.

Heinson, G., Constable, S., White, A. (2000). Episodic melt transport at mid-ocean ridges inferred from magnetotelluric sounding. *Geophysical Research Letters* **27**, 2317-2320.

Hemmings, B., Coco, A., Gottsmann, J., Whitaker, F. (2016). Investigating hydrological contributions to volcano monitoring signals. *Geophysical Journal International* **207**, 259-273.

Herrero-Bervera, E., Walker, G., Canon-Tapia, E., Garcia, M. (2001). Magnetic fabric and inferred flow direction of dikes, conesheets and sill swarms, Isle of Skye, Scotland. *Journal of Volcanology and Geothermal Research* **106**, 195-210.

Hickey, J., Gottsmann, J., Nakamichi, H., Iguchi, M. (2016). Thermomechanical controls on magma supply and volcanic deformation: application to Aira caldera, Japan. *Scientific Reports* **6**, 32691.

Hickey, J., Gottsmann, J., Mothes, P., Odbert, H., Prutkin, I., Vajda, P. (2017). The ups and downs of volcanic unrest: insights from integrated geodesy and numerical modelling. *Advances in Volcanology*, 1-17, Springer.

Hildreth, W. (2004). Volcanological perspectives on Long Valley, Mammoth Mountain, and Mono Craters: several contiguous but discrete systems. *Journal of Volcanology and Geothermal Research* **136**, 169-198.

Hodgetts, D. (2013). Laser scanning and digital outcrop geology in the petroleum industry: A review. *Marine and Petroleum Geology* **46**, 335-354.

Hooft, E. E. E., Morgan, J. V., Nomikou, P., Toomey, D. R., Papazachos, C. V., Warner, M., Heath, B., Christopoulou, M-E., Lampridou, D., Kementzetzidou, D. (2016). The PROTEUS Experiment:

- 1
2
3
4
5
6 1497 Active Source Seismic Imaging of the Crustal Magma Plumbing Structure of the Santorini Arc
7
8 1498 Volcano. *AGU Fall meeting*, Abstract# DI23B-2619.
- 9
10 1499 Holohan, E. P., Sudhaus, H., Walter, T. R., Schöpfer, M. P., Walsh, J. J. (2017). Effects of Host-
11 1500 rock Fracturing on Elastic-deformation Source Models of Volcano Deflation. *Scientific Reports* **7**,
12
13 1501 10970.
- 14
15 1502 Hrouda, F. (1982). Magnetic anisotropy of rocks and its application in geology and geophysics.
16
17 1503 *Geophysical Surveys* **5**, 37-82.
- 18
19 1504 Hrouda, F., Schulmann, K., Suppes, M., Ullemayer, K., de Wall, H., Weber, K. (1997). Quantitative
20
21 1505 relationship between low-field AMS and phyllosilicate fabric: a review. *Physics and Chemistry of*
22 1506 *the Earth* **22**, 153-156.
23
- 24 1507 Hübner, J., Whaler, K. A., Fisseha, S. (2018). The electrical structure of the Central Main Ethiopian
25
26 1508 Rift as imaged by Magnetotellurics - Implications for magma storage and pathways. *Journal of*
27
28 1509 *Geophysical Research*, in review.
- 29
30 1510 Hunt, T. & Bowyer, D. (2007). ReInjection and gravity changes at Rotokawa geothermal field, New
31
32 1511 Zealand. *Geothermics* **36**, 421-435.
- 33
34 1512 Husen, S., Taylor, R., Smith, R. B., Healy, H. (2004). Changes in geyser eruption behavior and
35 1513 remotely triggered seismicity in Yellowstone National Park produced by the 2002 M 7.9 Denali
36
37 1514 fault earthquake, Alaska. *Geology* **32**(6), 537-540.
38
- 39 1515 Ivanic, T., Zibra, I., Doublier, M., Wyche, S. (2013). Geological Interpretation of the Youanmi and
40
41 1516 Southern Carnarvon seismic lines 10GA-YU1, 10GA-YU2, 10GA-YU3, and 11GA-SC1. In:
42
43 1517 Wyche, S., Ivanic, T., Zibra, I. (eds.) *Youanmi and Southern Carnarvon seismic and*
44 1518 *magnetotelluric (MT) workshop 2013*. Geological Survey of Western Australia, Plate 3.
45
- 46 1519 Jachens, R. C. & Roberts, C. W. (1985). Temporal and areal gravity investigations at Long Valley
47
48 1520 Caldera, California. *Journal of Geophysical Research* **90**, 11210-11218.
49
50
51
52
53
54
55
56
57
58
59
60

1
2
3
4
5
6
7
8
9
10
11
12
13
14
15
16
17
18
19
20
21
22
23
24
25
26
27
28
29
30
31
32
33
34
35
36
37
38
39
40
41
42
43
44
45
46
47
48
49
50
51
52
53
54
55
56
57
58
59
60

Jackson, C. A.-L., Schofield, N., Golenkov, B. (2013). Geometry and controls on the development of igneous sill-related forced folds: A 2-D seismic reflection case study from offshore southern Australia. *Geological Society of America Bulletin* **125**, 1874-1890.

Jackson, I., Fitzgerald, J. D., Faul, U. H., Tan, B. H. (2002). Grain-size-sensitive seismic wave attenuation in polycrystalline olivine. *Journal of Geophysical Research* **107**, B12, 2156-2202.

Jaxybulatov, K., Shapiro, N. M., Koulakov, I., Mordret, A., Landes, M., Sens-Schonfelder, C. (2014). A large magmatic sill complex beneath the Toba caldera. *Science* **346**, 617-619.

Jay, J. A., Pritchard, M. E., West, M. E., Christensen, D. H., Haney, M., Minaya, E., Sunagua, M., McNutt, S. R., Zabala, M. (2012). Shallow seismicity, triggered seismicity, and ambient noise tomography at the long-dormant Uturuncu volcano, Bolivia. *Bulletin of Volcanology* **74**, 817-837.

Jay, J., Costa, F., Pritchard, M., Lara, L., Singer, B., Herrin, J. (2014). Locating magma reservoirs using InSAR and petrology before and during the 2011–2012 Cordón Caulle silicic eruption. *Earth and Planetary Science Letters* **395**, 254-266.

Johnson, J. H. & Poland, M. P. (2013). Seismic detection of increased degassing before Kīlauea's 2008 summit explosion. *Nature communications* **4**, 1668.

Johnson, N. E., Whaler, K. A., Hautot, S., Fisseha, S., Desissa, M. & Dawes, G. J. K. (2016). Magma imaged magnetotellurically beneath an active and an inactive magmatic segment in Afar, Ethiopia. *Geological Society, London, Special Publications* **420**, 105-125.

Jones, A. G. (2012). Distortion of magnetotelluric data: its identification and removal, in *The Magnetotelluric Method: Theory and Practice*, ed. Chave, A. D. & Jones, A. G., Cambridge University Press.

Jousset, P., Mori, H. & Okada, H. (2000). Possible magma intrusion revealed by temporal gravity, ground deformation and ground temperature observations at Mount Komagatake (Hokkaido) during the 1996-1998 crisis. *Geophysical Journal International* **143**, 557-574.

Kalinicheva, T., Warner, M., Ashley, J., Mancini, F. (2017). Two vs three-dimensional FWI in a 3D world. *SEG International Exhibition and 87th Annual Meeting*.

- 1
2
3
4
5
6 1547 Kamei, R., Jang, U. G., Lumley, D., Mouri, T., Nakatsukasa, M., Kato, A. & Takanashi, M. (2017).
7
8 1548 Time-lapse Full Waveform Inversion for Monitoring Near-surface Microbubble Injection. *79th*
9
10 1549 *Conference and Exhibition, EAGE, Extended Abstracts*.
- 11 1550 Kapoor, S., Vigh, D., Wiarda, E., Alwon, S. (2013). Full waveform inversion around the world. *75th*
12
13 1551 *Conference and Exhibition, EAGE, Extended Abstracts*.
- 14
15 1552 Karato, S. & Jung, H. (1998). Water, partial melting and the origin of the seismic low velocity and
16
17 1553 high attenuation zone in the upper mantle. *Earth and Planetary Science Letters* **157**, 193-207.
- 18
19 1554 Kavanagh, J. L., Burns, A. J., Hazim, S. H., Wood, E., Martin, S. A., Hignett, S. Dennis, D. J. 2018.
20
21 1555 Challenging dyke ascent models using novel laboratory experiments: Implications for reinterpreting
22
23 1556 evidence of magma ascent and volcanism. *Journal of Volcanology and Geothermal Research*.
- 24 1557 Keir, D., Hamling, I. J., Ayele, A., Calais, E., Ebinger, C. J., Wright, T. J., Jacques, E., Mohamed,
25
26 1558 K., Hammond, J. O. S., Belachew, M., Baker, E., Rowland, J. V., Lewi, E., Bennati, L. (2009).
27
28 1559 Evidence for focused magmatic accretion at segment centers from lateral dike injection captured
29
30 1560 beneath the Red Sea rift of Afar. *Geology* **37**, 59-62.
- 31
32 1561 Keir, D., Belachew, M., Ebinger, C. J., Kendall, J. -M., Hammond, J. O. S., Stuart, G. W., Ayele, A.,
33
34 1562 Rowland, J. R. (2011). Mapping the evolving strain field during continental breakup from crustal
35
36 1563 anisotropy in the Afar Depression. *Nature Communications* **2**, 285-7.
- 37 1564 Kelso, P. R., Tikoff, B., Jackson, M., Sun, W. (2002). A new method for the separation of
38
39 1565 paramagnetic and ferromagnetic susceptibility anisotropy using low field and high field methods.
40
41 1566 *Geophysical Journal International* **151**, 345-359.
- 42
43 1567 Kent, G. M., Singh, S. C., Harding, A. J., Sinha, M. C., Orcutt, J. A. (2000). Evidence from three-
44
45 1568 dimensional seismic reflectivity images for enhanced melt supply beneath mid-ocean-ridge
46
47 1569 discontinuities. *Nature* **406**, 614-618.
- 48 1570 Key, K., Constable, S., Liu, L., Pommier, A. (2013). Electrical image of passive upwelling beneath
49
50 1571 the northern East Pacific Rise. *Nature* **495**, 499-502.
- 51
52 1572 Khan, M. A. (1962). The anisotropy of magnetic susceptibility of some igneous and metamorphic
53
54
55
56
57
58
59
60

- 1
2
3
4
5
6 1573 rocks. *Journal of Geophysical Research* **67**, 2873-2885.
- 7
8 1574 Kim, D., Brown, L. D., Árnason, K., Ágústsson, K., Blanck, H. (2017). Magma reflection imaging in
9
10 1575 Krafla, Iceland, using microearthquake sources. *Journal of Geophysical Research Solid Earth* **122**,
11 1576 5228-5242.
- 12
13 1577 Kiser, E., Levander, A., Schmandt, B., Palomeras, I., Harder, S. H., Creager, K. C., Vidale, J. E.,
14
15 1578 Malone, S. D. (2014). Field report on the iMUSH active source seismic experiment. *AGU Fall*
16
17 1579 *Meeting Abstracts* **1**, 2.
- 18
19 1580 Knight, M. D. & Walker, G. P. (1988). Magma flow directions in dikes of the Koolau Complex,
20
21 1581 Oahu, determined from magnetic fabric studies. *Journal of Geophysical Research* **93**, 4301-4319.
- 22
23 1582 Koulakov, I., Gordeev, E. I., Dobretsov, N. L., Vernikovskiy, V. A., Senyukov, S., Jakovlev, A. &
24 1583 Jaxybulatov, K. (2013). Rapid changes in magma storage beneath the Klyuchevskoy group of
25
26 1584 volcanoes inferred from time-dependent seismic tomography. *Journal of Volcanology and*
27
28 1585 *Geothermal Research* **263**, 75-91.
- 29
30 1586 Laumonier, M., Gaillard, F., Sifre, D. (2015). The effect of pressure and water concentration on the
31
32 1587 electrical conductivity of dacitic melts: Implication for magnetotelluric imaging in subduction areas.
33
34 1588 *Chemical Geology* **418**, 66-76.
- 35 1589 Launeau, P. & Cruden, A. R. (1998). Magmatic fabric acquisition mechanisms in a syenite: Results
36
37 1590 of a combined anisotropy of magnetic susceptibility and image analysis study. *Journal of*
38
39 1591 *Geophysical Research* **103**, 5067-5089.
- 40
41 1592 Lazaratos, S., Chikichev, I., Wang, K. (2011). Improving the convergence rate of full wavefield
42
43 1593 inversion using spectral shaping. *81st Annual International Meeting, SEG, Expanded Abstracts*.
- 44 1594 Le Mével, H., Feigl, K. L., Córdova, L., DeMets, C. & Lundgren, P. (2015). Evolution of unrest at
45
46 1595 Laguna del Maule volcanic field (Chile) from InSAR and GPS measurements, 2003 to 2014.
47
48 1596 *Geophysical Research Letters* **42**, 6590-6598.
- 49
50
51
52
53
54
55
56
57
58
59
60

1
2
3
4
5
6
7
8
9
10
11
12
13
14
15
16
17
18
19
20
21
22
23
24
25
26
27
28
29
30
31
32
33
34
35
36
37
38
39
40
41
42
43
44
45
46
47
48
49
50
51
52
53
54
55
56
57
58
59
60

Leberl, F., Irschara, A., Pock, T., Meixner, P., Gruber, M., Scholz, S., Wiechert, A. (2010). Point

Clouds: Lidar versus 3D Vision. *Photogrammetric Engineering and Remote Sensing* **76**, 1123-

1134.

Lees, J. M. (2007). Seismic tomography of magmatic systems. *Journal of Volcanology and*

Geothermal Research **167**, 37-56.

Lu, Z. Dzurisin, D. (2014). InSAR Imaging of Aleutian Volcanoes. In *InSAR Imaging of Aleutian*

Volcanoes (pp. 87-345). Springer Berlin Heidelberg.

MacGregor, L. M., Constable, S., Sinha, M. C. (1998). The RAMESSES experiment—III.

Controlled-source electromagnetic sounding of the Reykjanes Ridge at 57° 45' N. *Geophysical*

Journal International **135**, 773-789.

Magee, C., Stevenson, C. T. E., O'Driscoll, B., Schofield, N., McDermott, K. (2012a). An

alternative emplacement model for the classic Ardnamurchan cone sheet swarm, NW Scotland,

involving lateral magma supply via regional dykes. *Journal of Structural Geology* **43**, 73-91.

Magee, C., Stevenson, C. T. E., O'Driscoll, B., Petronis, M. S. (2012b). Local and regional controls

on the lateral emplacement of the Ben Hiant Dolerite intrusion, Ardnamurchan (NW Scotland).

Journal of Structural Geology **39**, 66-82.

Magee, C., Hunt-Stewart, E., Jackson, C. A. L. (2013a). Volcano growth mechanisms and the role

of sub-volcanic intrusions: Insights from 2D seismic reflection data. *Earth and Planetary Science*

Letters **373**, 41-53.

Magee, C., Briggs, F., Jackson, C. A.-L. (2013b). Lithological controls on igneous intrusion-

induced ground deformation. *Journal of the Geological Society* **170**, 853-856.

Magee, C., Jackson, C. L., Schofield, N. (2014). Diachronous sub-volcanic intrusion along deep-

water margins: insights from the Irish Rockall Basin. *Basin Research* **26**, 85-105.

Magee, C., Maharaj, S. M., Wrona, T., Jackson, C. A.-L. (2015). Controls on the expression of

igneous intrusions in seismic reflection data. *Geosphere*, GES01150.01151.

1
2
3
4
5
6
7
8
9
10
11
12
13
14
15
16
17
18
19
20
21
22
23
24
25
26
27
28
29
30
31
32
33
34
35
36
37
38
39
40
41
42
43
44
45
46
47
48
49
50
51
52
53
54
55
56
57
58
59
60

Magee, C., Muirhead, J. D., Karvelas, A., Holford, S. P., Jackson, C. A., Bastow, I. D., Schofield, N., Stevenson, C. T., McLean, C., McCarthy, W. (2016). Lateral magma flow in mafic sill complexes. *Geosphere*, GES01256.01251.

Magee, C., Bastow, I. D., van Wyk de Vries, B., Jackson, C. A. L., Hetherington, R., Hagos, M. & Hoggett, M. (2017). Structure and dynamics of surface uplift induced by incremental sill emplacement. *Geology* **45**, 431-434.

Magee, C., Muirhead, J., Schofield, N., Walker, R., Galland, O., Holford, S., Spacapan, J., Jackson, C. A-L., McCarthy, W. (2017). Structural signatures of igneous sheet intrusion propagation. *EarthArXiv* doi:10.17605/OSF.IO/PDN42.

Malehmir, A., Durrheim, R., Bellefleur, G., Urosevic, M., Juhlin, C., White, D. J., Milkereit, B., Campbell, G. (2012). Seismic methods in mineral exploration and mine planning: A general overview of past and present case histories and a look into the future. *Geophysics* **77**, WC173-WC190.

Mamtani, M. A., Pal, T. & Greiling, R. O. (2013). Kinematic analysis using AMS data from a deformed granitoid. *Journal of Structural Geology* **50**, 119-132.

Mancini, F., Moss, J., Prindle, K., Ridsdill-Smith, T. (2015). Where can full waveform inversion have the biggest impact in the exploration and production cycle? *77th International Conference and Exhibition, EAGE, Extended Abstracts*.

Manzella, A., Volpi, G., Zaja, A., Meju, M. (2004). Combined TEM-MT investigation of shallow-depth resistivity structure of Mt Somma-Vesuvius. *Journal of Volcanology and Geothermal Research* **131**, 19-32.

Marjanovic, M., Carbotte, S. M., Carton, H., Nedimovic, M. R., Mutter, J. C., Canales, J. P. (2014). A multi-sill magma plumbing system beneath the axis of the East Pacific Rise. *Nature Geoscience* **7**, 825-829.

Mark, N. J., Schofield, N., Pugliese, S., Watson, D., Holford, S., Muirhead, D., Brown, R., Healy, D. (2017). Igneous intrusions in the Faroe Shetland basin and their implications for hydrocarbon

- 1
2
3
4
5
6 1648 exploration; new insights from well and seismic data. *Marine and Petroleum Geology*
7
8 1649 Masterlark, T. (2007). Magma intrusion and deformation predictions: Sensitivities to the Mogi
9
10 1650 assumptions. *Journal of Geophysical Research: Solid Earth*, **112**(B6).
11
12 1651 Masturyono., McCaffrey, R., Wark, D. A., Roecker, S. W., Fauzi Ibrahim, G. & Sukhyar. (2001).
13 1652 Distribution of magma beneath Toba caldera complex, north Sumatra, Indonesia, constrained by
14
15 1653 three-dimensional P wave velocities, seismicity, and gravity. *Geochemistry Geophysics Geosystems*
16
17 1654 **2**, 1014.
18
19 1655 Matsushima, N., Oshima, H., Ogawa, Y., Takakura, S., Satoh, H., Utsugi, M., Nishida, Y. (2011).
20
21 1656 Magma prospecting in Usu volcano, Hokkaido, Japan, using magnetotelluric soundings. *Journal of*
22
23 1657 *Volcanology and Geothermal Research* **109**, 263-277.
24
25 1658 McBride, J. H., William Keach, R., Leetaru, H. E. & Smith, K. M. (2018). Visualizing Precambrian
26
27 1659 basement tectonics beneath a carbon capture and storage site, Illinois Basin. *Interpretation* **6**, T257-
28 1660 T270.
29
30 1661 McCabe, C., Jackson, M., Ellwood, B. B. (1985). Magnetic anisotropy in the Trenton limestone:
31
32 1662 results of a new technique, anisotropy of anhysteretic susceptibility. *Geophysical Research Letters*
33
34 1663 **12**, 333-336.
35
36 1664 McCormick Kilbride, B., Edmonds, M. & Biggs, J. (2016). Observing eruptions of gas-rich
37
38 1665 compressible magmas from space. *Nature communications* **7**, 13744.
39
40 1666 McKenzie, D. A. N., & O'Nions, R. K. (1991). Partial melt distributions from inversion of rare earth
41
42 1667 element concentrations. *Journal of Petrology* **32**, 1021-1091.
43
44 1668 McLean, C. E., Schofield, N., Brown, D. J., Jolley, D. W., Reid, A. (2017). 3D seismic imaging of
45
46 1669 the shallow plumbing system beneath the Ben Nevis Monogenetic Volcanic Field: Faroe-Shetland
47
48 1670 Basin. *Journal of the Geological Society* **174**, 468-485.
49
50 1671 Miller, V. & Savage, M. (2001). Changes in seismic anisotropy after volcanic eruptions: evidence
51
52 1672 from Mount Ruapehu. *Science* **293**, 2231-2233.
53
54
55
56
57
58
59
60

1
2
3
4
5
6
7
8
9
10
11
12
13
14
15
16
17
18
19
20
21
22
23
24
25
26
27
28
29
30
31
32
33
34
35
36
37
38
39
40
41
42
43
44
45
46
47
48
49
50
51
52
53
54
55
56
57
58
59
60

Miller, C. F., Furbish, D. J., Walker, B. A., Claiborne, L. L., Koteas, G. C., Bleick, H. A., Miller, J. S. (2011). Growth of plutons by incremental emplacement of sheets in crystal-rich host: evidence from Miocene intrusions of the Colorado River region, Nevada, USA. *Tectonophysics* **500**, 65-77.

Miller, K. J., Zhu, W., Montesi, L. G. J., Gaetani, G. A. (2014). Experimental quantification of permeability of partially molten mantle rock. *Earth and Planetary Science Letters* **388**, 273-282.

Miller, C. A., Le Mével, H., Currenti, G., Williams-Jones, G. & Tikoff, B. (2017). Microgravity changes at the Laguna del Maule volcanic field: Magma-induced stress changes facilitate mass addition. *Journal of Geophysical Research: Solid Earth* **122**, 3179-3196.

Mitchell, M. A., White, R. S., Roecker, S., Greenfield, T. (2013). Tomographic image of melt storage beneath Askja Volcano, Iceland using local microseismicity. *Geophysical Research Letters* **40**, 5040-5046.

Morgan, J. V., Warner, M., Bell, R. E., Ashley, J., Barnes, D., Little, R., Roele, K., Jones, C. (2013). Next-generation seismic experiments: wide-angle, multi-azimuth, three-dimensional, full-waveform inversion. *Geophysical Journal International* **195**, 1657-1678.

Morgan, J. V., Warner, M., Arnoux, G., Hooft, E., Toomey, D., VanderBeek, B., Wilcock, W. (2016). Next-generation seismic experiments – II: wide-angle, multi-azimuth, 3-D, full-waveform inversion of sparse field data. *Geophysical Journal International* **204**, 1342-1363.

Muirhead, J. D., Airoidi, G., White, J. D., Rowland, J. V. (2014). Cracking the lid: Sill-fed dikes are the likely feeders of flood basalt eruptions. *Earth and Planetary Science Letters* **406**, 187-197.

Neuberg, J., Baptie, B., Luckett, R., Stewart, R. (1998). Results from the broadband seismic network on Montserrat. *Geophysical Research Letters* **25(19)**, 3661-3664.

Neuberg, J., Tuffen, H., Collier, L., Green, D., Powell, T., Dingwell, D. (2006). The trigger mechanism of low-frequency earthquakes on Montserrat. *Journal of Volcanology and Geothermal Research* **153**, 37-50.

- 1
2
3
4
5
6 1697 Neves, S. P., Araújo, A. M., Correia, P. B. & Mariano, G. (2003). Magnetic fabrics in the Cabanas
7
8 1698 Granite (NE Brazil): interplay between emplacement and regional fabrics in a dextral transpressive
9
9 1699 regime. *Journal of Structural Geology* **25**, 441-453.
10
11 1700 Newman, A. V., Dixon, T. H., Gourmelen, N. (2006). A four-dimensional viscoelastic deformation
12
13 1701 model for Long Valley Caldera, California, between 1995 and 2000. *Journal of Volcanology and*
14
15 1702 *Geothermal Research* **150**(1), 244-269.
16
17 1703 O'Driscoll, B., Stevenson, C. T. E., Troll, V. R. (2008). Mineral lamination development in layered
18
19 1704 gabbros of the British Palaeogene Igneous Province: A combined anisotropy of magnetic
20
21 1705 susceptibility, textural and mineral chemistry study. *Journal of Petrology* **49**, 1187-1221.
22
23 1706 O'Driscoll, B., Ferré, E. C., Stevenson, C. T. E., Magee, C. (2015). The significance of
24
25 1707 magnetic fabrics in layered mafic-ultramafic intrusions. In: Charlier, B., Latypov, R., Namur,
26
27 1708 O., Tegner, C. (Eds), *Layered Intrusions*, Springer, 295-329.
28
29 1709 Okubo, P. G., Benz, H. M., Chouet, B. A. (1997). Imaging the crustal magma sources beneath
30
31 1710 Mauna Loa and Kilauea volcanoes, Hawaii. *Geology* **25**(10), 867-870.
32
33 1711 Orlický, O. (1990). Detection of magnetic carriers in rocks: results of susceptibility changes in
34
35 1712 powdered rock samples induced by temperature. *Physics of the Earth and Planetary Interiors*
36
37 1713 **63**, 66-70.
38
39 1714 Padilha, A. L., Vitorello, Í., Pádua, M. B., Bologna, M. S. (2006). Lithospheric and
40
41 1715 sublithospheric anisotropy beneath central-southeastern Brazil constrained by long period
42
43 1716 magnetotelluric data. *Physics of the Earth and Planetary Interiors* **158**, 190-209.
44
45 1717 Pagli, C., Wright, T. J., Ebinger, C. J., Yun, S. H., Cann, J. R., Barnie, T. & Ayele, A. (2012).
46
47 1718 Shallow axial magma chamber at the slow-spreading Erta Ale Ridge. *Nature Geoscience* **5**, 284-
48
49 1719 288.
50
51 1720 Parker, R. L. (1980). The inverse problem of electromagnetic induction: Existence and construction
52
53 1721 of solutions based on incomplete data. *Journal of Geophysical Research* **85**, 4421-4428.
54
55
56
57
58
59
60

1
2
3
4
5
6
7
8
9
10
11
12
13
14
15
16
17
18
19
20
21
22
23
24
25
26
27
28
29
30
31
32
33
34
35
36
37
38
39
40
41
42
43
44
45
46
47
48
49
50
51
52
53
54
55
56
57
58
59
60

Parks, M. M., Biggs, J., England, P., Mather, T. A., Nomikou, P., Palamartchouk, K., Papanikolaou, X., Paradissis, D., Parsons, B., Pyle, D. M., Raptakis, C. (2012). Evolution of Santorini Volcano dominated by episodic and rapid fluxes of melt from depth. *Nature Geoscience* **5**(10), 749-754.

Parker, A. L. (2016). InSAR Observations of Ground Deformation: Application to the Cascades Volcanic Arc. Springer Theses.

Parmigiani, A., Faroughi, S. A., Huber, C., Bachmann, O., Su, Y. (2016) Bubble accumulation and its role on the evolution of upper crustal magma reservoirs. *Nature* **532**, 492-495.

Paulatto, M., Minshull, T., Baptie, B., Dean, S., Hammond, J. O. S., Henstock, T., Kenedi, C., Kiddle, E., Malin, P., Peirce, C., Ryan, G. (2010). Upper crustal structure of an active volcano from refraction/reflection tomography, Montserrat, Lesser Antilles. *Geophysical Journal International* **180**, 685-696.

Paulatto, M., Annen, C., Henstock, T. J., Kiddle, E., Minshull, T. A., Sparks, R. S. J., Voight, B. (2012). Magma chamber properties from integrated seismic tomography and thermal modeling at Montserrat. *Geochemistry, Geophysics, Geosystems* **13**(1).

Pedersen, R. & Sigmundsson, F. (2006). Temporal development of the 1999 intrusive episode in the Eyjafjallajökull volcano, Iceland, derived from InSAR images. *Bulletin of Volcanology* **68**(4), 377-393.

Peron-Pinvidic, G., Shillington, D. J., Tuelholke, B. E. (2010). Characterization of sills associated with the U reflection on the Newfoundland margin: evidence for widespread early post-rift magmatism on a magma-poor rifted margin. *Geophysical Journal International* **182**, 113-136.

Petford, N., Cruden, A. R., McCaffrey, K. J. W. & Vigneresse, J. L. (2000). Granite magma formation, transport and emplacement in the Earth's crust. *Nature* **408**, 669-673.

Petronis, M. S., Delcamp, A., de Vries, B. V. W. (2013). Magma emplacement into the Lemptégy scoria cone (Chaîne Des Puys, France) explored with structural, anisotropy of magnetic susceptibility, and Paleomagnetic data. *Bulletin of Volcanology* **75**, 753.

- 1
2
3
4
5
6 1747 Petronis, M. S., Brister, A. R., Rapprich, V., de Vries, B. V. W., Lindline, J., Misurec, J. (2015).
7
8 1748 Emplacement history of the Trosky basanitic volcano (Czech Republic): paleomagnetic, rock
9
10 1749 magnetic, petrologic, and anisotropy of magnetic susceptibility evidence for lingering growth of a
11
12 1750 monogenetic volcano. *Journal of Geosciences* **60**, 129-147.
- 13 1751 Petrovský, E. & Kapička, A. (2006). On determination of the Curie point from thermomagnetic
14
15 1752 curves. *Journal of Geophysical Research* **111**, B12S27.
- 16
17 1753 Phillips, T. B., Magee, C., Jackson, C. A. L. & Bell, R. E. (2017). Determining the three-
18
19 1754 dimensional geometry of a dike swarm and its impact on later rift geometry using seismic reflection
20
21 1755 data. *Geology* **46**, 119-122.
- 22 1756 Pinel, V., Poland, M. P., Hooper, A. (2014). Volcanology: Lessons learned from synthetic aperture
23
24 1757 radar imagery. *Journal of Volcanology and Geothermal Research* **289**, 81-113.
- 25
26 1758 Planke, S., Symonds, P. A., Alvestad, E., Skogseid, J. (2000). Seismic volcanostratigraphy of large-
27
28 1759 volume basaltic extrusive complexes on rifted margins. *Journal of Geophysical Research: Solid*
29
30 1760 *Earth* **105**, 19335-19351.
- 31
32 1761 Planke, S., Rasmussen, T., Rey, S. S., Myklebust, R. (2005). Seismic characteristics and
33
34 1762 distribution of volcanic intrusions and hydrothermal vent complexes in the Vøring and Møre basins.
35
36 1763 In: Doré, A. G. (ed.) *Petroleum Geology: North-West Europe and Global Perspectives -*
37 1764 *Proceedings of the 6th Petroleum Geology Conference*: Geological Society, London, 833-844.
- 38
39 1765 Poland, M. P., Miklius, A., Sutton, A. J. and Thornber, C. R. (2012). A mantle-driven surge in
40
41 1766 magma supply to Kilauea Volcano during 2003-2007. *Nature Geoscience* **5**(4), 295-300.
- 42
43 1767 Poland, M. P. & Carbone, D. (2016). Insights into shallow magmatic processes at Kīlauea Volcano,
44
45 1768 Hawai'i, from a multiyear continuous gravity time series. *Journal of Geophysical Research: Solid*
46
47 1769 *Earth* **121**, 5477-5492.
- 48 1770 Pommier, A. (2014). Interpretation of magnetotelluric results using laboratory measurements.
49
50 1771 *Surveys in Geophysics* **35**, 41-84.

51
52
53
54
55
56
57
58
59
60

- 1
2
3
4
5
6 1772 Pommier, A., Tarits, P., Hautot, S., Pichavant, M., Scaillet, B. & Gaillard, F. (2010). A new
7
8 1773 petrological and geophysical investigation of the present-day plumbing system of Mount
9
10 1774 Vesuvius. *Geochemistry Geophysics Geosystems* **11**, Q07013.
- 11 1775 Pommier, A. & Le Trong, E. (2011). SIGMELTS: A web portal for electrical conductivity
12
13 1776 calculations in geosciences. *Computational Geoscience* **37**, 1450-1459.
14
- 15 1777 Pritchard, M. E. & Simons, M. (2004). An InSAR-based survey of volcanic deformation in the
16
17 1778 central Andes. *Geochemistry, Geophysics, Geosystems* **5**(2).
- 18
19 1779 Prutkin, I., Vajda, P. & Gottsmann, J. (2014). The gravimetric picture of magmatic and
20
21 1780 hydrothermal sources driving hybrid unrest on Tenerife in 2004/5. *Journal of Volcanology and*
22
23 1781 *Geothermal Research* **282**, 9-18.
- 24 1782 Reeves, J., Magee, C. & Jackson, C. A. L. (2018). Unravelling intrusion-induced forced fold
25
26 1783 kinematics and ground deformation using 3D seismic reflection data. *Volcanica* **1**, 1-17.
27
- 28 1784 Reich, H. (1932). Die Bedeutung der finnischen Schweremessungen für die angewandte Geophysik:
29
30 1785 Beitr. *Angew. Geophys., Ergänzungsh* **2**, 1-13.
- 31
32 1786 Richter, C. & van der Pluijm, B.A. (1994). Separation of paramagnetic and ferrimagnetic
33
34 1787 susceptibilities using low temperature magnetic susceptibilities and comparison with high field
35
36 1788 methods. *Physics of the Earth and Planetary Interiors* **82**, 113-123.
- 37 1789 Rivalta, E. & Segall, P. (2008). Magma compressibility and the missing source for some dike
38
39 1790 intrusions. *Geophysical Research Letters* **35**(4).
- 40
41 1791 Roberts, J. J. & Tyburczy, J. A. (1999). Partial-melt electrical conductivity: Influence of melt
42
43 1792 composition. *Journal of Geophysical Research* **104**, 7055-7065.
- 44
45 1793 Rocchi, S., Mazzotti, A., Marroni, M., Pandolfi, L., Costantini, P., Giuseppe, B., Biase, D. D.,
46
47 1794 Federici, F. & Lo, P. G. (2007). Detection of Miocene saucer-shaped sills (offshore Senegal) via
48
49 1795 integrated interpretation of seismic, magnetic and gravity data. *Terra Nova* **19**, 232-239.
- 50 1796 Rochette, P., Jackson, M., Aubourg, C. (1992). Rock magnetism and the interpretation of
51
52 1797 anisotropy of magnetic susceptibility. *Reviews of Geophysics* **30**, 209-226.
53
54
55
56
57
58
59
60

- 1
2
3
4
5
6 1798 Roman, D. C. & Cashman, K.V. (2006). The origin of volcano-tectonic earthquake swarms.
7
8 1799 *Geology* **34**, 457-460.
- 9
10 1800 Roman, D. C., Savage, M. K., Arnold, R., Latchman, J. L. & De Angelis, S. (2011). Analysis and
11 1801 forward modeling of seismic anisotropy during the ongoing eruption of the Soufrière Hills Volcano,
12 1802 Montserrat, 1996–2007. *Journal of Geophysical Research: Solid Earth* **116**, B03201.
- 13 1803 Ronchin, E., Masterlark, T., Dawson, J., Saunders, S., Marti Molist, J. (2017). Imaging the complex
14 1804 geometry of a magma reservoir using FEM-based linear inverse modeling of InSAR data:
15 1805 application to Rabaul Caldera, Papua New Guinea. *Geophysical Journal International* **209**, 1746-
16 1806 1760.
- 17 1807 Routh, P., Neelamani, R., Lu, R., Lazaratos, S., Braaksma, H., Hughes, S., Saltzer, R., Stewart, J.,
18 1808 Naidu, K., Averill, H. & Gottumukkula, V. (2017). Impact of high-resolution FWI in the western
19 1809 black sea: Revealing overburden and reservoir complexity. *The Leading Edge* **36**, 60-66.
- 20 1810 Rubin, A. & Gillard, D. (1998). Dike-induced earthquakes: Theoretical considerations. *Journal of*
21 1811 *Geophysical Research* **103**, 10017-10030.
- 22 1812 Rymer, H. & Brown, G. C. (1986). Gravity fields and the interpretation of volcanic structures:
23 1813 Geological discrimination and temporal evolution. *Journal of Volcanology and Geothermal*
24 1814 *Research* **27**, 229-254.
- 25 1815 Rymer, H., Locke, C. A., Brenes, J. & Williams-Jones, G. (2005). Magma plumbing processes for
26 1816 persistent activity at Poas volcano, Costa Rica. *Geophysical Research Letters* **32**, L08307.
- 27 1817 Salzer, J. T., Nikkhoo, M., Walter, T. R., Sudhaus, H., Reyes-Dávila, G., Bretón, M., Arámbula, R.
28 1818 (2014). Satellite radar data reveal short-term pre-explosive displacements and a complex conduit
29 1819 system at Volcán de Colima, Mexico. *Frontiers in Earth Science* **2**, 12.
- 30 1820 Samrock, F., Kuvshinov, A., Bakker, J., Jackson, A., Fisseha, S. (2015). 3D analysis and
31 1821 interpretation of Magnetotelluric data from the Aluto-Langano geothermal field, Ethiopia.
32 1822 *Geophysical Journal International* **202**, 1923-1948

1
2
3
4
5
6
7
8
9
10
11
12
13
14
15
16
17
18
19
20
21
22
23
24
25
26
27
28
29
30
31
32
33
34
35
36
37
38
39
40
41
42
43
44
45
46
47
48
49
50
51
52
53
54
55
56
57
58
59
60

- Saunders, K., Blundy, J. D., Dohmen, R., Cashman, K. (2012). Linking Petrology and Seismology at an active volcano. *Science* **336**, 1023-1027.
- Saxby, J., Gottsmann, J., Cashman, K. & Gutiérrez, E. (2016). Magma storage in a strike-slip caldera. *Nature Communications* **7**, 12295.
- Schaefer, L. N., Lu, Z., Oommen, T. (2015). Dramatic volcanic instability revealed by InSAR. *Geology* **43**, 743-746.
- Schmeling, H. (1986). Numerical models on the influence of partial melt on elastic, anelastic and electrical properties of rocks. Part II: electrical conductivity. *Physics of Earth and Planetary Interiors* **43**, 123-136.
- Schofield, N., Stevenson, C., Reston, T. (2010). Magma fingers and host rock fluidization in the emplacement of sills. *Geology* **38**, 63-66.
- Schofield, N., Heaton, L., Holford, S. P., Archer, S. G., Jackson, C. A. L., Jolley, D. W. (2012a). Seismic imaging of 'broken bridges': linking seismic to outcrop-scale investigations of intrusive magma lobes. *Journal of the Geological Society of London* **169**, 421-426.
- Schofield, N. J., Brown, D. J., Magee, C., Stevenson, C. T. E. (2012b) Sill morphology and comparison of brittle and non-brittle emplacement mechanisms. *Journal of the Geological Society of London* **169**, 127-141.
- Schofield, N., Holford, S., Millett, J., Brown, D., Jolley, D., Passey, S., Muirhead, D., Grove, C., Magee, C., Murray, J., Hole, M., Jackson, C., Stevenson, C. (2017). Regional Magma Plumbing and emplacement mechanisms of the Faroe-Shetland Sill Complex: Implications for magma transport and petroleum systems within sedimentary basins. *Basin Research* **29**, 41-63.
- Segall, P. (2010). *Earthquake and volcano deformation*. Princeton University Press.
- Shalev, E., Kenedi, C. L., Malin, P., Voight, V., Miller, V., Hidayat, D., Sparks, R. S. J., Minshull, T., Paulatto, M., Brown, L. & Mattioli, G. (2010). Three-dimensional seismic velocity tomography of Montserrat from the SEA-CALIPSO offshore/onshore experiment. *Geophysical Research Letters* **37**, L00E17.

- 1
2
3
4
5
6 1849 Sigmundsson, F., Hreinsdóttir, S., Hooper, A., Árnadóttir, T., Pedersen, R., Roberts, M.J.,
7
8 1850 Óskarsson, N., Auriac, A., Decriem, J., Einarsson, P., Geirsson, H. (2010). Intrusion triggering of
9
10 1851 the 2010 Eyjafjallajökull explosive eruption. *Nature* **468**(7322), 426-430.
- 11 1852 Sigmundsson, F. & 37 others (2015). Segmented lateral dyke growth in a rifting event at
12
13 1853 Bardabunga volcanic system, Iceland. *Nature* **517**, 191-195.
- 14
15 1854 Sigmundsson, F. (2016). New insights into magma plumbing along rift systems from detailed
16
17 1855 observations of eruptive behavior at Axial volcano. *Geophysical Research Letters* **43**, 12.423-
18
19 1856 12.427.
- 20
21 1857 Simons, M. & P. A. Rosen. (2007). Interferometric synthetic aperture radar geodesy. *Treatise on*
22
23 1858 *Geophysics - Geodesy* **3**, 391-446, Elsevier, Amsterdam.
- 24 1859 Simpson, F. & Bahr, K. (2005). *Practical Magnetotellurics*. Cambridge University Press,
25
26 1860 Cambridge, UK.
- 27
28 1861 Singer, B. S., Andersen, N. L., Le Mével, H., Feigl, K. L., DeMets, C., Tikoff, B., Thurber, C. H.,
29
30 1862 Jicha, B. R., Cardona, C., Córdova, L. and Gil, F. (2014). Dynamics of a large, restless, rhyolitic
31
32 1863 magma system at Laguna del Maule, southern Andes, Chile. *GSA Today* **24**, 4-10.
- 33 1864 Sirgue, L., Barkved, O. I., Dellinger, J., Etgen, J., Albertin, U., Kommedal, J. H. (2010) Full
34
35 1865 waveform inversion: the next leap forward in imaging at Valhall. *First Break* **28**, 65-70.
- 36
37 1866 Smallwood, J. R. & Maresh, J. (2002). The properties, morphology and distribution of igneous sills:
38
39 1867 modelling, borehole data and 3D seismic from the Faroe-Shetland area. In: Jolley, D. W. & Bell, B.
40
41 1868 R. (eds.) *The North Atlantic Igneous Province: Stratigraphy, tectonic, Volcanic and Magmatic*
42
43 1869 *Processes*: Geological Society, London, Special Publications, 271-306.
- 44 1870 Sofyan, Y., Kamah, Y., Nishijima, J., Fujimitsu, Y., Ehara, S., Fukuda, Y. & Taniguchi, M. (2011).
45
46 1871 Mass variation in outcome to high production activity in Kamojang Geothermal Field, Indonesia: A
47
48 1872 reservoir monitoring with relative and absolute gravimetry. *Earth, Planets and Space* **63**, 1157-
49
50 1873 1167.

Formatted: Font: Italic, English (U.S.), Do not check spelling or grammar

Formatted: Font: Bold, English (U.S.), Do not check spelling or grammar

1
2
3
4
5
6
7
8
9
10
11
12
13
14
15
16
17
18
19
20
21
22
23
24
25
26
27
28
29
30
31
32
33
34
35
36
37
38
39
40
41
42
43
44
45
46
47
48
49
50
51
52
53
54
55
56
57
58
59
60

Solano, J. M. S., Jackson, M. D., Sparks, R. S. J., Blundy, J. D., Annen, C. (2012). Melt segregation in deep crustal hot zones: a mechanism for chemical differentiation, crustal assimilation and the formation of evolved magmas. *Journal of Petrology* **53**, 1999-2026.

Sparks, R., Biggs, J., Neuberg, J. (2012). Monitoring volcanoes. *Science* **335**, 1310-1311.

Stacey, F. D., Joplin, G., Lindsay, J. (1960). Magnetic anisotropy and fabric of some foliated rocks from S.E. Australia. *Pure Applied Geophysics* **47**, 30-40.

Stankiewicz, J., Ryberg, T., Haberland, C., Natawidjaja, D. (2010). Lake Toba volcano magma chamber imaged by ambient seismic noise tomography. *Geophysical Research Letters* **37**, L17306.

Stephenson, A. (1994). Distribution anisotropy: two simple models for magnetic lineation and foliation. *Physics of the Earth and Planetary Interiors* **82**, 49-53.

Sternberg, B., Washburne, J. C., Pellerin, L. (1988). Correction for the static shift in magnetotellurics using transient electromagnetic soundings. *Geophysics* **53**, 1459-1468.

Stevenson, C. T. E., Owens, W. H., Hutton, D. H. W. (2007a). Flow lobes in granite: the determination of magma flow direction in the Trawenagh Bay Granite, N.W. Ireland, using anisotropy of magnetic susceptibility. *Geological Society of America Bulletin* **119**, 1368-1386.

Stevenson, C. T. E., Owens, W. H., Hutton, D. H. W., Hood, D. N., Meighan, I. G. (2007b). Laccolithic, as opposed to cauldron subsidence, emplacement of the Eastern Mourne pluton, N. Ireland: evidence from anisotropy of magnetic susceptibility. *Journal of the Geological Society of London* **164**, 99-110.

Stork, A., Stuart, G. W., Henderson, C. M., Keir, D., Hammond, J. O. S. (2013). Uppermost mantle (Pn) velocity model for the Afar region, Ethiopia: An insight into rifting processes. *Geophysical Journal International* **193**, 321-328.

Stuart, G. W., Bastow, I. D., Ebinger, C. J. (2006). Crustal structure of the Northern Main Ethiopian rift from receiver function studies. In: Yirgu, G., Ebinger, C. J., Maguire, P. K. H. (eds) *The Afar Volcanic Province within the East African Rift System. Geological Society, London, Special Publications* **259**, 253-267.

- 1
2
3
4
5
6 1900 Sturkell, E., Einarsson, P., Sigmundsson, F., Geirsson, H., Olafsson, H., Pedersen, R., de Zeeuw-
7
8 1901 van Dalfsen, E., Linde, A.T., Sacks, S.I., Stefánsson, R. (2006). Volcano geodesy and magma
9
10 1902 dynamics in Iceland. *Journal of Volcanology and Geothermal Research* **150**, 14-34.
- 11 1903 Svensen, H., Corfu, F., Polteau, S., Hammer, Ø., Planke, S. (2012). Rapid magma emplacement in
12
13 1904 the Karoo Large Igneous Province. *Earth and Planetary Science Letters* **325-326**, 1-9.
- 14
15 1905 Symonds, P. A., Planke, S., Frey, O., Skogseid, J. (1998). Volcanic evolution of the Western
16
17 1906 Australian Continental Margin and its implications for basin development. *The Sedimentary Basins*
18
19 1907 *of Western Australia 2: Proc. of Petroleum Society Australia Symposium, Perth, WA.*
- 20
21 1908 Takada, Y. & Fukushima, Y. (2013). Volcanic subsidence triggered by the 2011 Tohoku earthquake
22
23 1909 in Japan. *Nature Geoscience* **6**(8), 637-641.
- 24 1910 Takei, Y. (2002). Effect of pore geometry on V-P/V-S: From equilibrium geometry to crack.
25
26 1911 *Journal of Geophysical Research-Solid Earth* **107**, 2043.
- 27
28 1912 Tarantola, A. (1984) Inversion of seismic reflection data in the acoustic approximation. *Geophysics*
29
30 1913 **49**, 1259-1266.
- 31
32 1914 Tarling, D. H. & Hrouda, F. (1993). *The Magnetic Anisotropy of Rocks*, Chapman and Hall, New
33
34 1915 York, pp. 1-232.
- 35 1916 Tauxe, L. (1998). *Paleomagnetic Principles and Practice*. In: *Of Modern approaches in geophysics*,
36
37 1917 vol. 17: Kluwer Academic Publishers, Dordrecht, Boston, London.
- 38
39 1918 Thiele, S., Micklethwaite, S., Bourke, P., Verrall, M., Kovési, P. (2015). Insights into the mechanics
40
41 1919 of en-echelon sigmoidal vein formation using ultra-high resolution photogrammetry and computed
42
43 1920 tomography. *Journal of Structural Geology* **77**, 27-54.
- 44
45 1921 Thomas, M. E. & Neuberg, J. (2012). What makes a volcano tick - A first explanation of deep
46
47 1922 multiple seismic sources in ascending magma. *Geology* **40**, 351-354.
- 48 1923 Thomson, K. (2007). Determining magma flow in sills, dykes and laccoliths and their implications
49
50 1924 for sill emplacement mechanisms. *Bulletin of Volcanology* **70**, 183-201.

51
52
53
54
55
56
57
58
59
60

1
2
3
4
5
6
7
8
9
10
11
12
13
14
15
16
17
18
19
20
21
22
23
24
25
26
27
28
29
30
31
32
33
34
35
36
37
38
39
40
41
42
43
44
45
46
47
48
49
50
51
52
53
54
55
56
57
58
59
60

- Thomson, K. & Hutton, D. (2004). Geometry and growth of sill complexes: insights using 3D seismic from the North Rockall Trough. *Bulletin of Volcanology* **66**, 364-375.
- Tizzani, P., Battaglia, M., Zeni, G., Atzori, S., Berardino, P. & Lanari, R. (2009). Uplift and magma intrusion at Long Valley caldera from InSAR and gravity measurements. *Geology* **37**, 63-66.
- Tolstoy, M., Waldhauser, F., Bohnenstiehl, D. R., Weekly, R. T., Kim, W. -Y. (2008). Seismic identification of along-axis hydrothermal flow on the East Pacific Rise. *Nature* **451**, 181-184.
- Trasatti, E., Giunchi, C. & Agostinetti, N. P. (2008). Numerical inversion of deformation caused by pressure sources: application to Mount Etna (Italy). *Geophysical Journal International* **172**, 873-884.
- Trindade, R. I. F., Nguema, T. M. M., Bouchez, J. L. (2001). Thermally enhanced mimetic fabric of magnetite in a biotite granite. *Geophysical Research Letters* **28**, 2687-2690.
- Trude, J., Cartwright, J., Davies, R. J. & Smallwood, J. (2003). New technique for dating igneous sills. *Geology* **31**, 813-816.
- Tuffen, H., Smith, R., Sammonds, P. R. (2008). Evidence for seismogenic fracture of silicic magma. *Nature* **453**, 511-514.
- Van Camp, M., de Viron, O., Watlet, A., Meurers, B., Francis, O. & Caudron, C. (2017). Geophysics from terrestrial time-variable gravity measurements. *Reviews of Geophysics* **55**, 938-992.
- Vargas-Bracamontes, D. M. & Neuberg, J. W. (2012). Interaction between regional and magma-induced stresses and their impact on volcano-tectonic seismicity. *Journal of Volcanology and Geothermal Research* **243**, 91-96.
- Vasuki, Y., Holden, E. -J., Kovesi, P., Micklethwaite, S. (2014) Semi-automatic mapping of geological Structures using UAV-based photogrammetric data: An image analysis approach. *Computers and Geosciences* **69**, 22-32.

- 1
2
3
4
5
6 1949 Vasuki, Y., Holden, E. -J., Kovesi, P., Micklethwaite, S. (2017). An interactive image segmentation
7
8 1950 method for lithological boundary detection: A rapid mapping tool for geologists. *Computers and*
9
10 1951 *Geosciences* **100**, 27-40.
- 11 1952 Verwey, E. J. W. (1939). Electronic conduction of magnetite (Fe₃O₄) and its transition point at low
12
13 1953 temperatures. *Nature* **144**, 327-328.
14
- 15 1954 Vigh, D., Starr, B., Kapoor, J., Li, H. (2010) 3D full waveform inversion on a GOM data set. *80th*
16
17 1955 *Annual International Meeting, SEG, Expanded Abstracts*.
- 18
19 1956 Vigneresse, J. L. (1995). Crustal regime of deformation and ascent of granitic magma.
20
21 1957 *Tectonophysics* **249**, 187-202.
- 22 1958 Vigneresse, J. L., Tikoff, B. & Améglio, L. (1999). Modification of the regional stress field by
23
24 1959 magma intrusion and formation of tabular granitic plutons. *Tectonophysics* **302**, 203-224.
25
- 26 1960 Voigt, W. & Kinoshita, S. (1907). Bestimmung absoluter Werte von Magnetisierungszahlen,
27
28 1961 insbesondere für Kristalle. *Annalen der Physik* **329**, 492-514.
- 29
30 1962 Vollgger, S. A. & Cruden, A. R. (2016). Mapping folds and fractures in basement and cover rocks
31
32 1963 using UAV photogrammetry, Cape Liptrap and Cape Paterson, Victoria, Australia. *Journal of*
33
34 1964 *Structural Geology* **85**, 168-187.
- 35 1965 Waite, G. P. & Moran, S. C. (2009). VP Structure of Mount St. Helens, Washington, USA, imaged
36
37 1966 with local earthquake tomography. *Journal of Volcanology and Geothermal Research* **182**, 113-122.
38
- 39 1967 Wall, M., Cartwright, J., Davies, R. & McGrandle, A. (2010). 3D seismic imaging of a Tertiary Dyke
40
41 1968 Swarm in the Southern North Sea, UK. *Basin Research* **22**, 181-194.
- 42
43 1969 Wannamaker, P. E., Hasterok, D. P., Johnston, J. M., Stodt, J. A., Hall, D. B., Sodergren, T. L.,
44
45 1970 Pellerin, L., Maris, V., Doerner, W. M., Groenewold, K. A., Unsworth, M. J. (2008). Lithospheric
46
47 1971 dismemberment and magmatic processes of the Great Basin–Colorado Plateau transition, Utah,
48
49 1972 implied from magnetotellurics. *Geochemistry, Geophysics, Geosystems* **9**, Q05019.
- 50 1973 Ward, K. M., Zandt, G., Beck, S. L., Christensen, D. H. & McFarlin, H. (2014). Seismic imaging of
51
52 1974 the magmatic underpinnings beneath the Altiplano-Puna volcanic complex from the joint inversion of
53
54
55
56
57
58
59
60

- 1
2
3
4
5
6 1975 surface wave dispersion and receiver functions. *Earth and Planetary Science Letters* **404**, 43-53.
- 7
8 1976 Warner, M., Ratclie, A., Nangoo, T., Morgan, J., Umpleby, A., Shah, N., Vinje, V., Stekl, I., Guasch,
9
10 1977 L., Win, C., Conroy, G., Bertrand, A. (2013). Anisotropic 3D full-waveform inversion. *Geophysics*
11
12 1978 **78**, R59-R80.
- 13 1979 Wauthier, C., Roman, D. C., Poland, M. P. (2013). Moderate-magnitude earthquakes induced by
14
15 1980 magma reservoir inflation at Kīlauea Volcano, Hawaii. *Geophysical Research Letters* **40**(20), 5366-
16
17 1981 5370.
- 18
19 1982 Wawrzyniak, P., Zlotnicki, J., Sailhac, P., Marquis, G. (2017). Resistivity variations related to the
20
21 1983 large March 9, 1998 eruption at La Fournaise volcano inferred by continuous MT monitoring.
22
23 1984 *Journal of Volcanology and Geothermal Research* **347**, 185-206.
- 24 1985 Weaver, J. (1994). *Mathematical methods for geo-electromagnetic induction*. Research Studies
25
26 1986 Press.
- 27
28 1987 Westoby, M. J., Brasington, J., Glasser, N. F., Hambrey, M. J., Reynolds, J. M. (2012). "Structure-
29
30 1988 from-Motion" photogrammetry: A low-cost, effective tool for geoscience applications.
31
32 1989 *Geomorphology* **179**, 300-314.
- 33
34 1990 Whaler, K. A. & Hautot, S. (2006). The electrical resistivity structure of the crust beneath the
35
36 1991 northern Main Ethiopian Rift. In: Yirgu, G., Ebinger, C. J., Maguire, P. K. H. (eds) The Afar
37 1992 Volcanic Province within the East African Rift System. *Geological Society, London, Special*
38
39 1993 *Publications* **259**, 293-305.
- 40
41 1994 White, R. & McCausland, W. (2016). Volcano-tectonic earthquakes: A new tool for estimating
42
43 1995 intrusive volumes and forecasting eruptions. *Journal of Volcanology and Geothermal Research*
44
45 1996 **309**, 139-155.
- 46 1997 Wicks, C.W., Thatcher, W., Dzurisin, D., Svarc, J. (2006). Uplift, thermal unrest and magma
47
48 1998 intrusion at Yellowstone caldera. *Nature* **440**(7080), 72-75.
- 49
50 1999 Yamasaki, T., Kobayashi, T., Wright, T. J., Fukahata, Y. (2018). Viscoelastic crustal deformation by
51
52 2000 magmatic intrusion: A case study in the Kutcharo caldera, eastern Hokkaido, Japan. *Journal of*
53
54
55
56
57
58
59
60

1
2
3
4
5
6
7
8
9
10
11
12
13
14
15
16
17
18
19
20
21
22
23
24
25
26
27
28
29
30
31
32
33
34
35
36
37
38
39
40
41
42
43
44
45
46
47
48
49
50
51
52
53
54
55
56
57
58
59
60

Volcanology and Geothermal Research **349**, 128-145.

Zandomeneghi, D., Aster, R., Kyle, P., Barclay, A., Chaput, J., Knox, H. (2013). Internal structure of Erebus volcano, Antarctica imaged by high-resolution active-source seismic tomography and coda interferometry. *Journal of Geophysical Research-Solid Earth* **118**, 1067–1078.

7. Figure captions

Figure 1: Schematic of a vertically extensive, transcrustal magma plumbing system involving transient, interconnected, relatively low-volume tabular magma intrusions (e.g., dykes, sills, and laccoliths) within a crystal mush (based on Cashman *et al.*, 2017; Cruden *et al.*, 2018).

Figure 2: (A) Interferograms showing fringes caused by the pressurisation of a point source directly beneath a stratovolcano from both ascending and descending satellite lines of sight. Note that the centre of the fringes are slightly offset from the summit of the volcano (marked by a black triangle). (B) Typical fringe patterns for analytical deformation sources in an elastic half space from ascending satellite geometry: (i) Mogi source at 5 km depth; (ii) dyke extending between depths of 3 and 9 km; (iii) rectangular sill; and (iv) a penny-shaped horizontal crack both at 5 km depth.

Figure 3: (A) Ascending line of sight (LOS) co-eruptive interferogram from the 2008 basalt lava extrusion between the Alu and Alu South domes and the Dalafilla stratovolcano (modified from Pagli *et al.*, 2012). (B) Inversion of uplift and subsidence patterns, recorded by InSAR during the 2008 basalt lava eruption at the Alu dome in the Danakil Depression, suggested ground deformation could be attributed to a combination of: (i) deflation of a reservoir, modelled as a Mogi source, at ~4 km depth; (ii) inflation and deflation of a tabular sill at ~1 km depth; and (iii) opening of a dyke beneath the eruptive fissure (Figs 3A and B) (Pagli *et al.*, 2012). See Figure 3A for location. (C) Geological map showing that lava flows radiate out from Alu and originate from the periphery of

1
2
3
4
5
6 2027 the dome, which is cross-cut by an array of randomly oriented faults (modified from Magee *et al.*,
7
8 2028 2017). (D) Magee *et al.*, (2017) inferred Alu is underlain by a saucer-shaped sill plumbing system,
9
10 2029 based on field observations and comparison to seismic reflection data, not a tabular sill (Fig. 3B).

11
12 2030
13 2031 Figure 4: Example of integrating seismology and petrology to constrain time-scales of magma
14
15 2032 storage and recharge (from Saunders *et al.*, 2012). Calculated Fe-Mg diffusion time scales of
16
17 2033 orthopyroxene crystals compared to monitoring data for the same eruptive period for Mount St.
18
19 2034 Helens. (A) The seismic record of depth against time of the 1980–1986 eruption sequence. (B)
20
21 2035 Measured flux of SO₂ gas. (C) Calculated age of orthopyroxene rim growth binned by month for the
22
23 2036 entire population. The age recorded is the month in which the orthopyroxene rim growth was
24
25 2037 triggered by magmatic perturbation. The black line displays the running average (over five points,
26
27 2038 equivalent to the average calculated uncertainty in calculated time scales) of all the data. The peaks
28
29 2039 in the diffusion time series correspond to episodes of deep seismicity in 1980 and 1982 and to
30
31 2040 elevated SO₂ flux in 1980 and possibly 1982. (D) Running average of the orthopyroxene rim time
32
33 2041 scales, displaying reverse zonation (Mg-rich rims) in blue and normal zonation (Fe-rich rims) in
34
35 2042 green. There are reverse zonation peaks in the early 1980, probably due to rejuvenation of the
36
37 2043 magma system by hotter pulses, whereas Fe-rich rims are more dominant from 1982 on. Vertical
38
39 2044 dashed grey lines represent the volcanic eruptions.

40
41 2045
42 2046 Figure 5: Plot of melt inclusion saturation and earthquake hypocentre depths, which suggest magma
43
44 2047 storage occurred at 1–5 km depths, beneath the Dabbahu volcanic system in Afar, Ethiopia
45
46 2048 (modified from Field *et al.*, 2012). Melt inclusion data obtained from analyses of alkali feldspar,
47
48 2049 clinopyroxene, and olivine phenocrysts within Dabbahu lavas <8 Kyr (Field *et al.*, 2012).
49
50 2050 Earthquake data recorded during the 2005 dyke event (Ebinger *et al.*, 2008).

1
2
3
4
5
6
7
8
9
10
11
12
13
14
15
16
17
18
19
20
21
22
23
24
25
26
27
28
29
30
31
32
33
34
35
36
37
38
39
40
41
42
43
44
45
46
47
48
49
50
51
52
53
54
55
56
57
58
59
60

Figure 6: (A) P-wave (V_p) tomography beneath Montserrat (black outline), highlighting the location of fast and slow seismic velocity anomalies (i.e. $>6\%$ faster or slower than average) relative to the location of the Silver Hills (SH), Central Hills (CH), and Soufrière Hills (SHV) volcanoes (modified from Shalev *et al.*, 2010). The fast velocity anomalies, interpreted to represent solidified andesitic intrusions underlie the volcanoes (Shalev *et al.*, 2010).

Figure 7: Static and dynamic gravimetric investigations of two active silicic magmatic systems in the Andes: Uturuncu volcano (Bolivia; A, C, and E) and the Laguna del Maule volcanic field (Chile; B, D, and F). (A) 3D view of the isosurface corresponding to the -120 kg m^3 density contrast beneath Uturuncu volcano, derived from Bouguer gravity data, interpreted to reflect a large ($\sim 750 \text{ km}^3$) plumbing system composed of a lower ($< 10 \text{ km}$) partially molten reservoir and upper, fractured and fluid-bearing solidified intrusions above sea level (after del Potro *et al.*, 2013). (B) 3D view of the -600 kg m^3 density contrast isosurface beneath the Laguna del Maule, which is interpreted to define a magma reservoir ($> 50\%$ melt) within a larger region of a crystal mush system; the 2D planes show slices through the dataset (Miller *et al.*, 2017). Elevation above sea level (a.s.l.) shown. See Figure 7D for area of data coverage. (C) Map of the 55 km long, dynamic gravity network (white circles) installed to track changes in gravity over time and space at Uturuncu volcano between 2010 and 2013 (modified from Gottsmann *et al.*, 2017). (D) Spatio-temporal residual gravity changes at Laguna del Maule recorded from 2013–2014, after correcting for deformation effects (modified from Miller *et al.*, 2017). (E) Gravity and deformation data, recorded from Uturuncu from 2010–2013, plotted against the measured free-air gravity gradient (solid red line) and associated errors (broken red lines) (modified from Gottsmann *et al.*, 2017). The data follow the gradient and are indicative of a subsurface density change as a cause of the uplift, possibly reflecting the release of fluids from a large deep-seated magma reservoir (i.e. the Altiplano-Puna Magmatic Body; Chmielowski *et al.*, 1999) through the vertically extensive crystal mush system shown in (A) (Gottsmann *et al.*, 2017). (F) Plot of gravity against horizontal distance

1
2
3
4
5
6 2078 for the source centre at Laguna del Maule (modified from Miller *et al.*, 2017). The increase in
7
8 2079 gravity of up to 120 μGal is explained by a hydrothermal fluid injection focused along a fault
9
10 2080 system, shown in (D), at 1.5–2 km depth as a result of a deeper seated magma injection, and is best
11
12 2081 modelled by a vertical rectangular prism source.

13 2082
14
15 2083 Figure 8: Gravity changes and deformation at the restless Long Valley caldera. (A) Map of the
16
17 2084 Long Valley caldera, California, USA, which hosts a resurgent dome (black outline), to highlight
18
19 2085 changes in residual gravity between 1982 and 1999 (modified from Tizzani *et al.*, 2009). (B) Plot of
20
21 2086 ground uplift and residual gravity changes with radial distance from the centre of the resurgent
22
23 2087 dome in (A) (modified from Tizzani *et al.*, 2009). The correlation between uplift and positive
24
25 2088 gravity residuals across the resurgent dome indicates ground deformation was instigated by
26
27 2089 intrusion of magma (Tizzani *et al.*, 2009).

28 2090
29
30 2091 Figure 9: (A) Map showing MT stations deployed around Volcán Uturuncu (U) and Volcán
31
32 2092 Quetena (Q), relative to areas of uplift and subsidence (modified from Comeau *et al.*, 2015). The
33
34 2093 white box shows area of modelled 3D MT data (Comeau *et al.*, 2015). (B) Regional 2D
35
36 2094 magnetotelluric line through the Altiplano-Puna magma body (APMB) highlighting the position of
37
38 2095 Volcán Uturuncu (modified from Comeau *et al.*, 2015). The APMB corresponds to a large,
39
40 2096 conductive (i.e. low-resistivity) body (Comeau *et al.*, 2015; Comeau *et al.*, 2016). Above the APMB
41
42 2097 are other areas of low-resistivity (e.g., C4) that are likely upper crustal magma reservoirs and dykes
43
44 2098 (Comeau *et al.*, 2016). C1–C7 and R1–R2 identify discrete zones of marked conductivity or
45
46 2099 resistivity, respectively (see Comeau *et al.*, 2015; Comeau *et al.*, 2016 for details). The white box
47
48 2100 shows area of modelled 3D MT data (Comeau *et al.*, 2015). See Figure 9A for location.

49
50 2101 Figure 10: (A) Interpreted seismic section and geological map showing the distribution of and
51
52 2102 connectivity between sills within the Faroe-Shetland Basin (modified from Schofield *et al.*, 2017).

1
2
3
4
5

6 Mapping of magma flow patterns within individual sills reveals that the sill-complex facilitates
7 extensive vertical and lateral magma transport. Magma was fed into the sedimentary basin via
8 basement-involved faults. TWT = two-way travel time. (B) Interpreted seismic section and
9 geological map describing the spatial relationship between volcanoes/vents and sills, inferred to
10 represent the magma plumbing system, emplaced at ~42 Ma (modified from Jackson *et al.*, 2013;
11 Magee *et al.*, 2013a). Sills are laterally offset from the volcanoes/vents summits. No 'magma
12 chambers' are observed in the seismic data, which images down to ~8 s TWT (i.e. ~>10 km)
13 (Magee *et al.*, 2013a).

14
15
16
17
18
19
20
21
22 Figure 11: (A) Interpreted seismic section from the Exmouth Sub-basin offshore NW Australia,
23 which images a saucer-shaped sill that is overlain by a forced fold and feeds a small vent from its
24 inclined limb (modified from Magee *et al.*, 2013b). See Figure 11B for line location). (B) Time-
25 structure map of the folded horizon (thick black line) in (A), highlighting fault traces and vent
26 locations and thicknesses (modified from Magee *et al.*, 2013b). (C) Seismic section from the
27 Farsund Basin, offshore southern Norway, which images part of a dyke-swarm that has been rotated
28 by basin flexure post-emplacment (modified from Phillips *et al.*, 2017).

29
30
31
32
33
34
35
36
37 Figure 12: (A) At the sample scale, all magnetic grains create a magnetic fabric. (i) Dominantly
38 prolate fabric, where K_2 and K_3 are least certain and form a girdle. Only the magnetic lineation (K_1)
39 can be confidently determined. (ii) When $K_1 > K_2 > K_3$, both a foliation (K_1-K_2) and a lineation (K_1)
40 may be discerned, defining a triaxial fabric. (iii) When K_1 and K_2 are equally uncertain and form a
41 girdle, K_3 is perpendicular to a foliation. (B) Schematic representation of how magma flow within a
42 planar sheet intrusion can produce imbricated magnetic fabrics at its margins, the closure of which
43 define the magma flow direction (after Féménias *et al.*, 2004). (C) AMS data and interpretations
44 from part of the Trawenagh Bay Granite, NW Ireland (adapted from Stevenson *et al.*, 2007a). (i)
45 AMS foliation traces are shown in blue and lineation traces in red. Lobes were defined in this

51
52
53
54
55
56
57
58
59
60

1
2
3
4
5
6
7
8
9
10
11
12
13
14
15
16
17
18
19
20
21
22
23
24
25
26
27
28
29
30
31
32
33
34
35
36
37
38
39
40
41
42
43
44
45
46
47
48
49
50
51
52
53
54
55
56
57
58
59
60

intrusion based on foliations curving around a lineation axis. In some lobes, the magnetic lineation trend was parallel to this axis, whilst in others they tended to splay or converge down flow. (ii) 3D sketch showing the geometry of three of the lobes (numbered in part i).

Figure 13: (A) Starting model derived from smoothed, pre-stack, time-migrated (PSTM) stacking velocities. (B) Final 2D FWI-derived velocity model obtained using 10 km streamer data and inversion frequencies of between 2.5 and 24 Hz. (C) FWI velocity model overlain by the 2D pre-stack, depth-migrated (PSDM) section. Strong irregular reflections in the lower half of the section are from basaltic intrusions, which appear as high-velocity anomalies in the FWI velocity model. Both the FWI velocity model and the PSDM pick out a major unconformity, and show shallow channels in the upper parts of the section (redrawn from Kalincheva *et al.*, 2017).

Figure 14: (A) UAV orthophotograph of the wave cut platform at Bingie Point, NSW, Australia showing the distribution of Palaeogene dolerite (Dol) and dacite (Dac) dykes within Devonian tonalite (Ton), diorite (Di), and aplite (Ap) host rocks. (B) Circular histogram of joint sets measured in the Devonian rocks from the orthophotograph; the dominant (purple) set is parallel to and likely contemporaneous with the Palaeogene dykes. (C) Annotated close-up image highlighting dykes and structural features. The northern dacite dyke shows two broken bridge (BB) structures, whilst the central dolerite dyke displays prominent step structures (S). Narrow apophyses are also associated with the broken bridges and steps.

Figure 1

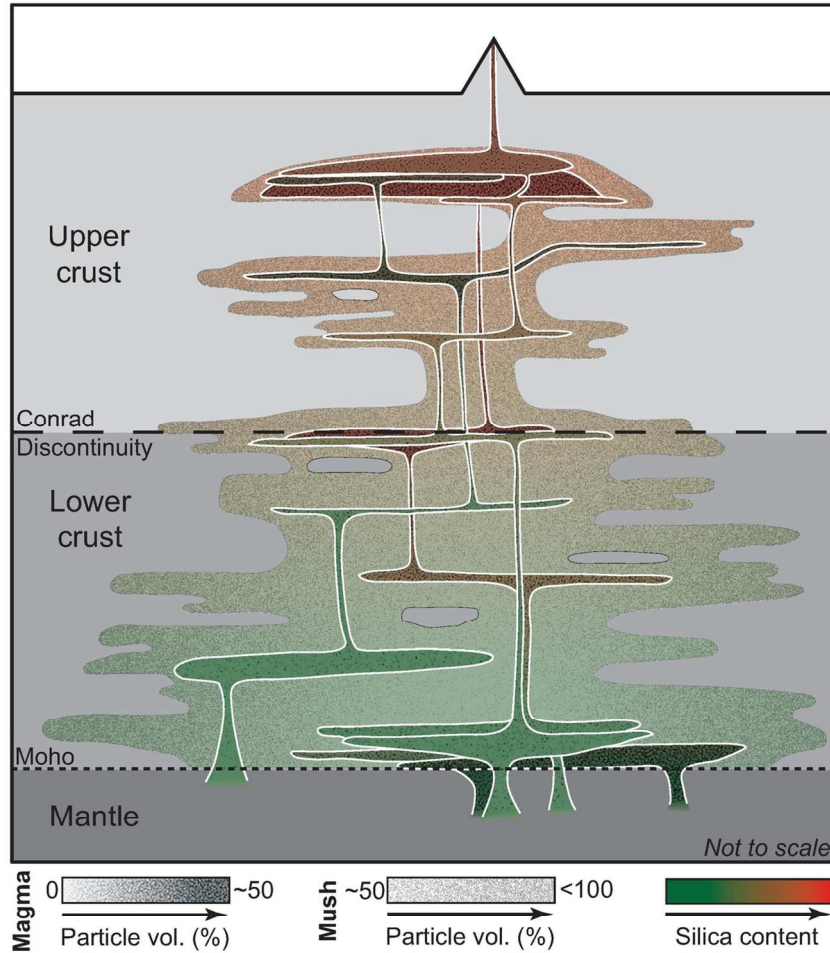


Figure 1: Schematic of a vertically extensive, transcrustal magma plumbing system involving transient, interconnected, relatively low-volume tabular magma intrusions (e.g., dykes, sills, and laccoliths) within a crystal mush (based on Cashman et al., 2017; Cruden et al., 2018).

126x136mm (300 x 300 DPI)

Figure 2

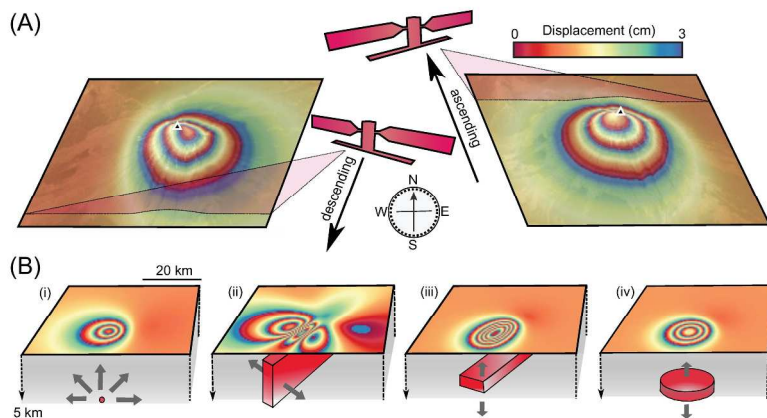


Figure 2: (A) Interferograms showing fringes caused by the pressurisation of a point source directly beneath a stratovolcano from both ascending and descending satellite lines of sight. Note that the centre of the fringes are slightly offset from the summit of the volcano (marked by a black triangle). (B) Typical fringe patterns for analytical deformation sources in an elastic half space from ascending satellite geometry: (i) Mogi source at 5 km depth; (ii) dyke extending between depths of 3 and 9 km; (iii) rectangular sill; and (iv) a penny-shaped horizontal crack both at 5 km depth.

250x366mm (300 x 300 DPI)

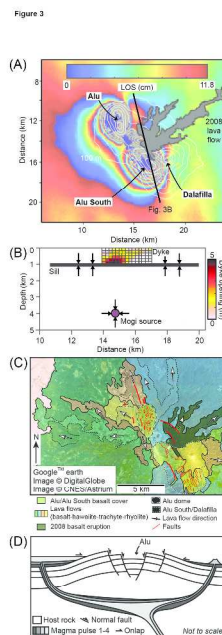


Figure 3: (A) Ascending line of sight (LOS) co-eruptive interferogram from the 2008 basalt lava extrusion between the Alu and Alu South domes and the Dalafilla stratovolcano (modified from Pagli et al., 2012). (B) Inversion of uplift and subsidence patterns, recorded by InSAR during the 2008 basalt lava eruption at the Alu dome in the Danakil Depression, suggested ground deformation could be attributed to a combination of: (i) deflation of a reservoir, modelled as a Mogi source, at ~4 km depth; (ii) inflation and deflation of a tabular sill at ~1 km depth; and (iii) opening of a dyke beneath the eruptive fissure (Figs 3A and B) (Pagli et al., 2012). See Figure 3A for location. (C) Geological map showing that lava flows radiate out from Alu and originate from the periphery of the dome, which is cross-cut by an array of randomly oriented faults (modified from Magee et al., 2017). (D) Magee et al., (2017) inferred Alu is underlain by a saucer-shaped sill plumbing system, based on field observations and comparison to seismic reflection data, not a tabular sill (Fig. 3B).

373x370mm (300 x 300 DPI)

Figure 4

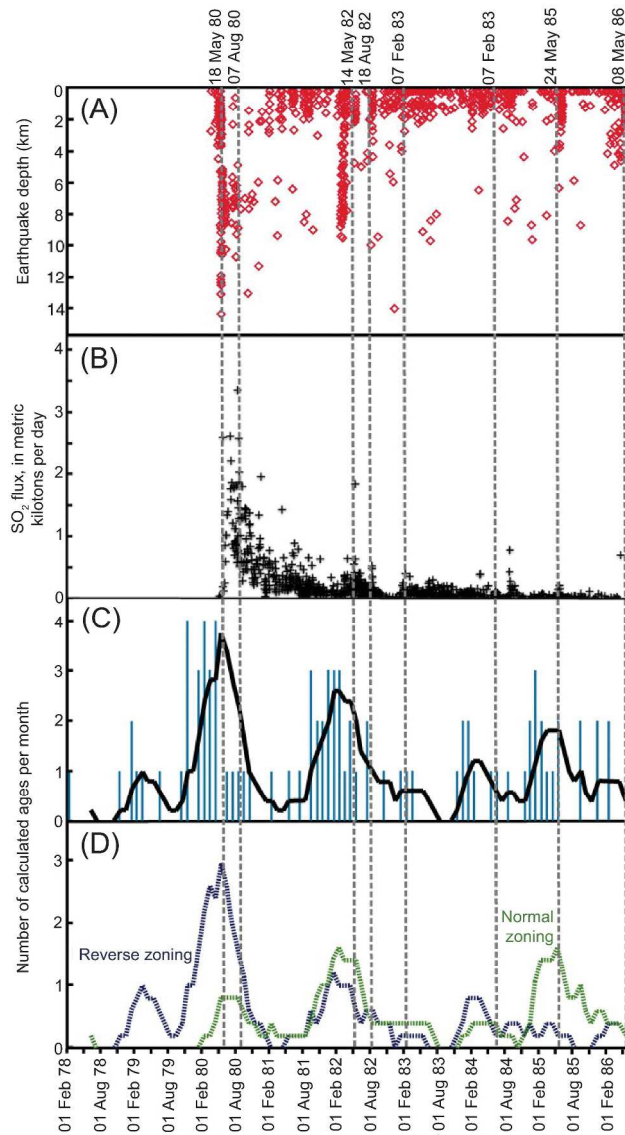


Figure 4: Example of integrating seismology and petrology to constrain time-scales of magma storage and recharge (from Saunders et al., 2012). Calculated Fe-Mg diffusion time scales of orthopyroxene crystals compared to monitoring data for the same eruptive period for Mount St. Helens. (A) The seismic record of depth against time of the 1980–1986 eruption sequence. (B) Measured flux of SO₂ gas. (C) Calculated age of orthopyroxene rim growth binned by month for the entire population. The age recorded is the month in which the orthopyroxene rim growth was triggered by magmatic perturbation. The black line displays the running average (over five points, equivalent to the average calculated uncertainty in calculated time scales) of all the data. The peaks in the diffusion time series correspond to episodes of deep seismicity in 1980 and 1982 and to elevated SO₂ flux in 1980 and possibly 1982. (D) Running average of the orthopyroxene rim time scales, displaying reverse zonation (Mg-rich rims) in blue and normal zonation (Fe-rich rims) in green. There are reverse zonation peaks in the early 1980, probably due to rejuvenation of the magma system by hotter pulses, whereas Fe-rich rims are more dominant from 1982 on. Vertical dashed grey lines represent the volcanic eruptions.

1
2
3
4
5
6
7
8
9
10
11
12
13
14
15
16
17
18
19
20
21
22
23
24
25
26
27
28
29
30
31
32
33
34
35
36
37
38
39
40
41
42
43
44
45
46
47
48
49
50
51
52
53
54
55
56
57
58
59
60

206x396mm (300 x 300 DPI)

For Peer Review

Figure 5

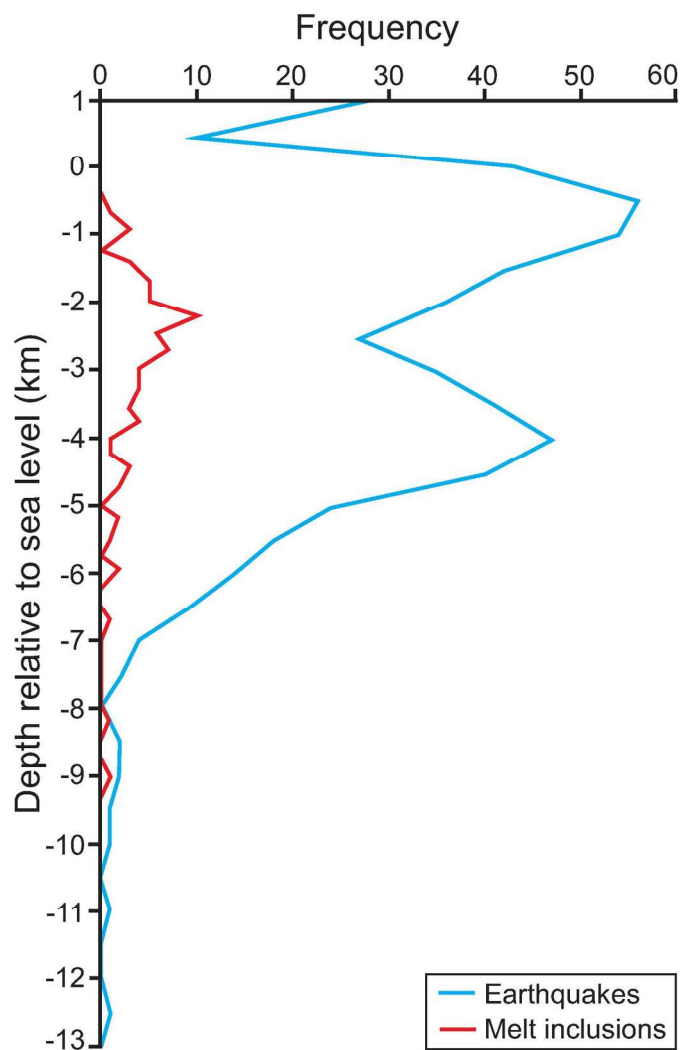


Figure 5: Plot of melt inclusion saturation and earthquake hypocentre depths, which suggest magma storage occurred at 1–5 km depths, beneath the Dabbahu volcanic system in Afar, Ethiopia (modified from Field et al., 2012). Melt inclusion data obtained from analyses of alkali feldspar, clinopyroxene, and olivine phenocrysts within Dabbahu lavas <8 Kyr (Field et al., 2012). Earthquake data recorded during the 2005 dyke event (Ebinger et al., 2008).

121x218mm (300 x 300 DPI)

Figure 6

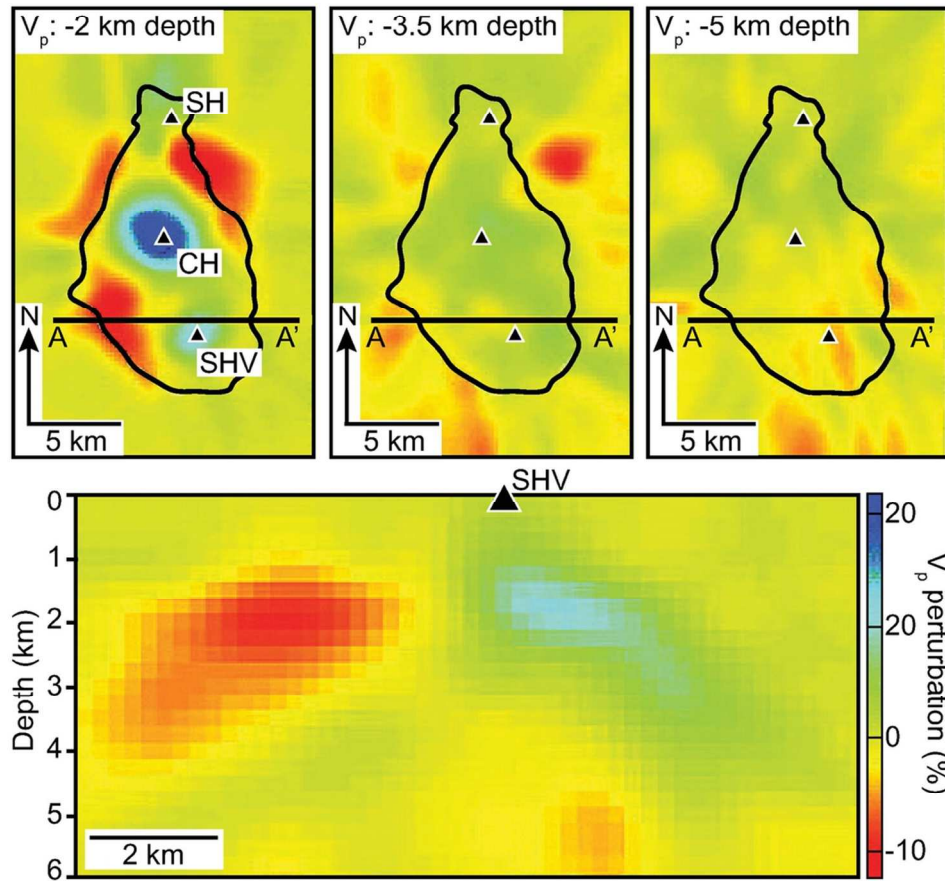


Figure 6: (A) P-wave (V_p) tomography beneath Montserrat (black outline), highlighting the location of fast and slow seismic velocity anomalies (i.e. $>6\%$ faster or slower than average) relative to the location of the Silver Hills (SH), Central Hills (CH), and Soufrière Hills (SHV) volcanoes (modified from Shalev et al., 2010). The fast velocity anomalies, interpreted to represent solidified andesitic intrusions underlie the volcanoes (Shalev et al., 2010).

95x92mm (300 x 300 DPI)

Figure 7

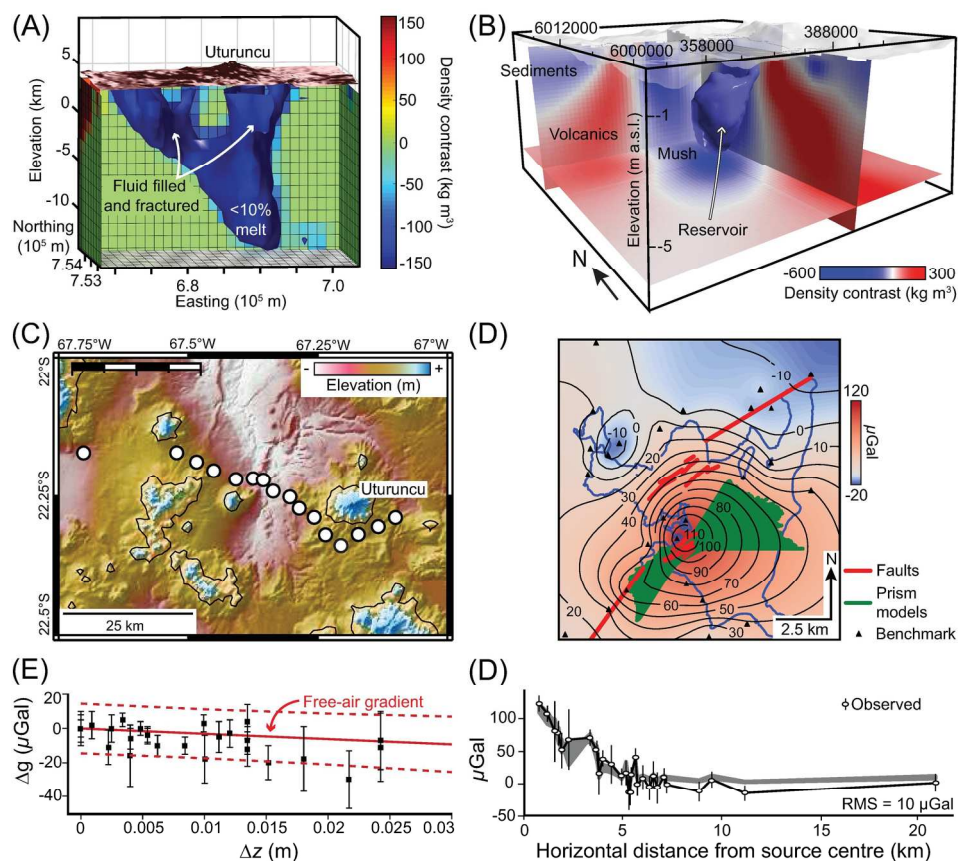


Figure 7: Static and dynamic gravimetric investigations of two active silicic magmatic systems in the Andes: Uturuncu volcano (Bolivia; A, C, and E) and the Laguna del Maule volcanic field (Chile; B, D, and F). (A) 3D view of the isosurface corresponding to the -120 kg m^{-3} density contrast beneath Uturuncu volcano, derived from Bouguer gravity data, interpreted to reflect a large ($\sim 750 \text{ km}^3$) plumbing system composed of a lower ($< -10 \text{ km}$) partially molten reservoir and upper, fractured and fluid-bearing solidified intrusions above sea level (after del Potro et al., 2013). (B) 3D view of the -600 kg m^{-3} density contrast isosurface beneath the Laguna del Maule, which is interpreted to define a magma reservoir ($> 50 \%$ melt) within a larger region of a crystal mush system; the 2D planes show slices through the dataset (Miller et al., 2017). Elevation above sea level (a.s.l.) shown. See Figure 7D for area of data coverage. (C) Map of the 55 km long, dynamic gravity network (white circles) installed to track changes in gravity over time and space at Uturuncu volcano between 2010 and 2013 (modified from Gottsmann et al., 2017). (D) Spatio-temporal residual gravity changes at Laguna del Maule recorded from 2013–2014, after correcting for deformation effects (modified from Miller et al., 2017). (E) Gravity and deformation data, recorded from Uturuncu from 2010–2013, plotted against the measured free-air gravity gradient (solid red line) and associated errors (broken red lines) (modified from Gottsmann et al., 2017). The data follow the gradient and are indicative of a subsurface density change as a cause of the uplift, possibly reflecting the release of fluids from a large deep-seated magma reservoir (i.e. the Altiplano-Puna Magmatic Body; Chmielowski et al., 1999) through the vertically extensive crystal mush system shown in (A) (Gottsmann et al., 2017). (F) Plot of gravity against horizontal distance for the source centre at Laguna del Maule (modified from Miller et al., 2017). The

1
2
3
4
5
6
7
8
9
10
11
12
13
14
15
16
17
18
19
20
21
22
23
24
25
26
27
28
29
30
31
32
33
34
35
36
37
38
39
40
41
42
43
44
45
46
47
48
49
50
51
52
53
54
55
56
57
58
59
60

increase in gravity of up to 120 μGal is explained by a hydrothermal fluid injection focused along a fault system, shown in (D), at 1.5–2 km depth as a result of a deeper seated magma injection, and is best modelled by a vertical rectangular prism source.

180x187mm (300 x 300 DPI)

For Peer Review

Figure 8

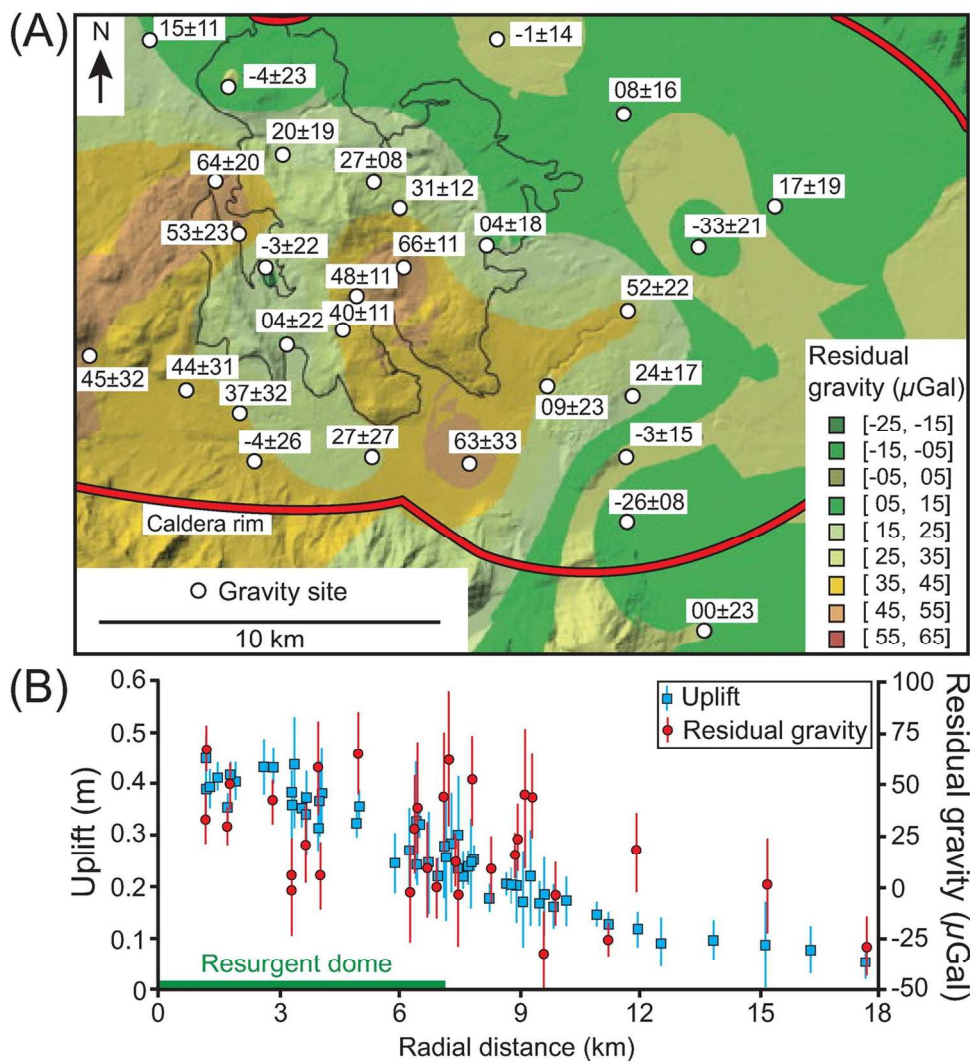


Figure 8: Gravity changes and deformation at the restless Long Valley caldera. (A) Map of the Long Valley caldera, California, USA, which hosts a resurgent dome (black outline), to highlight changes in residual gravity between 1982 and 1999 (modified from Tizzani et al., 2009). (B) Plot of ground uplift and residual gravity changes with radial distance from the centre of the resurgent dome in (A) (modified from Tizzani et al., 2009). The correlation between uplift and positive gravity residuals across the resurgent dome indicates ground deformation was instigated by intrusion of magma (Tizzani et al., 2009).

126x146mm (300 x 300 DPI)

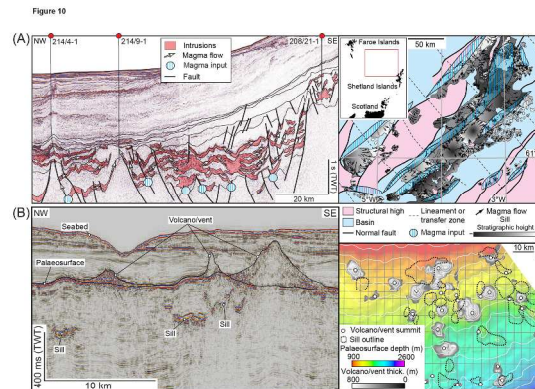


Figure 10: (A) Interpreted seismic section and geological map showing the distribution of and connectivity between sills within the Faroe-Shetland Basin (modified from Schofield et al., 2017). Mapping of magma flow patterns within individual sills reveals that the sill-complex facilitates extensive vertical and lateral magma transport. Magma was fed into the sedimentary basin via basement-involved faults. TWT = two-way travel time. (B) Interpreted seismic section and geological map describing the spatial relationship between volcanoes/vents and sills, inferred to represent the magma plumbing system, emplaced at ~ 42 Ma (modified from Jackson et al., 2013; Magee et al., 2013a). Sills are laterally offset from the volcanoes/vents summits. No 'magma chambers' are observed in the seismic data, which images down to ~ 8 s TWT (i.e. $\sim > 10$ km) (Magee et al., 2013a).

374x216mm (300 x 300 DPI)

Figure 11

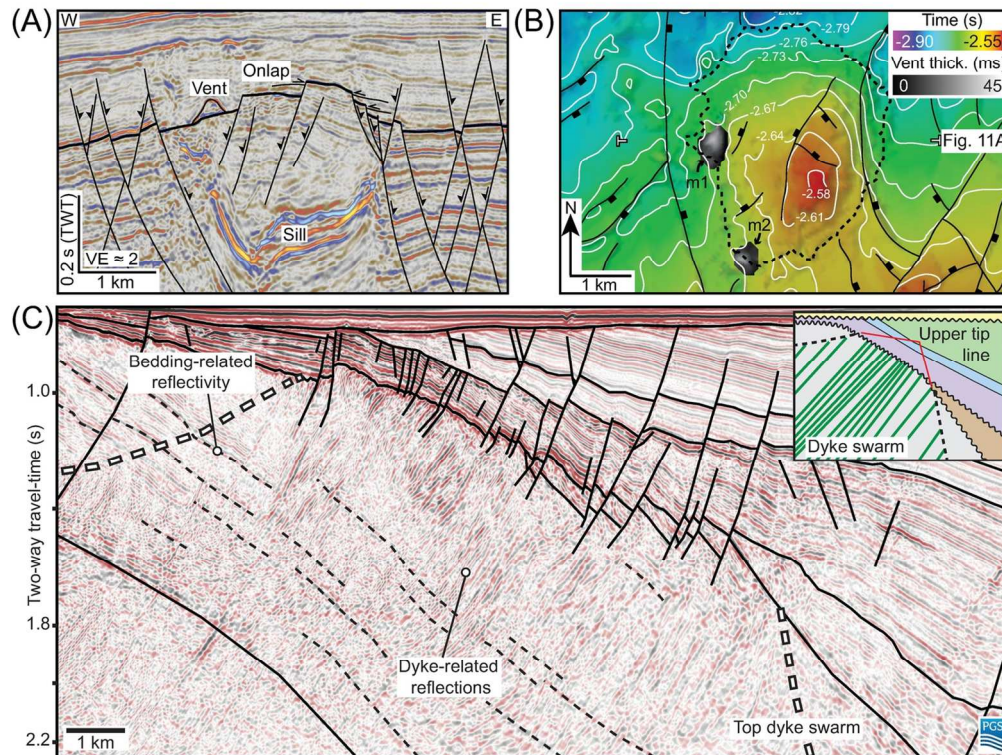


Figure 11: (A) Interpreted seismic section from the Exmouth Sub-basin offshore NW Australia, which images a saucer-shaped sill that is overlain by a forced fold and feeds a small vent from its inclined limb (modified from Magee et al., 2013b). See Figure 11B for line location). (B) Time-structure map of the folded horizon (thick black line) in (A), highlighting fault traces and vent locations and thicknesses (modified from Magee et al., 2013b). (C) Seismic section from the Farsund Basin, offshore southern Norway, which images part of a dyke-swarm that has been rotated by basin flexure post-emplacement (modified from Phillips et al., 2017).

127x101mm (300 x 300 DPI)

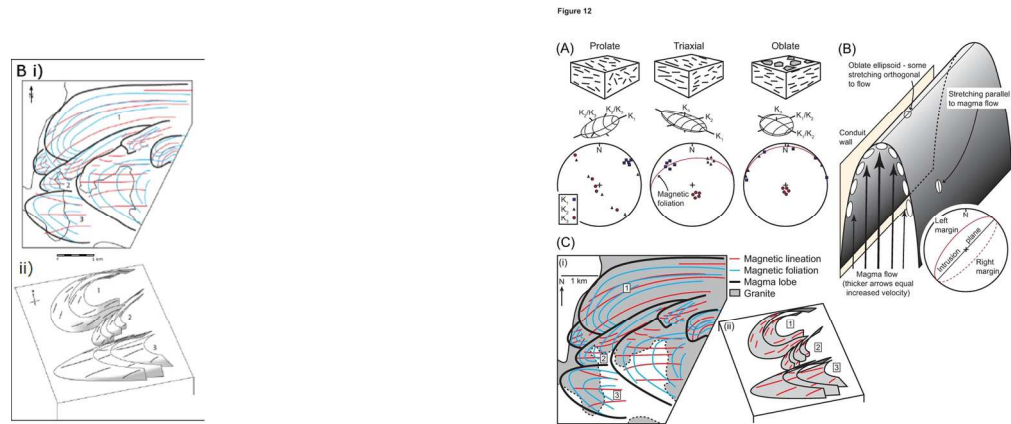


Figure 12: (A) At the sample scale, all magnetic grains create a magnetic fabric. (i) Dominantly prolate fabric, where K_2 and K_3 are least certain and form a girdle. Only the magnetic lineation (K_1) can be confidently determined. (ii) When $K_1 > K_2 > K_3$, both a foliation (K_1 – K_2) and a lineation (K_1) may be discerned, defining a triaxial fabric. (iii) When K_1 and K_2 are equally uncertain and form a girdle, K_3 is perpendicular to a foliation. (B) Schematic representation of how magma flow within a planar sheet intrusion can produce imbricated magnetic fabrics at its margins, the closure of which define the magma flow direction (after Féménias et al., 2004). (C) AMS data and interpretations from part of the Trawenagh Bay Granite, NW Ireland (adapted from Stevenson et al., 2007a). (i) AMS foliation traces are shown in blue and lineation traces in red. Lobes were defined in this intrusion based on foliations curving around a lineation axis. In some lobes, the magnetic lineation trend was parallel to this axis, whilst in others they tended to splay or converge down flow. (ii) 3D sketch showing the geometry of three of the lobes (numbered in part i).

153x63mm (300 x 300 DPI)

Figure 13

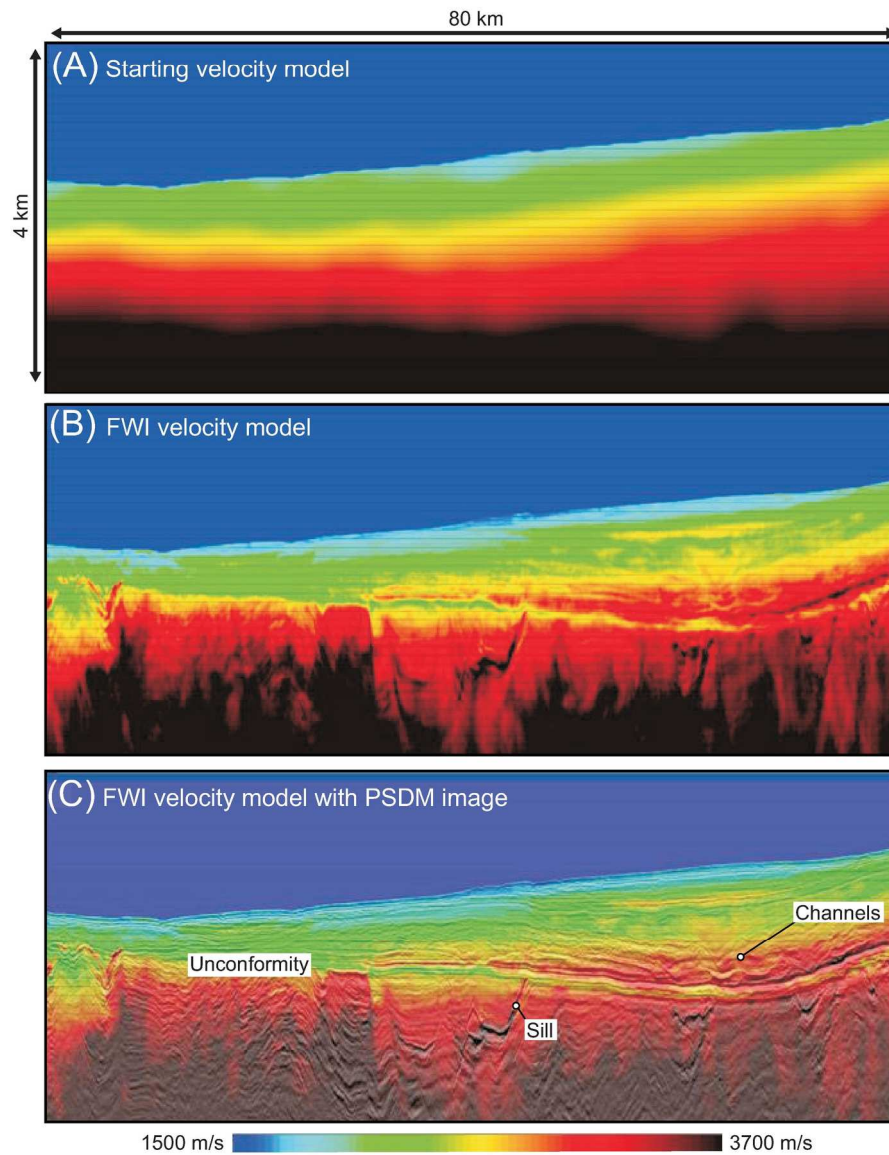


Figure 13: (A) Starting model derived from smoothed, pre-stack, time-migrated (PSTM) stacking velocities. (B) Final 2D FWI-derived velocity model obtained using 10 km streamer data and inversion frequencies of between 2.5 and 24 Hz. (C) FWI velocity model overlain by the 2D pre-stack, depth-migrated (PSDM) section. Strong irregular reflections in the lower half of the section are from basaltic intrusions, which appear as high-velocity anomalies in the FWI velocity model. Both the FWI velocity model and the PSDM pick out a major unconformity, and show shallow channels in the upper parts of the section (redrawn from Kalincheva et al., 2017).

167x221mm (300 x 300 DPI)

Figure 14

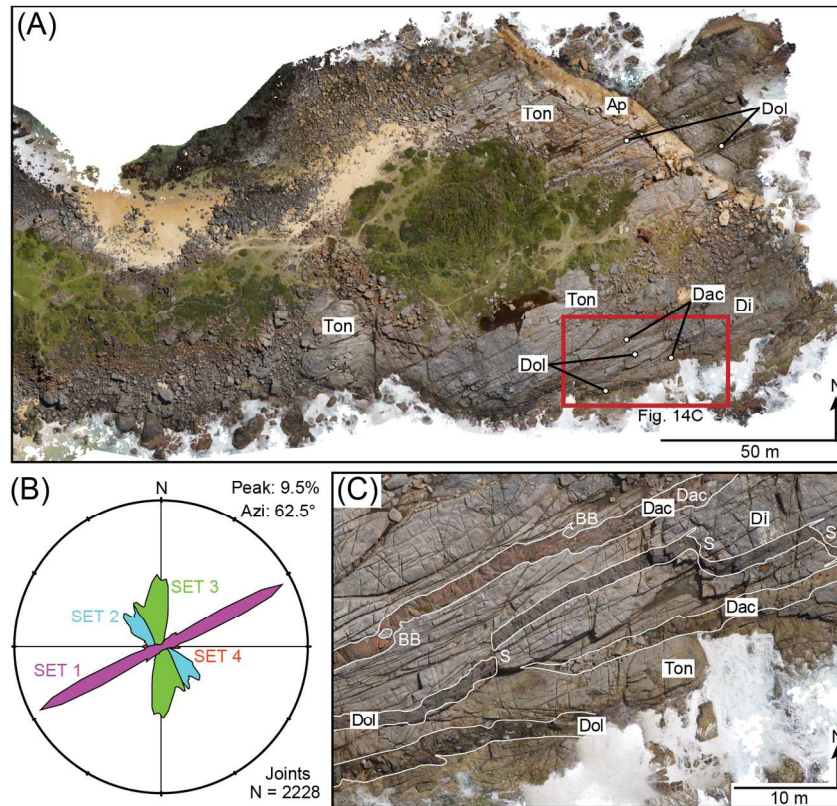


Figure 14: (A) UAV orthophotograph of the wave cut platform at Bingie Point, NSW, Australia showing the distribution of Palaeogene dolerite (Dol) and dacite (Dac) dykes within Devonian tonalite (Ton), diorite (Di), and aplite (Ap) host rocks. (B) Circular histogram of joint sets measured in the Devonian rocks from the orthophotograph; the dominant (purple) set is parallel to and likely contemporaneous with the Palaeogene dykes. (C) Annotated close-up image highlighting dykes and structural features. The northern dacite dyke shows two broken bridge (BB) structures, whilst the central dolerite dyke displays prominent step structures (S). Narrow apophyses are also associated with the broken bridges and steps.

162x148mm (300 x 300 DPI)